III-Nitride: Fabrication and Characterisation of Micron and Sub-Micron Structured Electrically Injected Light-Emitting Diode

Author: Suneal S. Ghataora

Supervisor: Prof. Tao Wang
2nd Supervisor: Dr. Richard M. Smith

A Thesis Submitted in Partial Fulfilment of the Requirements for the Degree of Doctor of Philosophy

The University of Sheffield
Department of Electronic and Electrical Engineering

August, 2019

Abstract

This thesis is focused toward the fabrication and characterisation of electrically injected micron and sub-micron featured III-nitride light-emitting diode (LED), demonstrating new and interesting device structures. A number of unique fabrication process have been developed in the production of 2D micro-hole array, 1D nano-grating array and single micro/nano-pillar structured light-emitting devices.

Initial efforts consider the combined complimentary benefits of the organic and inorganic semiconductor material systems, featuring the respective high-performance fluorescent quantum yield and electrical properties. The main advantage to a hybrid organic/inorganic LED is the highly-efficient radiation-less Förster resonance energy transfer (FRET) process, requiring near-field proximity (< 10 nm) between donor (InGaN/GaN MQW) and acceptor (organic light-emitting polymer) dipole. A 2D micro-hole and 1D nano-grating array structure through the InGaN/GaN MQW of a high-performance LED have both been demonstrated to provide the necessary dipole-dipole separation; resulting in respective FRET efficiencies of 16.7 % and 31.3 %, where total FRET interaction area accounts just 0.64 % and 3.91 %.

The emission of a c-plane III-nitride LED is intrinsically unpolarised, periodic 1D nano-grating arrays mean it can serve as an efficient blue light-emitter and polariser through anisotropic strain relaxation. A uniaxial alignment of the otherwise highly-disordered organic molecules is also then achieved through effective nano-confinement to the 1D nano-grating structure, substantially increasing polarised light absorption/emission with the molecular order. The polarisation dependent measurements show the hybrid organic/inorganic device with a combined white light polarisation degree up to 44 %; electrically injected blue emitting devices have a highest 34 % polarisation degree with largest nano-grating duty-cycle.

A novel sub-wavelength fabrication method is also documented with the development and optimisation of a modified single-instrument direct-write laser photolithography and high-resolution confocal photoluminescence microscopy system; demonstrating mask-less laser-ablation and exposure of photoresist below diffraction-limited spot-size. In a technical demonstration the electrical characteristics of a 3.7 µm and 13 µm diameter single micro-pillar structured III-nitride LED are presented, but more significantly single nano-pillar devices with respective 326.2 nm and 382.1 nm diameter are also shown.

Acknowledgement

I have received much support in this project and I would like to extend my gratitude to all for their patient help and assistance.

I would like to begin by thanking my project supervisor, Prof. Tao Wang, whose continuous support and direction has been invaluable throughout. In addition I would also like to show my appreciation to him for affording me the incredible opportunity to become part of the interesting research area of III-nitride optoelectronics; thank you for going above and beyond what is expected.

I would next like to offer my appreciation to my 2nd supervisor, Dr. Richard Smith, whose unrestricted help and discussion has been fundamental.

Members of the *Centre for GaN Materials and Devices* both past and present have each extended me their own insight and friendship for which I am grateful. I want to start by thanking Dr. Modestos Athanasiou for his encouragement, dialogue and teachings. I would also like to express my appreciation to the education and assistance received in device fabrication from the highly-knowledgable Dr. Jie Bai, instrumental in all of my accomplishment. I would next like to thank Mr. Fernando Guzman, Mr. Nicolas Poyiatzis, Mr. Zohaib Ahem Syed, Mr. Ling Jiu and Mr. Shuoheng Shen who all shared extensive knowledge of their individual research topics. Finally I would like to recognise the contributions of former colleagues Dr. Yipin Gong, Dr. Kun Xing, Dr. Xiang Yu, Dr. Yun Zhang, Dr. Zhi Li and Dr. Yaonan Hou to our current and future success.

In addition I must also share my admiration of the technical staff that endeavour to maintain the safe working condition of the cleanroom facility and its necessary equipment. Particular thanks are offered to Mr. Paul Haines, Mr. Jonathan Milner, Mr. Saurabh Kumar, Dr. Kenneth Kennedy, Dr. David Morris, Dr. Rob Airey and Mr. Gordon Askwith. I would also like to express an appreciation of the often unnoticed work of Mrs. Kim Brechin, Mrs. Hilary Levesley and Mrs. Frances Bright in administration; as well as to Mr. Karl Rotchell, Mr. David Miller and Mr. David Snowden in the faculty workshop for bringing life to technical drawing.

Ultimately I am beholden to my family for their unconditional love and support, thank you. A particular mention must go to my sister who is there when I need her the most.

I will forever be indebted to the understanding and support of my girlfriend, I love you. Awoo.

Publication

Journal Publication

M. Athanasiou, R. M. Smith, S. Ghataora, and T. Wang, '*Polarized White Light from Hybrid Organic/III-Nitrides Grating Structures*', Sci. Rep. **7**, 39677 (2017).

S. Ghataora, R. M. Smith, M. Athanasiou, and T. Wang, '*Electrically Injected Hybrid Organic/Inorganic III-Nitride White Light-Emitting Diodes with Nonradiative Förster Resonance Energy Transfer*', ACS Photonics **5**, 642–647 (2018).

S. Ghataora, R. M. Smith, N. Poyiatzis, M. Athanasiou, and T. Wang, '*Sub-Micron Direct-Write Photolithography using Confocal Photoluminescence Microscopy System in Fabrication of III-Nitride Micro-Pillar Light-Emitting Diode Device*', ***Under Review*** (2019).

Conference Presentation

M. Athanasiou, R. M. Smith, S. Ghataora, and T. Wang, '*Polarized White Light Emission from Hybrid Organic/III-Nitrides Grating Structures*', UK Semiconductors, Cambridge (2016).

S. Ghataora, R. M. Smith, M. Athanasiou, and T. Wang, '*Fabrication and Characterisation of Electrically Injected Hybrid Organic/III-Nitride White Light-Emitting Diodes*', UK Semiconductors, Sheffield (2016).

S. Ghataora, R. M. Smith, M. Athanasiou, and T. Wang, '*Hybrid Organic/III-Nitride White Light-Emitting Diodes with Non-Radiative Resonant Energy Transfer*', 16th International Symposium on the Science and Technology of Lighting, Sheffield (2018).

Contents

1 Introduction **1**

1.1 Introduction 2

1.1.1 Motivation 2

1.1.2 History 3

1.1.3 Project Description 6

1.2 Issues and Limitations 8

1.2.1 Lattice Mismatch 8

1.2.2 Efficiency Droop 13

1.2.3 Light Extraction Efficiency 14

1.3 References 17

2 Background Information **26**

2.1 Background Information 27

2.1.1 Isolated Atoms 27

2.1.2 Crystal Structure 28

2.1.3 Bandstructure 29

2.1.4 Semiconductors 30

2.1.5 Carrier Concentration 31

2.1.6 Direct and Indirect Band-Gap 33

2.1.7 Optical Transitions 36

2.2 Light-Emitting Diode 39

2.2.1 Semiconductor PN-Junction 43

2.2.2 White Light-Emitting Diode 44

2.3 Laser Diode 46

2.3.1 Purcell Effect 47

2.3.2 Whispering Gallery Mode 49

2.4 Organic Semiconductors 50
2.4.1 Hybrid Organic/Inorganic White Light-Emitting Diode . . 52
2.4.2 Förster Resonance Energy Transfer 52
2.5 References 55

3 Experimental Techniques 61
3.1 Experimental Techniques 62
3.2 Device Fabrication 62
3.2.1 Photolithography 62
3.2.2 Dry-Etching 63
3.2.3 Thin-Film Deposition 66
3.2.4 Anaerobic Glove-Box 68
3.3 Device Characterisation 70
3.3.1 Optical and Electrical Characterisation 70
3.3.2 Scanning Electron Microscopy 75
3.4 References 77

4 Electrically Injected Hybrid Organic/Inorganic White Light-Emitting Diode with Non-Radiative Förster Resonance Energy Transfer 79
4.1 Introduction 80
4.2 Method 82
4.2.1 Fabrication 82
4.3 Results and Discussion 86
4.3.1 Electroluminescence 86
4.3.2 Photoluminescence and Time-Resolved Photoluminescence 88
4.4 Conclusion 94
4.5 References 95

5 Polarised Light Emission from Inorganic and Hybrid Organic/Inorganic Nano-Grating Structured Device 99
5.1 Introduction 100
5.2 Hybrid Nano-Grating Photoluminescence 103
5.2.1 Fabrication 103
5.2.2 Photoluminescence 105
5.2.3 Time-Resolved Photoluminescence 109
5.3 Inorganic Nano-Grating Electroluminescence 111

5.3.1 Fabrication 111
5.3.2 Electroluminescence 114
5.4 Conclusion 118
5.5 References 119

6 Direct-Write Laser Photolithography Fabrication of Micron and Sub-Micron Single Pillar Inorganic Light-Emitting Device 123
6.1 Introduction 124
6.2 Method 125
6.2.1 System Description 125
6.3 Micron and Sub-Micron Pillar Photoluminescence 127
6.3.1 Fabrication 127
6.3.2 Direct-Write Optimisation 129
6.3.3 Confocal Photoluminescence 134
6.4 Micron Pillar Electroluminescence 137
6.4.1 Fabrication 138
6.4.2 Electroluminescence 141
6.5 Conclusion 142
6.6 References 144

7 Conclusion 148
7.1 Conclusion 149
7.1.1 Overview 149
7.1.2 Future Research 151
7.2 References 152

8 Appendices 153
8.1 Appendix 1 - List of Symbols 154
8.2 Appendix 2 - As-Grown Sample Structures 157

Chapter 1

Introduction

1.1 Introduction

III-nitride materials are considered the most important semiconductor alloy system in solid-state optoelectronic application. This is because the III-V compounds of aluminium nitride (AlN), gallium nitride (GaN) and indium nitride (InN) provide direct band-gap energy that cover beyond the entire visible spectrum (390 nm to 720 nm). The miscibility and lattice constant of III-N materials allow further composition of ternary and quaternary alloys, forming average properties of the constituent elements[1]. A band-gap energy between AlN 6.0 eV (206 nm), GaN 3.4 eV (364 nm) and InN 0.7 eV (1771 nm) is therefore all possible.

A double heterostructure InGaN/GaN light-emitting diode (LED) with an $In_{0.17}Ga_{0.83}N$ active region produces high-energy blue ($\sim$450 nm) light emission. This high-efficiency optoelectronic device in combination with a radiatively-pumped yellow down-converting phosphor provides the current standard for dichromatic solid-state white light[2]. The typical down-conversion material is a powdered YAG ($Y_3Al_5O_12 : Ce^{3+}$) phosphor, requiring optically-active rare-earth cerium (Ce) ion dopants[3].

1.1.1 Motivation

Anthropogenic carbon emissions have continuously increased since mid-18th century industrialisation[4]. This is the result of the increasing reliance on energy production using carbon-intensive fossil-fuels with annual (2017) global CO_2 net-emissions of 41.2 $GtCO_2e$, with UK contributing an estimated 460.2 $MtCO_2e$[5,6].

The UK (2017) electricity consumption totals 353.8 TWh, which is dominated by non-renewable and non-environmentally friendly means. A breakdown includes contributions in production of gas/coal 47.1 %, nuclear 20.8 % and renewable 29.3 %. However, end consumption is primarily split between domestic (105.4 TWh), commercial (73.8 TWh) and industrial (92.6 TWh) sectors complete to 271.8 TWh[7]. The UK is committed to legally-binding targets that will see reduction in the 1990 anthropogenic carbon emissions by 34 % in 2020 and further to 80 % in 2050, as stated in the Climate Change Act 2008; committing even more recently to attain net-zero emissions in that same period[8,9]. The UK parliamentary strategy to meet gradual decreasing carbon budgets is two-fold, and includes a lowered reliance on non-renewable (carbon-intensive) energy and reduced consumption through increased efficiency, where equivalent CO_2 emissions are an already

estimated 42.1 % lower than in 1990[6,8].

A reported ∼20 % of the 25082 TWh generated electricity is consumed in artificial lighting applications, accountable for an approximate 1900 $MtCO_2e$ global CO_2 emissions annually[10,11]. The transition of present artificial lighting to predominantly high-efficiency low-carbon LED technology can therefore result in considerable energy reduction without impact to performance[9]. The European Union (EU) introduced recent legislation across member states to regulate a gradual phase-out of incandescent light bulbs between 2009 and 2012; with a widespread cost-effective social shift to the ∼80 % more efficient compact fluorescent lamp (CFL)[12].

The incandescent light bulb relies on thermal black-body radiation of a tungsten filament, and therefore has intrinsically low ∼16 lm/W luminous efficacy[13]. A fluorescent lamp generates light emission through an electrical discharge across gas, exciting mercury-vapours (5 mg). The internal transitions release ultraviolet photons that are then down-converted to visible-wavelength, typical luminous efficacy of a CFL are less than 100 lm/W[13].

LEDs provide an alternative for further improvement in luminous efficacy, with theoretical limits between 250 lm/W and 370 lm/W, and commercially available up to 150 lm/W[14]. However, despite evident advantages of solid-state lighting the inherent high manufacturing-costs slows uptake, although this can be offset across the significantly longer LED lifetime (> 100000 hours)[15].

1.1.2 History

The LED was initially discovered by H.J. Round, published in 1907, in which electroluminescence from a carborundum (silicon carbide) diode was first claimed[16]. O.V. Losev then independently rediscovered the LED, with publication in 1927, detailing light emission of silicon carbide diodes with electrical excitation. Although this had first been noticed in 1907, O.V. Losev, correctly theorised that quantum mechanics explained the non-incandescent light emission[17,18].

The first functional LED wasn't then developed until 1961, when J.R. Baird and G.E. Pittman patented a near-IR GaAs PN-junction LED emitting at 890 nm[19]. N. Holonyak and S.F. Bevacqua in 1962 are then accredited for demonstrating the first visible light (red) GaAsP LED emitting at 710 nm[20].

LEDs with shorter wavelength have since been produced using similar III-V compound semiconductor materials, including GaAsP with increasing P content.

The limitation of $GaAs_{1-x}P_x$ is that with a phosphorous mole fraction above 0.44 the radiative efficiency decreases significantly, attributed to a direct-indirect band-gap transition[21,22]. Therefore SiC, with an indirect band-gap, was the only material capable of creating blue LEDs, with low efficiencies and maximum external quantum efficiency (EQE) of 0.03 % at 470 nm[23,24].

GaN was first obtained in 1932 by W.C. Johnson et al.[25]; despite this single crystalline growth was not realised until 1969 by H.P. Maruska and J.J. Tietjen using hydride vapour phase epitaxy (HVPE) technique[26]. This allowed the first optical investigation of undoped single-crystal GaN, measuring a direct wide band-gap of 3.39 eV[27]. H.P. Maruska et al. also discovered the undoped GaN films exhibit inherent n-type properties, with electron concentrations typically above 10^{19} cm^{-3}. This unintentional n-type conductivity is a result of the disassociation of nitrogen atoms in GaN at temperatures of 600 °C, leaving nitrogen vacancies in the crystal lattice[26,28]. Preliminary attempts to incorporate acceptor impurities (Zn and Mg) yield high-resistivity insulating materials (> 10^9 Ωcm)[26].

J.I. Pankove et al. reported in 1971, in absence of p-type GaN, the electroluminescence of a metal-insulator-semiconductor (MIS) GaN LED structure[29]. MIS LEDs with 2.35 eV (green) and 2.8 eV (blue) emission at approximately 510 nm and 440 nm, were demonstrated respectively. This was achieved using the same device with lower concentration of Zn doping in the insulating GaN layer at shorter wavelength[29,30]. H.P. Maruska et al. then subsequently invent an MIS LED in 1972, with an insulating Mg-doped layer, which emits electroluminescence centred at 2.9 eV (violet) 425 nm[31]. The high-resistivity of Zn and Mg acceptor doping means the MIS LEDs exhibit luminescence under a large electric-field, caused by avalanche breakdown impact ionisation effects[30,31].

1971, also saw H.M. Manasevit et al. grow the first single-crystalline GaN using metal-organic chemical vapour deposition (MOCVD)[32]; which is a significant step because of the capacity MOCVD provides to deposit mono-layers, a requirement for multi-layer device structures.

III-nitrides were limited then by the inability to grow high-quality materials and absence of p-type conductivity; research focus to realise efficient blue emitting LEDs was then ZnSe (II-VI).

The first high-quality films were not achieved until 1983 when S. Yoshida et al. attempted to grow GaN on AlN coated sapphire substrates using molecular beam epitaxy (MBE)[33]. H. Amano and I. Akasaki et al. then repeated this two-

step growth method in 1985 using MOCVD[34]. This technique requires the low-temperature (600 °C) growth of a thin initial AlN nucleation layer on sapphire, addressing the large lattice mismatch between GaN and foreign substrate[35]. A high-quality GaN layer is then obtained with the subsequent high-temperature growth (1030 °C), with defect density decreasing significantly above 300 nm[36]. A similar two-step method was then introduced in 1991 when T. Moustakas et al. used MBE to grow an initial low-temperature GaN buffer-layer, with the remainder grown at higher temperatures[37].

S. Nakamura et al. proposed in 1991 a novel two-flow MOCVD system, producing high-quality GaN grown directly on sapphire. The two-flow system requires a flow of reactant and inactive gas parallel and perpendicular to the substrate, respectively, with purpose of controlling the direction of the reactant gas[38]. S. Nakamura et al. also in 1991 grew the first high-quality GaN film with GaN buffer-layer across a 2" sapphire substrate using the two-flow MOCVD system[39].

The most significant achievement in development of high-efficiency III-nitride optoelectronic devices was in the realisation of p-type GaN. GaN:Mg layers had been considered strongly resistive, until 1989 when H. Amano et al. used low-energy electron-beam irradiation (LEEBI) to activate p-type conductivity; with Mg concentration in the order of 10^{20} cm^{-3} resistivity dropped to 35 Ωcm from ∼ 10^{8} Ωcm[40,41]. This achievement allowed H. Amano et al. to report the first GaN PN-junction UV LED, proving the possibility of using Mg as an effective p-type acceptor[40]. S. Nakamura in 1992 then alternatively demonstrated uniform p-type GaN throughout the complete film by thermal annealing above 700 °C in a N_2-ambient atmosphere. The initial resistivity of 10^{6} Ωcm fell in the range of 2-8 Ωcm after treatment; resulting in a blue PN-junction LED centred at 430 nm with an EQE of 0.18 %[42]. This caused J. Van Vechten to propose in 1992 that the presence of NH_3 during growth was cause of acceptor compensation in the material, forming Mg-H neutral complexes, and that a sufficient energy dissociates hydrogen to free the shallow acceptor[1,43].

The significant progress that resulted in high-quality GaN on sapphire and controllable p-type doping techniques moved focus to the development of high-efficiency short-wavelength III-nitride LEDs.

Double heterostructures (DH) are essential in high-performance optoelectronic devices, because of carrier confinement and increased quantum efficiencies. The most promising DH active-layer material for high-efficiency blue emission is In-

GaN, with a functional band-gap between 2 eV (620 nm) and 3.4 eV (365 nm), dependent on the indium mole fraction[44]. S. Nakamura et al. in 1992 successfully produced a high-quality 300 nm InGaN layer on GaN, after N. Yoshimoto et al. in 1991 demonstrated the first high-temperature (800 °C) high-quality InGaN film grown on sapphire[45]. The $In_{0.14}Ga_{0.86}N$ and $In_{0.34}Ga_{0.76}N$ layers grown on 2 μm thick GaN resulted in a respective 400 nm (violet) and 445 nm (blue) photoluminescent band-to-band emission[44]. S. Nakamura et al. then in 1994 is able to report the first III-nitride blue LED (450 nm) using an $In_{0.06}Ga_{0.94}N/Al_{0.15}Ga_{0.85}N$ DH, with highest ever luminous intensity of 1.2 cd[46]. High-brightness single-quantum well LED structures, with a ∼2 nm undoped-InGaN active-layer, were then grown by S. Nakamura et al. in 1995, emitting at the blue (450 nm), green (525 nm) and yellow (590 nm) wavelength with In content of 20 %, 43 % and 70 % respectively[47].

The significant contributions of I. Akasaki, H. Amano and S. Nakamura in the development of efficient blue LEDs was recognised with The Nobel Prize in Physics 2014[48].

1.1.3 Project Description

This project considers primarily the fabrication and characterisation of micron and sub-micron structured III-nitride electrically injected light-emitting diode device; connecting original work on hybrid organic and inorganic III-N semiconductors with direct-write laser nano-photolithography.

Initial parts reflect on the combination of organic and inorganic III-N semiconductors, fabricating hybrid white LED with the complimentary benefits of both material systems[49–51]. A resulting device will feature the respective high-performance electrical properties and fluorescent quantum yield (> 85 %) of inorganic and organic materials[52]. The basic configuration, achieving white light emission, involves the partial down-conversion of electrically injected blue InGaN/GaN LED by organic light-emitting polymer (OLEP).

The significant advantage to hybrid organic/inorganic LEDs is the possibility of highly-efficient non-radiative Förster resonance energy transfer (FRET)[49]. FRET involves the near-field (< 10 nm) radiation-less electronic energy transfer from the inorganic active region to OLEP, where it radiatively emits at rates above FRET[53,54]. Avoiding intermediate steps preceding the photoluminescence of the down-converting material, which before absorption includes photon emission and extraction in the inorganic LED[49]. This energy transfer process therefore generates

change in the recombination dynamics, resulting in significant enhancement of the total device efficiency; where FRET rate is sufficient to suppress non-radiative recombination and improve carrier lifetime (τ)[55]. The geometric configuration of the proposed hybrid white LED therefore aims to minimise the separation between donor and acceptor dipoles. This requires a top-down fabrication of a 2D micro-hole array structure through the multi-quantum well (MQW) of a standard planar LED device, allowing an adjacent coupling.

The implementation of an electrically-pumped LED using FRET coupling to a down-conversion material has significant potential to improve efficiency of existing solid-state white light[56]. The decreasing carrier lifetime also presents application in simultaneous illumination and ultra-fast high-bandwidth visible light communication, improving bandwidth with decreasing emission wavelength[57]. The increased modulation rate ($\frac{1}{\tau}$) is typically restricted by the phosphor recombination lifetime ($\sim$70 ns), where receivers filter the slow yellow component[58,59].

A polarised white light emission is also possible by combining a one-dimensional nano-grating structure through standard c-plane InGaN/GaN MQW with down-converting OLEP confined to the nanoscopic domain[50]. This having benefits in areas of liquid-crystal display backlighting, requiring an intrinsic polarised light source that would instead necessitate polarising filters; polarisation is the property describing the orientation at which lights transverse electromagnetic field oscillates.

Emission of a c-plane III-N LED is intrinsically unpolarised. A periodic one-dimensional array of nano-scale channels mean it can serve both as an efficient blue light-emitter and polariser through an expected anisotropic strain relaxation[50,60]. Uniaxial alignment of the otherwise highly-disordered organic molecules in their liquid-crystalline (LC) phase is achieved through effective nano-confinement to the one-dimensional inorganic LED grating structure[61,62]. The conjugated polymer backbones are orientated parallel to the direction of confinement on order less than the molecular chain length. This results in a substantial increase in molecular order that improves both charge transport properties and polarised absorption/emission of light[63,64].

The implementation of an electrically-pumped LED using FRET coupling to a down-conversion material therefore has significant potential to improve the efficiency of white lighting. A hybrid organic/inorganic LED ultimately benefits mutually from the high optical-performance of the InGaN/GaN inorganic emitter

and alignment enhanced high-efficiency FRET colour-conversion process.

The project later also looks to combine advanced epitaxial growth, nano-scale fabrication and characterisation of III-nitride optoelectronics in attempts to produce a first visible light electrically injected single nano-laser.

Sub-wavelength fabrication is otherwise restricted by the diffraction-limit, where features of an optical component approach dimensions on order of the wavelength of light ($\sim\frac{\lambda}{2}$). This requiring first optimisation of a single-instrument direct-write laser photolithography and high-resolution confocal photoluminescence microscopy system, demonstrating mask-less high-power laser-ablation and 2-step exposure of photoresist below the diffraction-limited spot-size without loss to resolution. This leading to the development of an efficient and low-budget optical nano-fabrication technique outside electron-beam lithography.

An ultra-stable high-performance single nano-laser is well-suited to nano-photonics, overcoming existing challenges facing electronic integrated-circuit in fundamental speed and bandwidth limit[65].

1.2 Issues and Limitations

1.2.1 Lattice Mismatch

Substrate

The absence of an inexpensive native bulk III-nitride substrate restricts homo-epitaxial material growth. III-N semiconductors therefore more commonly utilise foreign substrate, suitable for high-temperature epitaxy, which include sapphire (Al_2O_3), silicon carbide (6H-SiC) and silicon (Si, 111)[66].

The difference in structural properties, lattice parameter (table 2.1) and thermal expansion coefficient, between the hetero-epitaxial III-N and substrate lead to a high-density of strain-induced defects. A crystal lattice defect, discussed in section 2.1.7, introduces non-radiative recombination centre, which act to reduce the materials quantum efficiency with increasing density[67]. A typical dislocation-density of III-N materials is on the order of 10^{-8}-10^{-9} cm^{-2}, sufficient to render other II-VI and III-V system optically inactive[68,69].

The $\sim$16 % lattice mismatch in c-plane wurtzite GaN and favoured sapphire substrate, as shown in Figure 1.1, results in compressive strain within the epitaxial layer[66]. GaN undergoes a 30° intrinsic rotation in the hexagonal basal-plane

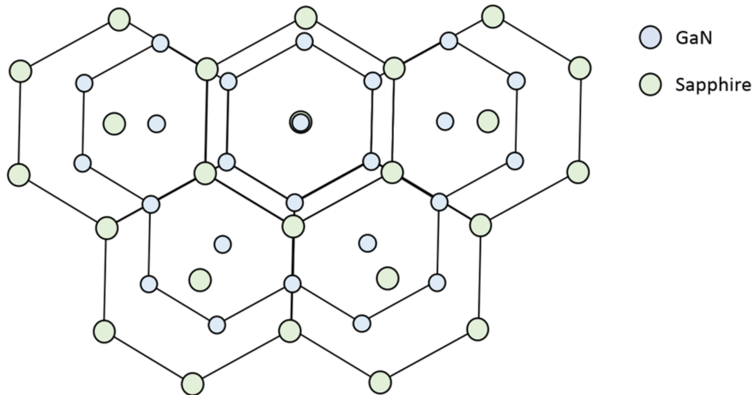

Figure 1.1: Demonstration of Sapphire and GaN lattice mismatch (not to scale).

relative to the sapphire substrate, reducing the effective lattice mismatch from calculated ∼49 %[70].

The low-cost of sapphire mean it remains the most commonly used substrate, despite an improved lattice mismatch with 6H-SiC[71]. However, mature-technology of silicon (cubic) allows further commercial value in the provision of budget large-diameter substrate, although with worse corresponding structural properties.

The availability of viable free-standing bulk-GaN substrate is limited by inability to grow single-crystalline boule using Czochralski process, owed to the high melting point of GaN (> 2500 °C)[72]. The existing native GaN substrates are grown thick on lattice mismatched substrate using hydride vapour phase epitaxy (HVPE), before separating the free-standing GaN[73].

Polarisation

The favoured wurtzite crystal structure of GaN, discussed in section 2.1.2, develops a spontaneous polar field acting in the direction of the c-axis {0001}. This is caused by the lack of inversion symmetry in the c-plane of the hexagonal wurtzite unit cell, making GaN a polar molecule[1]. A polar molecule has a permanent electric dipole-moment, which results from slight displacement in charge caused by differences in electronegativity between constituent Ga (1.81) and N (3.04) atoms[74].

In addition to spontaneous polarisation, InGaN/GaN low-dimensional quantum-confined double heterostructure, section 2.2, induce a dominant piezoelectric field. Figure 1.2 demonstrates pseudomorphic compressive strain causing this piezoelectric polarisation in films below the critical-layer thickness; resultant of the lattice

mismatch between GaN and InGaN that increases with indium composition[75].

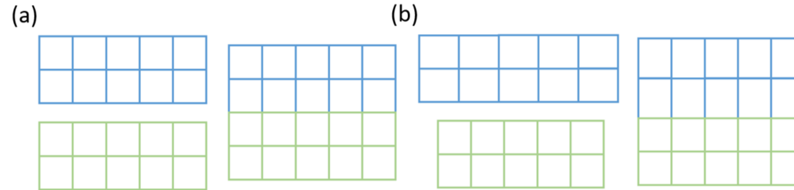

Figure 1.2: (a) lattice match (b) lattice mismatch and psuedomorphic compressive strain.

The mechanical stress, acting on a unit cell absent of a centre of symmetry, causes separation and imbalance in charge across the molecule. The polarity of the polar field is therefore dependent on the direction of applied strain. A compressive strain means that the piezoelectric field acts in the $\{000\bar{1}\}$ direction, conversely a tensile strain is observed in the opposite $\{0001\}$ direction.

Quantum-Confined Stark Effect

The presence of the piezoelectric field across low-dimensional InGaN/GaN double heterostructure results in the Quantum-Confined Stark Effect (QCSE), before crystalline defect formation induces strain relaxation[47,76]. This strong piezoelectric field is formed perpendicular to the QW-plane in the $\{000\bar{1}\}$ direction[77].

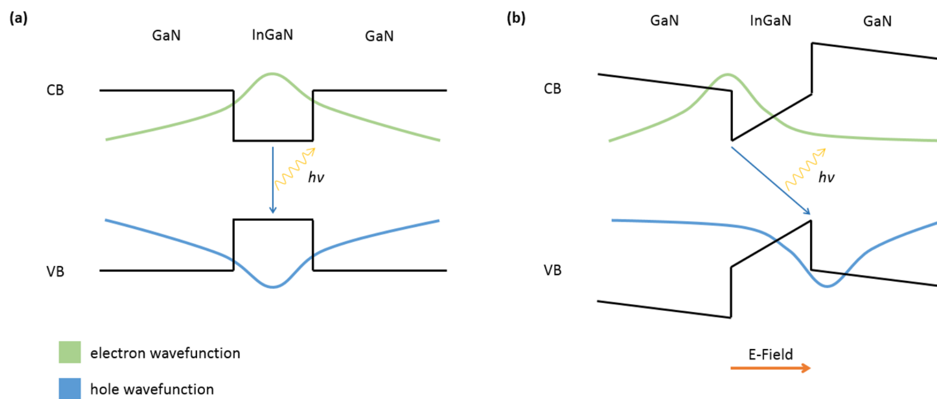

Figure 1.3: Quantum-Confined Stark Effect in (a) non-polar and (b) polar orientation.

QCSE is the quantum confined change in the absorption or emission spectrum to low-energy (red-shift) in response to an applied electric-field[78]. The piezoelec-

tric field produces an intrinsic triangulation within the potential well bandstructure between opposing barriers, moving carriers to favoured energy state reducing the effective band-gap[78], demonstrated in Figure 1.3. This is caused by a spatial displacement of electron and hole concentration in opposite directions to the boundary of the QW structure, resulting also in a decreasing carrier wavefunction overlap[79]. The reduced electron and hole wavefunction overlap leads to a decreased interband optical-transition probability, increasing the radiative lifetime and therefore lower quantum efficiencies[15].

Green Gap

A significant consequence of QCSE, in the III-N alloy system, is the absence of an efficient light-emitting composition in the green region of the visible spectrum.

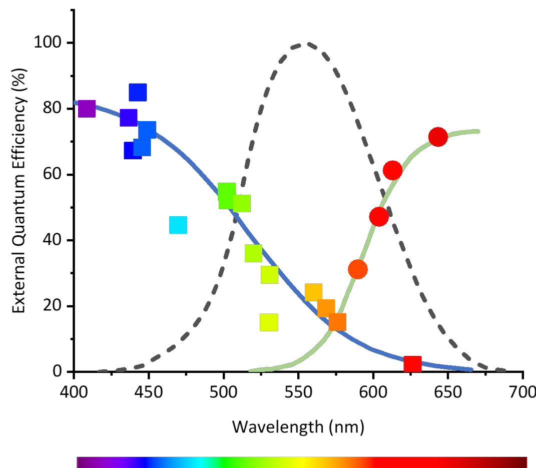

Figure 1.4: Peak wavelength vs. external quantum efficiency (□) {0001} c-plane $In_xGa_{(1-x)}N$, (○) $(Al_xGa_{(1-x)})_{0.52}In_{0.48}P$ and (---) CIE $V(\lambda)$ human eye sensitivity response[80].

The $In_xGa_{(1-x)}N$ alloy system can cover the entire visible spectrum (390 nm to 720 nm), discussed in section 2.2. Emission energy is dependent on the indium mole fraction (x); developing an intermediate between GaN (3.4 eV, 365 nm) and InN band-gap (0.7 eV, 1771 nm). However, increase in the indium composition also results in a larger lattice mismatch in the InGaN/GaN QW structure, which in turn strengthens the piezoelectric field. The QCSE therefore causes a rapid de-

cline in the device quantum efficiency as the emission wavelength tends towards the green region ($\sim$510 nm)[81], as in Figure 1.4 with the CIE $V(\lambda)$ human eye sensitivity response shown as reference. A higher indium incorporation also requires slow growth rate and low-temperature conditions, which adversely affects the crystalline quality, introducing additional non-radiative recombination centres that further reduce the internal quantum efficiency (IQE)[79,82].

The InGaN/GaN QW structured LED can therefore provide efficient blue and violet light, longer wavelength orange and red are even possible using $(Al_xGa_{(1-x)})_{(1-y)}In_yP$ LED. The III-P material system is however restricted to emission wavelengths between 560 nm (yellow) and 650 nm (red). A direct band-gap is available for only $x < 0.53$, where a direct-indirect band-gap transition occurs beyond this composition. The alloy is lattice matched to high-quality GaAs substrates at $y = 0.48$, an essential requirement since a high defect density would otherwise result in significant quantum efficiency reduction[81].

The efficiency in both alloy systems therefore decreases significantly approaching the green region, resulting in the green gap. This highlights the present necessity to combine efficient high-energy blue InGaN/GaN LED with yellow down-conversion materials to achieve solid-state white lighting[2]. However, improvement of the QCSE is concentrated on reducing the piezoelectric component in the direction of QW confinement; including strain relaxation and epitaxial growth in orientations angled from the {0001} c-plane[83].

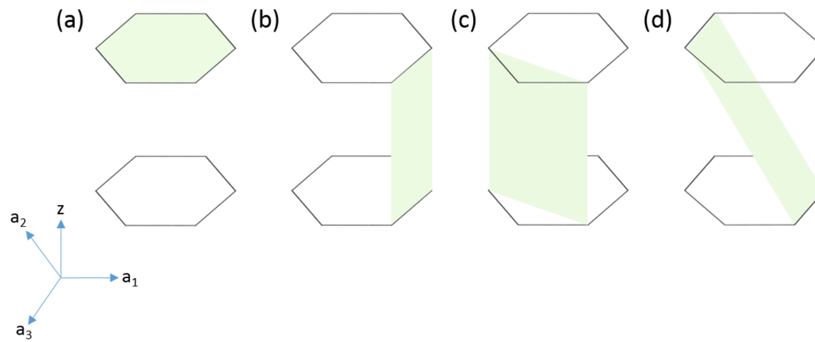

Figure 1.5: Wurtzite crystal orientations (a) c-plane (polar), (b) m-plane (non-polar), (c) a-plane (non-polar) and (d) r-plane (semi-polar).

A strain reduction can be achieved using composition gradient across an intermediate superlattice that effectively modifies the material lattice constant[84]. Alter-

natively, the post-fabrication of a nanostructure within strained epitaxial layers also allows strain relaxation, removing pseudomorphic transition by the Poisson effect, similar to the defect formation[85].

The piezoelectric effect is however conditional on the crystal orientation, as Figure 1.5, where the strongest electric-field is generated in the polar (c-plane) direction. This allows control of the piezoelectric field through a redistribution away from the confinement direction. The growth in semi-polar (r-plane) and non-polar (a-plane/m-plane) directions, orientated 39° and 90° from the {0001} axis, exhibit no longitudinal piezoelectric effect[83].

1.2.2 Efficiency Droop

III-N LEDs require operation under a relatively low current density ($< 10\ Acm^{-2}$). This is because resultant quantum efficiencies begin to significantly decrease ($>$ 40 %) with further increase in the driving current[86], as demonstrated in Figure 1.6. A considerable problem in high-power high-brightness LED, where many applications demand high-efficiency under current densities above 50 Acm^{-2}[87]. The light output power of an LED should ideally increase linearly with the injection current; although an accepted compromise is to maintain a low current density efficiency peak and subsequently minimise the efficiency droop[87].

The exact origin of efficiency droop still remains unknown, therefore remains unsolved without clear consensus, though the fundamental cause is a non-radiative recombination channel negligible at low-current. The most promising suggested mechanisms include carrier leakage, Auger recombination and density-activated defect recombination (DADR)[86].

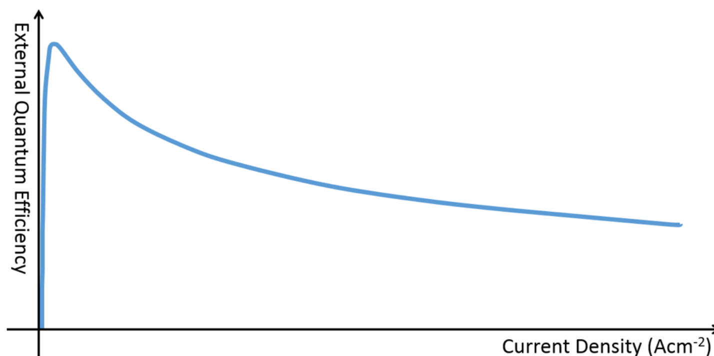

Figure 1.6: Current density vs. external quantum efficiency[86].

- Carrier leakage refers to the injected carriers that transport through the active region without undergoing recombination, either escaping or avoiding quantum confinement[86]. The inability to confine electrons within the active region is a result of an electron with sufficient energy to bypass the QW, as a hot-carrier[86]. Alternatively, at high current density a carrier injected overpopulation of the finite active region volume is possible, causing carriers above the QW potential barrier to delocalise[3]. An electron-blocking layer (EBL), grown between the p-GaN and active region interface, a heavily p-doped AlGaN layer with large band-gap relative to the remaining structure. The purpose of the EBL is to confine electron within the QW and transmit holes from the p-type region, an ineffective EBL is therefore a suspected cause of carrier leakage[3].
- Auger recombination involves the non-radiative transfer of the emission energy to a third charged particle, promoting it to a higher energy level. As a three-particle interaction, Auger recombination is therefore expected to dominate at increasing carrier density[87,88].
- DADR suggests that at low current density the carriers are confined to potential minima within the QW-plane, which result from inherent fluctuations in the InGaN/GaN bandstructure[86]. It is understood that these potential minima, with low defect density, are efficient radiative recombination centres[89]. An increasing carrier injection ultimately results in the overpopulation of these states, causing a delocalisation of carriers to regions with significantly higher defect density. This results in an increase in the non-radiative recombination rate above a threshold current density, typical of efficiency droop[90].

1.2.3 Light Extraction Efficiency

EQE is a measure of the extraction of internally generated photon, limited by the poor light extraction efficiency (LEE) of III-nitrides. This is caused by an optical waveguide effect, which result from the large difference in refractive index (n) between ambient-air ($n = 1$) and GaN ($n \approx 2.5$)[91]. The light is therefore mostly confined internally through total internal reflection (TIR), where the photon energy is then ultimately lost through collisions or absorption. The condition of TIR ($\theta > \theta_c$) is defined by Snell's law, equation (1.1), and states that an angle of incidence above the critical angle will result in reflection.

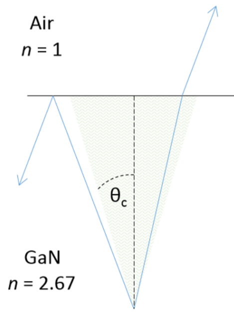

Figure 1.7: Total internal reflection in GaN.

The critical angle of the GaN-air interface is $\sim 23.6°$, defining an extraction cone in each dimension from the origin of the spontaneous emission as in Figure 1.7. The optical performance of III-N LED is therefore constrained by the small proportion ($\frac{1-\cos\theta_c}{2} \approx 0.04$) of generated photon that escape each face of a standard planar device[92].

$$\theta_c = \arcsin\frac{n_{air}}{n_{gan}} \tag{1.1}$$

$\boldsymbol{\theta_c}$ = critical angle

$\mathbf{n_{air}}$ = ambient-air refactive index

$\mathbf{n_{gan}}$ = GaN refractive index

The IQE of a typical InGaN/GaN LED is particularly high (> 80 %), given as the conversion ratio between photon generation and injected carriers[93]. To overcome the large difference between IQE and EQE, a significant improvement in LEE is therefore required.

A number of methods aimed at LEE enhancement have been suggested, including geometric shaping, surface texturing and patterned sapphire substrates (PSS). The basic principle of these methods is to influence change in the angle of incidence, giving reflected and redistributed light additional opportunity to escape at the next interface[92].

A geometric shaping, away from a standard square LED device, results in reduced TIR in the horizontal-plane as consequence of modified incident angle on the non-parallel facets[94]. This has been demonstrated with circular, triangular and lozenge LED structures[93,95,96]; even in three-dimensions as a truncated pyramid[94].

The surface texturing of the substrate, semiconductor and/or current spreading layers allows improved photon diffusion, introducing additional scattering mechanics that influence the subsequent direction of the light[97].

PSS forms a non-planar interface between GaN and the sapphire substrate, requiring epitaxial growth on the ex-situ patterned and etched substrate, resulting in improved crystalline quality[98]. The lower refractive index of sapphire ($n \approx 1.8$) relative to the GaN layer means the optical waveguide effects again confine most light to the semiconductor[99]. A PSS therefore has similar influence as surface texturing, effectively increasing the photon diffusion compared to the planar substrate, improving transmission of propagating light into the sapphire[13].

1.3 References

[1]J. I. Pankove, "GaN: from fundamentals to applications", Materials Science and Engineering: B **61-62**, 305–309 (1999).

[2]S. M. Sze and K. K. Ng, *Physics of Semiconductor Devices*, 3rd ed. (John Wiley & Sons, Inc., New Jersey, 2006).

[3]E. F. Schubert, *Light-Emitting Diodes*, 1st ed. (Cambridge University Press, Cambridge, 2003).

[4]I. P. o. C. C. (IPCC), *Climate Change 2007: The Physical Science Basis*, tech. rep. (United Nations Environment Programme, (UNEP), Nairobi, 2007).

[5]C. Le Quéré, R. M. Andrew, P. Friedlingstein, S. Sitch, J. Hauck, J. Pongratz, P. A. Pickers, J. I. Korsbakken, G. P. Peters, J. G. Canadell, A. Arneth, V. K. Arora, L. Barbero, A. Bastos, L. Bopp, F. Chevallier, L. P. Chini, P. Ciais, S. C. Doney, T. Gkritzalis, D. S. Goll, I. Harris, V. Haverd, F. M. Hoffman, M. Hoppema, R. A. Houghton, G. Hurtt, T. Ilyina, A. K. Jain, T. Johannessen, C. D. Jones, E. Kato, R. F. Keeling, K. K. Goldewijk, P. Landschützer, N. Lefèvre, S. Lienert, Z. Liu, D. Lombardozzi, N. Metzl, D. R. Munro, J. E. M. S. Nabel, S.-i. Nakaoka, C. Neill, A. Olsen, T. Ono, P. Patra, A. Peregon, W. Peters, P. Peylin, B. Pfeil, D. Pierrot, B. Poulter, G. Rehder, L. Resplandy, E. Robertson, M. Rocher, C. Rödenbeck, U. Schuster, J. Schwinger, R. Séférian, I. Skjelvan, T. Steinhoff, A. Sutton, P. P. Tans, H. Tian, B. Tilbrook, F. N. Tubiello, I. T. van der Laan-Luijkx, G. R. van der Werf, N. Viovy, A. P. Walker, A. J. Wiltshire, R. Wright, S. Zaehle, and B. Zheng, "Global Carbon Budget 2018", Earth System Science Data **10**, 2141–2194 (2018).

[6]Department for Business Energy & Industrial Strategy, *Final UK greenhouse gas emissions national statistics: 1990-2017*, tech. rep. February (2019), p. 46.

[7]Department for Business Energy and Industrial Strategy, *Digest of UK Energy Statistics (DUKES): statistics on electricity from generation through to sales*, tech. rep. (2018), pp. 111–153.

[8]D. f. E. (DECC) and C. Change, *The Climate Change Act 2008*, tech. rep. (Parliament of the United Kingdom, London, 2008).

[9]M. A. Moram, "Light-emitting diodes and their applications in energy-saving lighting", Proceedings of the ICE - Energy **164**, 17–24 (2011).

[10]Y. Yuan and M. Krüger, "Polymer-Nanocrystal Hybrid Materials for Light Conversion Applications", Polymers **4**, 1–19 (2011).

[11]International Energy Agency, *Electricity Information 2018: overview*, tech. rep. (2019).

[12]L. Smith, *The phasing out of incandescent light bulbs*, tech. rep. (House of Commons, UK, London, 2010).

[13]Y. Narukawa, M. Ichikawa, D. Sanga, M. Sano, and T. Mukai, "White light emitting diodes with super-high luminous efficacy", Journal of Physics D: Applied Physics **43**, 354002 (2010).

[14]T. W. Murphy, "Maximum Spectral Luminous Efficacy of White Light", (2013).

[15]S. Nakamura, "The Roles of Structural Imperfections in InGaN-Based Blue Light-Emitting Diodes and Laser Diodes", Science **281**, 956–961 (1998).

[16]H. J. Round, "A note on caborundum", Electrical World **49**, 309 (1907).

[17]O. Losev, "Luminous carborundum [silicon carbide] detector and detection with crystals", Telegrafiya i Telefoniya bez Provodov **44**, 485–494 (1927).

[18]N. Zheludev, "The life and times of the LED - a 100-year history", Nature Photonics **1**, 189–192 (2007).

[19]J. Baird and G. Pittman, *Semiconductor radiant diode*, 1962.

[20]N. Holonyak and S. F. Bevacqua, "COHERENT (VISIBLE) LIGHT EMISSION FROM Ga(As1-xPx) JUNCTIONS", Applied Physics Letters **1**, 82 (1962).

[21]H. P. Maruska and J. I. Pankove, "Efficiency of GaAs1 - xPx electroluminescent diodes", Solid-State Electronics **10**, 917–925 (1967).

[22]N. Holonyak, S. F. Bevacqua, C. V. Bielan, and S. J. Lubowski, "The "Direct-Indirect" transition in Ga(As1-xPx) p-n junctions", Applied Physics Letters **3**, 47–49 (1963).

[23]J. a. Edmond, H.-S. Kong, and C. H. Carter, "Blue LEDs, UV photodiodes and high-temperature rectifiers in 6H-SiC", Physica B: Condensed Matter **185**, 453–460 (1993).

[24]E. F. Schubert, *Light-emitting diodes*, 2nd ed. (Cambridge University Press, 2006).

[25]W. C. Johnson, J. B. Parson, and M. C. Crew, "Nitrogen Compounds of Gallium", The Journal of Physical Chemistry **36**, 2651–2654 (1931).

[26] H. P. Maruska and J. J. Tietjen, "The preparation and properties of vapor-deposited single-crystal-line GaN", Applied Physics Letters **15**, 327–329 (1969).

[27] J. I. Pankove, J. E. Berkeyheiser, H. P. Maruska, and J. Wittke, "Luminescent properties of GaN", Solid State Communications **8**, 1051–1053 (1970).

[28] M. R. Lorenz and B. B. Binkowski, "Preparation, Stability, and Luminescence of Gallium Nitride", Journal of The Electrochemical Society **109**, 24 (1962).

[29] J. I. Pankove, E. A. Miller, and J. E. Berkeyheiser, "GaN electroluminescent diodes", in 1971 international electron devices meeting (1971), p. 78.

[30] J. I. Pankove, E. Miller, and J. E. Berkeyheiser, "GaN blue light-emitting diodes", Journal of Luminescence **5**, 84–86 (1972).

[31] H. P. Maruska, W. C. Rhines, and D. Stevenson, "Preparation of Mg-doped GaN diodes exhibiting violet electroluminescence", Materials Research Bulletin **7**, 777–781 (1972).

[32] H. M. Manasevit and W. I. Simpson, "The Use of Metal-Organics in the Preparation of Semiconductor Materials", Journal of The Electrochemical Society **116**, 1725 (1969).

[33] S. Yoshida, S. Misawa, and S. Gonda, "Improvements on the electrical and luminescent properties of reactive molecular beam epitaxially grown GaN films by using AlN-coated sapphire substrates", Applied Physics Letters **42**, 427–429 (1983).

[34] H. Amano, N. Sawaki, I. Akasaki, and Y. Toyoda, "Metalorganic vapor phase epitaxial growth of a high quality GaN film using an AlN buffer layer", Applied Physics Letters **48**, 353 (1986).

[35] I. Akasaki, "Progress in crystal growth and future prospects of group III nitrides by metalorganic vapor-phase epitaxy", Journal of Crystal Growth **195**, 248–251 (1998).

[36] K. Hiramatsu, S. Itoh, H. Amano, I. Akasaki, N. Kuwano, T. Shiraishi, and K. Oki, "Growth mechanism of GaN grown on sapphire with A1N buffer layer by MOVPE", Journal of Crystal Growth **115**, 628–633 (1991).

[37] T. D. Moustakas, R. J. Molnar, T. Lei, G. Menon, and C. R. Eddy, "A Comparative Study of GaN Films Grown on Different Faces of Sapphire by ECR-Assisted MBE", MRS Proceedings **242** (1992).

[38]S. Nakamura, Y. Harada, and M. Seno, "Novel metalorganic chemical vapor deposition system for GaN growth", Applied Physics Letters **58**, 2021–2023 (1991).

[39]S. Nakamura, "GaN Growth Using GaN Buffer Layer", Japanese Journal of Applied Physics **30**, L1705–L1707 (1991).

[40]H. Amano, M. Kito, K. Hiramatsu, and I. Akasaki, "P-Type Conduction in Mg-Doped GaN Treated with Low-Energy Electron Beam Irradiation (LEEBI)", Japanese Journal of Applied Physics **28**, L2112–L2114 (1989).

[41]H. Amano, "Growth and Luminescence Properties of Mg-Doped GaN Prepared by MOVPE", Journal of The Electrochemical Society **137**, 1639 (1990).

[42]S. Nakamura, T. Mukai, M. Senoh, and N. Iwasa, " Thermal Annealing Effects on P-Type Mg-Doped GaN Films ", Japanese Journal of Applied Physics **31**, L139–L142 (1992).

[43]J. a. Van Vechten, J. D. Zook, R. D. Horning, and B. Goldenberg, "Defeating compensation in wide gap semiconductors by growing in H that is removed by low temperature de-ionizing radiation", Japanese Journal of Applied Physics, Part 1: Regular Papers and Short Notes and Review Papers **31**, 3662–3663 (1992).

[44]S. Nakamura and T. Mukai, "High-Quality InGaN Films Grown on GaN Films", Jpn. J. Appl. Phys. **31**, L1457–L1459 (1992).

[45]N. Yoshimoto, T. Matsuoka, T. Sasaki, and a. Katsui, "Photoluminescence of InGaN films grown at high temperature by metalorganic vapor phase epitaxy", Applied Physics Letters **59**, 2251 (1991).

[46]S. Nakamura, T. Mukai, and M. Senoh, "Candela-class high-brightness InGaN / AlGaN double-heterostructure blue-light-emitting diodes", Applied Physics Letters **64**, 1687 (1994).

[47]S. Nakamura, M. Senoh, N. Iwasa, and S.-i. Nagahama, "High-Brightness InGaN Blue, Green and Yellow Light-Emitting Diodes with Quantum Well Structures", Japanese Journal of Applied Physics **34**, L797–L799 (1995).

[48]Nobelprize.org, *The Nobel Prize in Physics 2014*, 2014.

[49]R. M. Smith, B. Liu, J. Bai, and T. Wang, "Temperature dependence of non-radiative energy transfer in hybrid structures of InGaN/GaN nanorods and F8BT films", Applied Physics Letters **105**, 171111 (2014).

[50] M. Athanasiou, R. M. Smith, S. Ghataora, and T. Wang, “Polarized White Light from Hybrid Organic/III-Nitrides Grating Structures”, Scientific Reports **7**, 39677 (2017).

[51] S. Ghataora, R. M. Smith, M. Athanasiou, and T. Wang, “Electrically Injected Hybrid Organic/Inorganic III-Nitride White Light-Emitting Diodes with Nonradiative Förster Resonance Energy Transfer”, ACS Photonics **5**, 642–647 (2018).

[52] H. Nakanotani, K. Masui, J. Nishide, T. Shibata, and C. Adachi, “Promising operational stability of high-efficiency organic light-emitting diodes based on thermally activated delayed fluorescence.”, Scientific reports **3**, 2127 (2013).

[53] H. Sahoo, “Förster resonance energy transfer - A spectroscopic nanoruler: Principle and applications”, Journal of Photochemistry and Photobiology C: Photochemistry Reviews **12**, 20–30 (2011).

[54] J. J. Rindermann, G. Pozina, B. Monemar, L. Hultman, H. Amano, and P. G. Lagoudakis, “Dependence of resonance energy transfer on exciton dimensionality”, Physical Review Letters **107**, 1–5 (2011).

[55] R. Smith, B. Liu, J. Bai, and T. Wang, “Hybrid III-Nitride/Organic Semiconductor Nanostructure with High Efficiency Nonradiative Energy Transfer for White Light Emitters”, Nano Letters **13**, 3042–3047 (2013).

[56] M. Achermann, M. a. Petruska, D. D. Koleske, M. H. Crawford, and V. I. Klimov, “Nanocrystal-based light-emitting diodes utilizing high-efficiency nonradiative energy transfer for color conversion”, Nano Letters **6**, 1396–1400 (2006).

[57] N. J. Findlay, J. Bruckbauer, A. R. Inigo, B. Breig, S. Arumugam, D. J. Wallis, R. W. Martin, and P. J. Skabara, “An organic down-converting material for white-light emission from hybrid LEDs.”, Advanced materials (Deerfield Beach, Fla.) **26**, 7290–7294 (2014).

[58] Boston Applied Technologies Inc., *Technical Specification - YAG:Ce*, Woburn, Massachusetts, 2015.

[59] Hyunchae Chun, P. Manousiadis, S. Rajbhandari, D. A. Vithanage, G. Faulkner, D. Tsonev, J. J. D. McKendry, S. Videv, Enyuan Xie, Erdan Gu, M. D. Dawson, H. Haas, G. A. Turnbull, I. D. W. Samuel, and D. C. O’Brien, “Visible Light Communication Using a Blue GaN μLED and Fluorescent Polymer Color Converter”, IEEE Photonics Technology Letters **26**, 2035–2038 (2014).

[60]Z. Zhuang, Y. Li, B. Liu, X. Guo, J. Dai, G. Zhang, T. Tao, T. Zhi, Z. Xie, H. Ge, Y. Shi, Y. Zheng, and R. Zhang, "Optical polarization characteristics of c -plane InGaN/GaN asymmetric nanostructures", Journal of Applied Physics **118**, 233111 (2015).

[61]Z. Zheng, K. H. Yim, M. S. M. Saifullah, M. E. Welland, R. H. Friend, J. S. Kim, and W. T. S. Huck, "Uniaxial alignment of liquid-crystalline conjugated polymers by nanoconfinement", Nano Letters **7**, 987–992 (2007).

[62]S. a. Schmid, K. H. Yim, M. H. Chang, Z. Zheng, W. T. S. Huck, R. H. Friend, J. S. Kim, and L. M. Herz, "Polarization anisotropy dynamics for thin films of a conjugated polymer aligned by nanoimprinting", Physical Review B **77**, 115338 (2008).

[63]G. R. Hayes, I. D. W. Samuel, and R. T. Phillips, "Exciton dynamics in electroluminescent polymers studied by femtosecond time-resolved photoluminescence spectroscopy", Physical Review B **52**, 569–572 (1995).

[64]P. Lane, "Polyfluorene Electroluminescence", in *Organic light-emitting devices: a survey*, edited by J. Shinar, 1st ed. (Springer-Verlag New York, Inc., New York, 2004) Chap. 10, pp. 265–299.

[65]M. T. Hill, Y.-S. Oei, B. Smalbrugge, Y. Zhu, T. de Vries, P. J. van Veldhoven, F. W. M. van Otten, T. J. Eijkemans, J. P. Turkiewicz, H. de Waardt, E. J. Geluk, S.-H. Kwon, Y.-H. Lee, R. Nötzel, and M. K. Smit, "Lasing in metallic-coated nanocavities", Nature Photonics **1**, 589–594 (2007).

[66]S. Nakamura and G. Fasol, *The Blue Laser Diode: GaN Based Light Emitters and Lasers* (Springer, Berlin, 1997).

[67]F. K. Yam, L. L. Low, S. A. Oh, and Z. Hassan, "Gallium Nitride: An Overview of Structural Defects", Optoelectronics - Materials and Techniques, 99–136 (2011).

[68]J. W. Orton and C. T. Foxon, "Group III nitride semiconductors for short wavelength light-emitting devices", Reports on Progress in Physics **61**, 1–75 (1999).

[69]D. Feezell and S. Nakamura, "Nonpolar and semipolar group III-nitride lasers", in *Semiconductor lasers* (Elsevier, 2013), pp. 221–271.

[70]H. Morkoç, *Handbook of Nitride Semiconductors and Devices: Volume 1 - Materials Properties, Physics and Growth*, 1st ed. (John Wiley & Sons, Inc., Hoboken, New Jersey, 2008), pp. 1–1322.

[71]S. Fischer, C. Wetzel, W. L. Hansen, E. D. Bourret-Courchesne, B. K. Meyer, and E. E. Haller, "Properties of GaN grown at high rates on sapphire and on 6H-SiC", Applied Physics Letters **69**, 2716–2718 (1996).

[72]R. Dwiliński, R. Doradziński, J. Garczyński, L. Sierzputowski, R. Kucharski, M. Zajac, M. Rudziński, R. Kudrawiec, W. Strupiński, and J. Misiewicz, "Ammonothermal GaN substrates: Growth accomplishments and applications", physica status solidi (a) **208**, 1489–1493 (2011).

[73]V. Dmitriev and A. Usikov, "Hydride Vapor Phase Epitaxy of Group III Nitride Materials", in *Iii-nitride: semiconductor materials*, edited by Z. C. Feng, 1st ed. (Imperial College Press, London, 2006) Chap. 1, pp. 1–40.

[74]E. S. Hellman, "The Polarity of GaN: a Critical Review", MRS Internet Journal of Nitride Semiconductor Research **3**, 1–10 (1998).

[75]C. G. Van de Walle, M. D. McCluskey, C. P. Master, L. T. Romano, and N. M. Johnson, "Large and composition-dependent band gap bowing in InxGa1xN alloys", Materials Science and Engineering: B **59**, 274–278 (1999).

[76]S. Nakamura, T. Mukai, M. Senoh, S.-i. Nagahama, and N. Iwasa, "InxGa(1x)N / InyGa(1y)N superlattices grown on GaN films", Journal of Applied Physics **74**, 3911 (1993).

[77]T. Takeuchi, S. Sota, M. Katsuragawa, M. Komori, H. Takeuchi, H. Amano, and I. Akasaki, "Quantum-Confined Stark Effect due to Piezoelectric Fields in GaInN Strained Quantum Wells", Japanese Journal of Applied Physics **36**, L382–L385 (1997).

[78]S. F. Chichibu, A. C. Abare, M. P. Mack, M. S. Minsky, T. Deguchi, D. Cohen, P. Kozodoy, S. B. Fleischer, S. Keller, J. S. Speck, J. E. Bowers, E. Hu, U. K. Mishra, L. Coldren, S. P. DenBaars, K. Wada, T. Sota, and S. Nakamura, "Optical properties of InGaN quantum wells", Materials Science and Engineering: B **59**, 298–306 (1999).

[79]T. Langer, A. Kruse, F. A. Ketzer, A. Schwiegel, L. Hoffmann, H. Jönen, H. Bremers, U. Rossow, and A. Hangleiter, "Origin of the "green gap": Increasing nonradiative recombination in indium-rich GaInN/GaN quantum well structures", physica status solidi (c) **8**, 2170–2172 (2011).

[80]M. Auf der Maur, A. Pecchia, G. Penazzi, W. Rodrigues, and A. Di Carlo, “Efficiency Drop in Green InGaN/GaN Light Emitting Diodes: The Role of Random Alloy Fluctuations”, Physical Review Letters **116**, 027401 (2016).

[81]M. R. Krames, O. B. Shchekin, R. Mueller-Mach, G. O. Mueller, L. Zhou, G. Harbers, and M. G. Craford, “Status and Future of High-Power Light-Emitting Diodes for Solid-State Lighting”, Journal of Display Technology **3**, 160–175 (2007).

[82]S. Keller, B. P. Keller, D. Kapolnek, A. C. Abare, H. Masui, L. A. Coldren, U. K. Mishra, and S. P. Den Baars, “Growth and characterization of bulk InGaN films and quantum wells”, Applied Physics Letters **68**, 3147–3149 (1996).

[83]T. Takeuchi, H. Amano, and I. Akasaki, “Theoretical study of orientation dependence of piezoelectric effects in wurtzite strained GaInN/GaN heterostructures and quantum wells”, Japanese Journal of Applied Physics, Part 1: Regular Papers and Short Notes and Review Papers **39**, 413–416 (2000).

[84]a. D. Bykhovski, B. L. Gelmont, and M. S. Shur, “Elastic strain relaxation and piezoeffect in GaN-AlN, GaN-AlGaN and GaN-InGaN superlattices”, Journal of Applied Physics **81**, 6332 (1997).

[85]Q. Wang, J. Bai, Y. P. Gong, and T. Wang, “Influence of strain relaxation on the optical properties of InGaN/GaN multiple quantum well nanorods”, Journal of Physics D: Applied Physics **44**, 395102 (2011).

[86]J. Cho, E. F. Schubert, and J. K. Kim, “Efficiency droop in light-emitting diodes: Challenges and countermeasures”, Laser & Photonics Reviews **7**, 408–421 (2013).

[87]Y. C. Shen, G. O. Mueller, S. Watanabe, N. F. Gardner, a. Munkholm, and M. R. Krames, “Auger recombination in InGaN measured by photoluminescence”, Applied Physics Letters **91**, 24–27 (2007).

[88]J. Iveland, L. Martinelli, J. Peretti, J. S. Speck, and C. Weisbuch, “Direct measurement of auger electrons emitted from a semiconductor light-emitting diode under electrical injection: Identification of the dominant mechanism for efficiency droop”, Physical Review Letters **110**, 1–5 (2013).

[89]J. Hader, J. V. Moloney, and S. W. Koch, “Temperature-dependence of the internal efficiency droop in GaN-based diodes”, Applied Physics Letters **99**, 2014–2017 (2011).

[90]J. Hader, J. V. Moloney, and S. W. Koch, "Density-activated defect recombination as a possible explanation for the efficiency droop in GaN-based light emitters", 2011 Conference on Lasers and Electro-Optics Europe and 12th European Quantum Electronics Conference, CLEO EUROPE/EQEC 2011, 1–3 (2011).

[91]T. K. Kim, S. H. Kim, S. S. Yang, J. K. Son, K. H. Lee, Y. G. Hong, K. H. Shim, J. W. Yang, K. Y. Lim, S. J. Bae, and G. M. Yang, "GaN-based light-emitting diode with textured indium tin oxide transparent layer coated with Al[sub 2]O[sub 3] powder", Applied Physics Letters **94**, 161107 (2009).

[92]C. Wiesmann, K. Bergenek, N. Linder, and U. T. Schwarz, "Photonic crystal LEDs - Designing light extraction", Laser and Photonics Reviews **3**, 262–286 (2009).

[93]J.-Y. K. J.-Y. Kim, M.-K. K. M.-K. Kwon, J.-P. K. J.-P. Kim, and S.-J. P. S.-J. Park, "Enhanced Light Extraction From Triangular GaN-Based Light-Emitting Diodes", IEEE Photonics Technology Letters **19**, 1865–1867 (2007).

[94]B. Sun, L. Zhao, T. Wei, X. Yi, Z. Liu, G. Wang, and J. Li, "Shape designing for light extraction enhancement bulk-GaN light-emitting diodes", Journal of Applied Physics **113** (2013).

[95]X. H. Wang, W. Y. Fu, P. T. Lai, and H. W. Choi, "Evaluation of InGaN/GaN light-emitting diodes of circular geometry.", Optics express **17**, 22311–22319 (2009).

[96]Dong-Hyun Jang, Jong-In Shim, and Dong-Soo Shin, "Enhancement of Light Extraction Efficiency Using Lozenge-Shaped GaN-Based Light-Emitting Diodes", IEEE Photonics Technology Letters **21**, 760–762 (2009).

[97]M. Y. Hsieh, C. Y. Wang, L. Y. Chen, T. P. Lin, M. Y. Ke, Y. W. Cheng, Y. C. Yu, C. P. Chen, D. M. Yeh, C. F. Lu, C. F. Huang, C. C. Yang, and J. J. Huang, "Improvement of external extraction efficiency in GaN-based LEDs by SiO2 nanosphere lithography", IEEE Electron Device Letters **29**, 658–660 (2008).

[98]Y.-J. Lee, T.-C. Lu, H.-C. Kuo, and S.-C. Wang, "High Brightness GaN-Based Light-Emitting Diodes", Journal of Display Technology **3**, 118–125 (2007).

[99]I. H. MALITSON, F. V. MURPHY, JR., and W. S. RODNEY, "Refractive Index of Synthetic Sapphire", Journal of the Optical Society of America **48**, 72 (1958).

Chapter 2

Background Information

2.1 Background Information

2.1.1 Isolated Atoms

The Bohr atomic model describes isolated atoms with discrete bound negatively charged electron clouds around a nucleus of positive charge, where stationary electron orbital positions are defined such that an electron's angular momentum is contained to integer multiples ($\geq$ 1) of $\frac{h}{2\pi}$[1].

The de Broglie relationship, equation (2.1), considers the wave-like behaviour of electrons and relates the wavelength (λ) inversely proportional to the particle's momentum (p). This means quantised electron energy levels can instead be defined by standing waves that conform an integer number of wavelengths that fit the orbital circumference[2]. The Planck–Einstein relation, equation (2.2), then defines quantised energy of massless particles relative to their oscillation frequency ($\nu = \frac{c}{\lambda}$) in multiples of the Planck's constant (6.63x10^{-34} Js)[3].

$$\lambda = \frac{h}{p} \tag{2.1}$$
$$E = \frac{hc}{\lambda} \tag{2.2}$$

$\boldsymbol{\lambda}$ = wavelength

h = Planck's constant $(6.63 \times 10^{-34}\ Js)$

p = particle momentum

E = energy

c = speed of light $(3.00 \times 10^{8}\ ms^{-1})$

An atom consists of different orbitals that can each accommodate only a predefined number of degenerate electrons. These ground orbitals are S (2), P (6), D (10), and F (14) listed in order of increasing energy with the total quantity of electrons succeeding in brackets. Electrons naturally first fill the most favourable low energy states. This is controlled in part by the Pauli exclusion principle, which states no two identical fermions can concurrently inhabit the same quantum state[4]. However, electrons demonstrate spin, a property somewhat synonymous to the principles of electromagnetism. Electron spin is a quantised angular momentum, exhibiting a magnetic field moment, acting in parallel (spin-up) and anti-parallel

(spin-down) directions. This means in actuality each quantum state can contain two electrons, each with opposite spin.

2.1.2 Crystal Structure

The energetically favourable condition of an atom is to have a completed outer valence band orbital. To satisfy this neighbouring atoms share electrons in covalent bonds. It is therefore no longer valid to consider the system as an isolated atom.

This interaction of valence electrons between atoms describes their structural position in a highly ordered crystal lattice, characterised by its unit cell. A unit cell is the primitive volume that can be repeated as a periodic array to form the correct three-dimensional crystal structure[5]. The arrangement of atoms in the solid-state determine the material's many physical characteristics, which include its electrical, optical and mechanical properties[6].

III-N materials can exist with a primitive wurtzite, zincblende and rock-salt cell structure[7,8]. However, in application III-nitrides primarily exist in a wurtzite structure as a result of its improved thermodynamic stability under ambient conditions; this study is therefore limited to wurtzite structures.

The hexagonal wurtzite unit cell consists of two-sets of atoms arranged tetrahedrally, four N atoms centred on a single group-III, and vice-versa. The III-N wurtzite crystal then exists as interpenetrating group-III and N sub-lattices stacked sequentially in a hexagonal closed-pack (HCP) lattice, both demonstrated in Figure 2.1. This means neighbouring planes are positioned horizontally so that the separation in the c-axis, perpendicular to the unit cell hexagons, is at a minimum[5].

Table 2.1: Lattice parameters of wurtzite GaN, InN, AlN and sapphire (Al_2O_3)[7].

	a (Å)	c (Å)	$\frac{c}{a}$
GaN	3.189	5.185	1.626
InN	3.544	5.718	1.613
AlN	3.111	4.978	1.600
Al_2O_3	4.758	12.991	2.730

As in table 2.1, wurtzite is characterised by lattice parameters a, b and c. The hexagonal symmetry means that $a = b \neq c$, where a and b are the inter-atomic distances in the hexagonal plane and c is the inter-atomic distance in the c-axis[7].

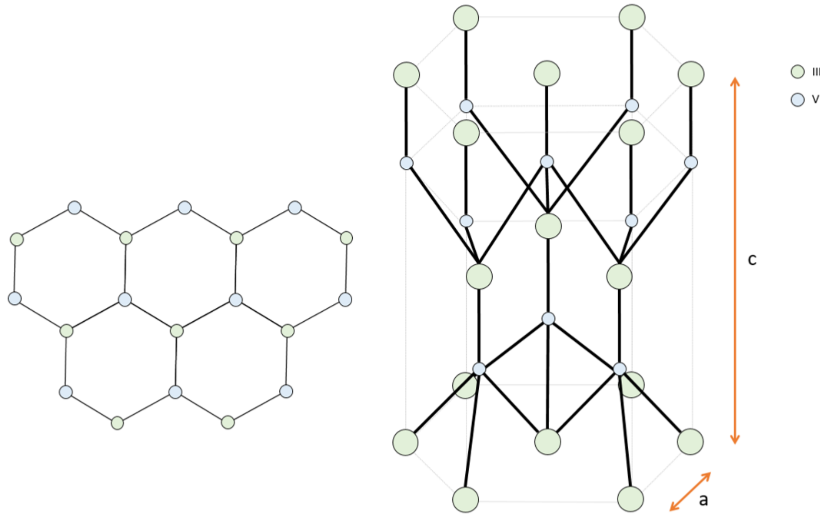

Figure 2.1: III-N hexagonal closed-pack lattice and primitive wurtzite unit cell.

2.1.3 Bandstructure

In the solid-state, as N atoms are brought together, individual quantised energy levels divide (Pauli exclusion principle) to give N unique energy levels. Two seemingly continuous energy bands are ultimately formed in the case of a large number of atoms, which are the conduction band (CB) and valence band (VB). The VB consists of the states of all bound electrons, which have insufficient free energy to move unrestricted through the lattice, whereas the unoccupied energy states available to free electrons complete the CB.

The CB and VB are isolated by a forbidden energy band-gap, in which no available energy states exist. The band-gap is defined as the difference between the lowest CB and highest VB energy levels, equation (2.3), quantifying the minimum energy required to promote a VB electron to the CB.

$$E_g = E_c - E_v \tag{2.3}$$

$\mathbf{E_g}$ = band-gap energy

$\mathbf{E_c}$ = conduction band minima

$\mathbf{E_v}$ = valence band maxima

The Fermi-Dirac distribution, equation (2.4), provides the statistical distribu-

tion of fermions (electrons) with respect to energy, giving the energy states probability it is occupied[9,10].

$$F(E) = \frac{1}{1 + exp(\frac{E-E_F}{k_B T})} \tag{2.4}$$

$\mathbf{F(E)}$ = Fermi-Dirac distribution

$\mathbf{E_F}$ = Fermi level

$\mathbf{k_B}$ = Boltzmann constant $(1.38 \times 10^{-23}\ JK^{-1})$

$\mathbf{T}$ = absolute temperature

The bandstructure is typically represented by the dispersion relationship, which relates energy as a function of angular spatial frequency (wavenumber), and therefore momentum, from equations (2.5) and (2.6).

$$k = \frac{2\pi}{\lambda} \tag{2.5}$$

$$k = \frac{p}{\hbar} \tag{2.6}$$

$\mathbf{k}$ = wavenumber

$\boldsymbol{\hbar}$ = reduced Planck's constant $(1.05 \times 10^{-34}\ Js)$

2.1.4 Semiconductors

The band-gap of a material is the fundamental parameter that distinguishes conductors, semiconductors and insulators. A semiconductor has properties between a conductor and insulator, which allow and prohibit the flow of electric charge, respectively. Conduction is only possible where an energy band isn't completely occupied or unoccupied.

At $T = 0$ K a conductor consists of a singular partially-filled energy band, where the VB and CB overlap. This allows electrical conduction, independent of temperature, because charged carriers can flow freely within the material.

$$n = N_c exp(-\frac{E_c - E_F}{k_B T}) \tag{2.7}$$

$$p = N_v exp(-\frac{E_F - E_v}{k_B T}) \tag{2.8}$$

$\mathbf{n}$ = electron density

$\mathbf{N_c}$ = conduction band density of states

$\mathbf{p}$ = hole density

$\mathbf{N_v}$ = valence band density of states

In the same conditions the CB of a semiconductor and insulator is completely unoccupied, whereas the VB is fully populated. However, the typical band-gap of a semiconductor is in the range of 0.3 - 3.5 eV, where an insulators band-gap is significantly larger. This means, from equation (2.7) and (2.8), that under ambient temperatures a small number of valence electrons in a semiconductor have sufficient thermal energy to cross the band-gap in conduction.

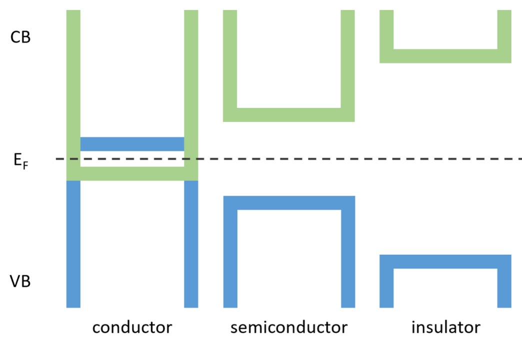

Figure 2.2: Bandstructure of a conductor, semiconductor and insulator.

The Fermi level is defined by the energy level at which the probability a state is populated is $\frac{1}{2}$ at any value of T, where $E = E_F$ in equation (2.4). At absolute zero temperature ($T = 0$ K) the Fermi-Dirac distribution gives $F(E) = 0$ for $E > E_F$ and $F(E) = 1$ for $E < E_F$[11].

The Fermi level is therefore equivalent to an hypothetical electron energy of the bulk material, despite that it may not actually correspond to an allowed state. It is understood that the Fermi level of a conductor exists within that singular partially filled energy band, whereas in an insulator and intrinsic semiconductor the Fermi level occurs within the band-gap, shown in Figure 2.2.

2.1.5 Carrier Concentration

A material's ability to conduct electrical charge is quantified by its conductivity, equal to the reciprocal of resistivity, which expresses how much the material re-

stricts current flow.

$$\sigma = ne\mu_n \tag{2.9}$$

$$\sigma = ne\mu_n + pe\mu_p \tag{2.10}$$

$\boldsymbol{\sigma}$ = electrical conductivity

$\mathbf{e}$ = elementary charge constant $(1.60 \times 10^{-19}\ C)$

$\boldsymbol{\mu_n}$ = electron mobility

$\boldsymbol{\mu_p}$ = hole mobility

The material's conductivity is highly dependent on both carrier concentration and mobility, equation (2.9). This relation is adjusted to equation (2.10), where electrons and holes contribute individually to conduction, each with a unique carrier mobility. The carrier mobility is a material constant that describes the ease at which a carrier travels through the lattice with respect to an applied E-field.

A semiconductor has an electrical conductivity between a conductor ($\sigma > 10^3$ Scm^{-1}) and an insulator ($\sigma < 10^{-8}$ Scm^{-1})[12].

In the excitation of a valence electron to the CB, an electron hole is produced in the VB; a hole being the absence of an electron in a position within the crystal lattice that would allow one. This generates in intrinsic semiconductors electron-hole pairs so $n_i = n = p$.

$$n_i = \sqrt{N_c N_v} exp(-\frac{E_g}{2k_B T}) \tag{2.11}$$

$\mathbf{n_i}$ = intrinsic carrier density

The free carrier concentration in semiconductor materials is controllable, and therefore so is its conductivity, from equation (2.11). This is an average between the electron and hole concentration in the respective CB and VB of equation (2.7) and (2.8), where the density of states (N_c and N_v) are a concentration coefficient across the energy bands. The concept of doping involves the generation of an excess of these active electrons (n-type) or holes (p-type) within the semiconductor, increasing the free carrier concentration at equilibrium.

III-V materials, like GaN, contain group-III (Ga) and group-V (N) elements that have three and five valence electrons, respectively.

Increasing electron concentration in n-type doping involves substituting group-III with group-IV (Si) donor atoms, donating one additional negatively charged free electron to the CB. P-type doping conversely involves replacing group-III with group-II (Mg) acceptor atoms in increasing the hole concentration, creating one additional positively charged vacancy in the VB[13]. Therefore the donor (N_D) and acceptor (N_A) atom density incorporated into the material directly relates to the concentration of free carriers, assuming complete ionisation at $T \neq 0$ K[5]. The additional shallow impurities introduced are weakly-bound, forming new sites slightly below CB (electrons) and above VB (holes), such that $k_B T$ is sufficient to ionise the carrier to the respective energy band. This causing the Fermi level to increase in n-type and decrease in p-type materials as they fill the CB and VB density of states (DOS), respectively.

It is therefore practicable to control σ through doping the intrinsic crystal lattice.

2.1.6 Direct and Indirect Band-Gap

The bandstructure of a solid is classified as having either a direct or indirect band-gap, as in Figure 2.3. The CB minimum (E_c) and VB maximum (E_v) both exist at the same wavenumber (k = 0) in direct band-gap materials, otherwise it has an indirect band-gap. The significance of a direct and indirect band-gap relates to the conservation of momentum in recombination of carriers between bands.

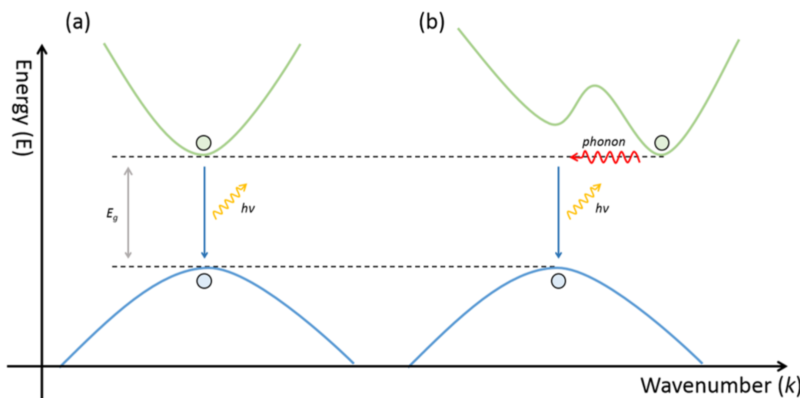

Figure 2.3: Representation of (a) direct and (b) indirect band-gap.

The electrons moved to the conduction band ultimately relax to the valence state through recombination of an electron-hole pair as it is more energetically favourable[6]. This is achieved by loss of excess energy equivalent to the band-gap (E_g) by radiative or non-radiative processes, considering that no states exist between the CB and VB. The radiative recombination of an electron-hole pair releases the change in energy across the band-gap as a photon with an emission wavelength given by equation (2.2).

The electrons and holes collect, respectively, at the lowest available energy states along the band-edge of the CB and VB; electrons and holes require the same momentum in order to recombine[6]. The carriers in a direct band-gap material therefore combine directly. However, the negligible momentum of a photon, with respect of an electron, mean that an indirect band-gap system also requires a phonon. This makes recombination in an indirect band-gap material a 2nd-order action and therefore the radiative lifetime is much larger, resulting from the limited transitional probability[6].

The competition between radiative and non-radiative dynamics is quantified by the internal quantum efficiency (IQE) using equation (2.13). IQE gives the probability of radiative recombination relative to the total number of electron-hole pairs generated, which equals the total probability of recombination from equation (2.12).

$$\frac{1}{\tau} = \frac{1}{\tau_r} + \frac{1}{\tau_{nr}} \tag{2.12}$$

$$\eta_{IQE} = \frac{1}{\tau_r} \Big/ \frac{1}{\tau} \tag{2.13}$$

$\boldsymbol{\tau}$ = total recombination lifetime

$\boldsymbol{\tau_{\mathrm{r}}}$ = radiative lifetime

$\boldsymbol{\tau_{\mathrm{nr}}}$ = non-radiative lifetime

$\boldsymbol{\eta_{\mathrm{IQE}}}$ = internal quantum efficiency

In equilibrium, with no external stimulant, the condition under the law of mass action states $n_i^2 = n_0 p_0$ is valid. This law implies that the rate of reaction is proportional to the product of the reactants. Introduction of excess carriers into the material, through light absorption or current injection, disturbs the equilibrium condition such that $n = n_0 + \delta n$ and $p = p_0 + \delta p$, demonstrated in Figure 2.4.

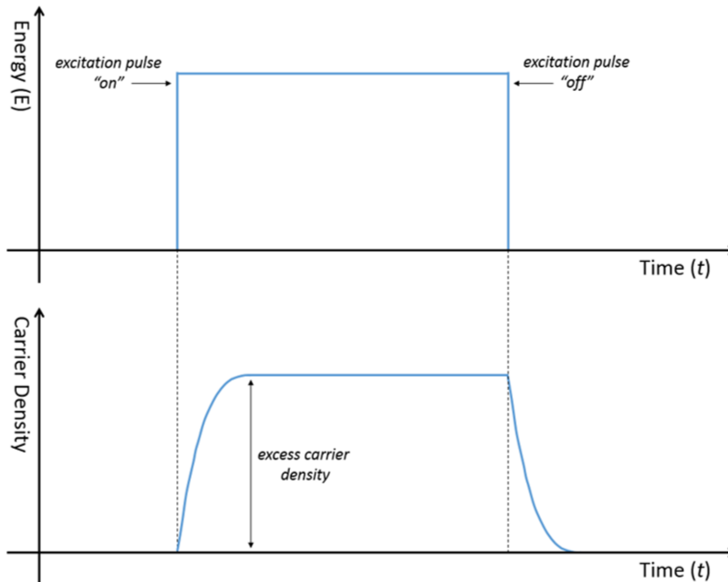

Figure 2.4: Change in carrier density in response to an excitation pulse.

This deviation from equilibrium is only temporary as mechanics occur to restore it, which involves the recombination of the significant number of minority carriers injected. The recombination rate, as in equation (2.14), shows that this process is proportional to electron and hole density by the bimolecular recombination constant ($10^{-9} - 10^{-11}$ $cm^3 s^{-1}$)[14].

The rate of recombination is ultimately controlled by the carrier lifetime (τ), which gives the mean time between generation and recombination of a minority carrier.

$$R = \beta(n_0 + \delta n)(p_0 + \delta p) \tag{2.14}$$

$\mathbf{R}$ = recombination rate

$\boldsymbol{\beta}$ = bimolecular recombination coeffecient

$\mathbf{n_0}$ = equilibrium electron density

$\boldsymbol{\delta}\mathbf{n}$ = excess electron density

$\mathbf{p_0}$ = equilibrium hole density

$\boldsymbol{\delta}\mathbf{p}$ = excess hole density

2.1.7 Optical Transitions

The transition of an excited electron back to the VB in recombination can occur through different radiative and non-radiative action, shown in Figure 2.5. Radiative mechanics include band-edge, exciton and impurity centre recombination; whereas non-radiative processes include Shockley-Read-Hall (SRH) and Auger recombination.

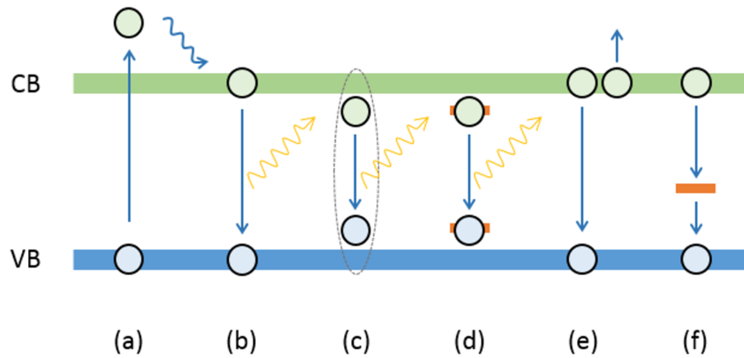

Figure 2.5: Generation-recombination mechanics (a) absorption ($E > E_g$), (b) spontaneous band-edge, (c) exciton, (d) donor-acceptor impurity, (e) non-radiative Auger and (f) non-radiative Shockley-Read-Hall recombination.

(a). Introduction of energy above the band-gap so that $E > E_g$, through optical absorption or current injection, generates excited free electron-hole pairs beyond the band-edge. The high energy carriers rapidly relax through thermalisation, multiple phonon emission, to a more favourable energy level at the band-edge.

(b). Spontaneous radiative recombination of an electron-hole pair across the band-gap, where equivalent energy lost in the action is converted to a photon defined by equation (2.2).

(c). The radiative recombination of a free (Wannier-Mott) exciton in emission of a photon with energy less than the band-gap ($E_g - E_n$), where the free exciton binding energy E_n is given by equation (2.15). An exciton is a neutral bound electron-hole pair, generated at the same point in space, attracted by electrostatic coulomb interaction of the oppositely charged carriers. The

exciton can therefore transfer energy through the crystal lattice without a net electrical charge[6].

A stable exciton is generated when the exciton binding energy is sufficient to remain bound at room temperature ($T = 293$ K), such that $E_n > k_B T$. GaN has a free exciton binding energy of $E_n \approx 25$ meV, and $k_B T \approx 25$ meV, meaning room temperature stable exciton are possible[6].

$$E_n = -\frac{\mu}{m_0}\frac{1}{\varepsilon_r^2}\frac{R_H}{n^2} \tag{2.15}$$

$\mathbf{E_n}$ = exciton binding energy

$\boldsymbol{\mu}$ = reduced electron-hole mass

$\mathbf{m_0}$ = invariant mass

$\boldsymbol{\varepsilon_r}$ = relative dielectric constant

$\mathbf{R_H}$ = Rydberg energy of hydrogen $(13.6\ eV)$

$\mathbf{n}$ = principal quantum number

An exciton exists in two basic formations, the Frenkel (bound) and Wannier-Mott (free) exciton[15,16]:

- A Frenkel exciton is tightly bound, with a small exciton radius expanding a size comparable to the inter-atomic spacing. This means the Frenkel exciton is less mobile since it is associated to particular atoms or molecules, transporting by hopping between atomic sites within the crystal. This type of exciton typically only exists in insulator and molecular crystals[17].
- The Wannier-Mott exciton has a large exciton radius, which encompasses many atoms. The electron-hole pair is therefore only weakly bound and has a low exciton binding energy. This type of exciton is primarily found only in inorganic semiconductor crystals. A Wannier-Mott exciton is a delocalised state and can travel freely within the crystal, where it doesn't associate with any one particular atom or molecule[6].

(d). The donor-acceptor radiative electron-hole recombination between fixed energy states that result from impurity centres introduced by dopant atoms; photon energy is less than the bulk material band-gap by the dopant activation energy[18].

(e). Auger recombination is a non-radiative action that involves the transfer of the process energy and momentum to a third charged particle (electron or hole), promoting the third carrier deep into the respective energy band[5]. The energetic carrier will ultimately lose this excess energy and return to the band-edge through multiple phonon emission. Auger recombination, a three-particle interaction, is therefore statistically more dominant at increasing carrier density; a particular problem in LED and proposed cause of efficiency droop[19].

(f). Shockley-Read-Hall non-radiative recombination of carriers at energy level traps distributed within the forbidden region of the band-gap through phonon involvement. The recombination centres are caused by imperfections in the crystal lattice, interrupting its periodicity that otherwise defines the bandstructure[20,21]. The crystal defects, typically unavoidable and occur during growth, are characterised by dimensionality[22]:

Zero-Dimension: Point defects occur at a single point in the crystal lattice, one atomic site, which include vacancy and interstitial atoms.

One-Dimension: Linear defects include edge, screw and mixed dislocations that result from a sudden change in the atomic order, disrupting the lattice along a single line.

Two-Dimension: Planar defects are imperfections related to an area, including grain boundaries and stacking faults, typically where different crystal structures transition.

Surface non-radiative recombination, similarly, occurs due to an immediate discontinuity along the semiconductor surface. At the interface atomic bonding changes in absence of neighbouring atoms, resulting in partially complete electron orbitals, creating many localised recombination energy states.

Three-Dimension: Bulk defects are affiliated to a volume, including voids and inclusions, regions of space either vacant of atoms or completed

with foreign atoms.

2.2 Light-Emitting Diode

The light-emitting diode (LED) is a fundamental semiconductor optoelectronic device; Figure 2.6 demonstrates it existing typically as an active light-emitting region between n-type and p-type material[14]. The active region is a low-dimensional structure, providing quantum confinement in direction of any plane on the order of the de Broglie wavelength (λ_d), as in equation (2.1). A low-dimensional structure provides discrete energy states in the same dimension (X, Y and Z), such that the particle's wavefunction is confined as a standing wave, resulting in a quantisation of its motion[6].

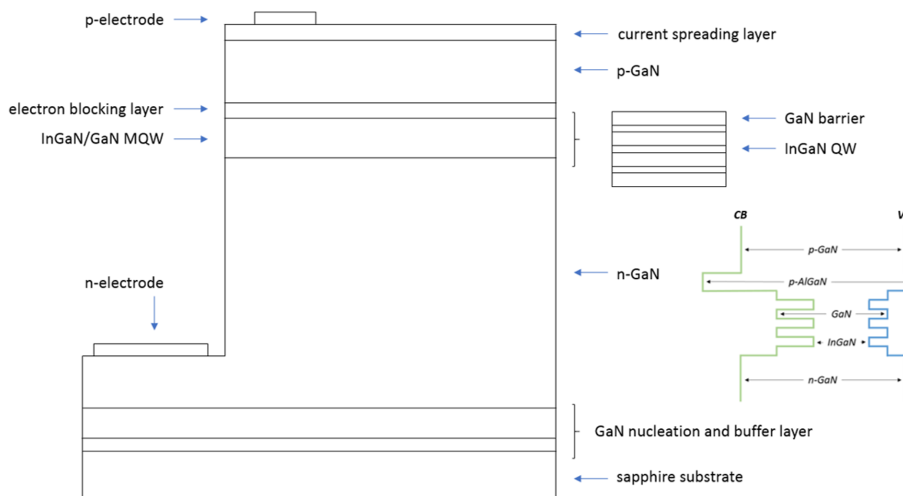

Figure 2.6: Standard light-emitting diode structure and inset corresponding bandstructure (not to scale).

The system geometry therefore determines the confinement dimensionality, as in Figure 2.7[6]:

Zero-Dimension: Quantum dot (QD) provides complete carrier confinement in all three-dimensions, electrons and holes are unable to move free in any direction.

One-Dimension: Quantum wire allows electrons and holes to travel along one axis, with carrier confinement in the remaining two-dimensions.

Two-Dimension: Quantum well (QW) restricts motion of free carriers in one-dimension, particles can move throughout a confined two-dimensional area.

Three-Dimension: Bulk material is without carrier confinement in any of the three-dimensions, excited carriers can travel free in all directions.

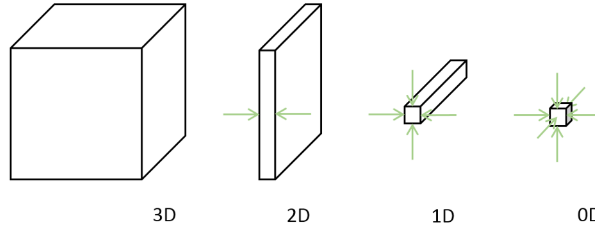

Figure 2.7: Quantum confinement and confinement dimensionality.

The quantum well is typically employed in an LED, such that a thin ($L \approx \lambda_d$) layer of a low band-gap material (InGaN) is grown between a large band-gap material (GaN)[23]. This is a form of double heterostructure, providing confinement in the direction of growth.

The n-type and p-type GaN, under forward bias, provide a respective high concentration of electrons and holes to the active region, which exists at the PN-junction interface to trap both carriers. Localised confinement of electron-hole pair to a quantum well increases the respective carrier wavefunction overlap across the active region, resulting in the enhanced probability of recombination. The photon emission energy is therefore a function of the same discrete state of the QW, where quantised energy of a quantum well, assumed infinitely deep, is given in equation (2.16).

$$E_n = \frac{1}{2m^*}(\frac{\pi\hbar n}{L})^2 \tag{2.16}$$

$\mathbf{E_n}$ = discrete quantum well energy

$\mathbf{m}^*$ = effective particle mass

$\mathbf{L}$ = quantum well thickness

A higher principal quantum number (n) results in a higher quantised energy, as shown in Figure 2.8. The solution is a result of using the Schrödinger wave

equation to identify permitted energy states of the free-particles confined to an infinite square well potential, particle-in-a-box problem. The wave equation $\Psi(x,t)$, equation (2.17), collapses at $x = 0$ and $x = L$ so that standing waves form between boundary conditions, simplifying to an isolated region at zero potential $V(x) = 0$[24].

$$\Psi(x,t) = \sqrt{\frac{2}{L}} sin(\frac{n\pi}{L}x) exp(\frac{iE_n t}{\hbar}) \tag{2.17}$$

$\boldsymbol{\Psi(x,t)}$ = Schrödinger wave equation

x = positon

t = time

This however provides only an approximation of a more complicated quantum system, where finite potential wells in reality cannot confine particles so definitively. The Schrödinger wave equation instead gives a solution that now extends within the classically forbidden region, associating non-zero probability to finding the particle even when its energy is less than the potential barrier. This quantum tunnelling has the effect of lowering the corresponding quantised energy levels as the effective potential well length (L) increases. The density of states (DOS) then considers just the number of these available discrete energy level in relation to unit volume, dependent on confinement dimensionality.

An InGaN/GaN QW double heterostructure permits a band-gap engineering through control of the thickness (L), again in Figure 2.8, and ternary alloy composition of the active low band-gap region[23]. The $In_xGa_{(1-x)}N$ alloy system, despite an $\sim$11 % lattice mismatch between GaN ($a = 3.189$ Å) and InN ($a = 3.544$ Å), allows growth of intermediate layers not exceeding the critical-layer thickness, limiting L. The critical thickness of the InGaN layer is the point when it is no longer psuedomorphically strained to match the properties of GaN, past the critical thickness strain relaxation occurs through formation of crystalline defects[25].

A single-quantum well (SQW) typically exhibits a saturated optical intensity as the injected carrier density increases, caused when the carrier concentration within the active region increases sufficiently to fill its small finite DOS. The carrier overflow of the SQW can therefore be improved by increasing the QW thickness or implementation of a multiple quantum well (MQW) structure[14]. A comparatively thick large band-gap material barrier is required between each QW in order to decouple their wavefunction and disallow quantum tunnelling. To further prevent

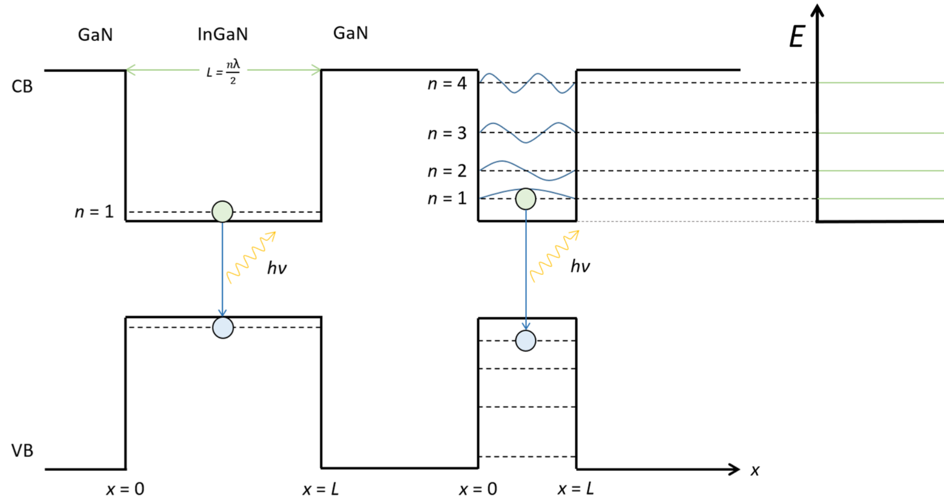

Figure 2.8: Quantisation of particle wavefunctions in a quantum well structure with respect to thickness.

carrier leakage in the active region an electron blocking layer (EBL), with an even higher band-gap material (p-AlGaN), is typically grown at its interface with the p-type material[14].

$$E_{InGaN}(x) = xE_{InN} + (1-x)E_{GaN} - bx(1-x) \tag{2.18}$$

$\mathbf{E_{InGaN}}$ = InGaN band-gap energy

$\mathbf{x}$ = indium mole fraction

$\mathbf{E_{InN}}$ = InN band-gap energy $(0.7\ eV)$

$\mathbf{E_{GaN}}$ = GaN band-gap energy $(3.4\ eV)$

$\mathbf{b}$ = bowing parameter $(1.4\ eV)$

The $In_xGa_{(1-x)}N$ band-gap as a function of the indium mole fraction from Vegard's law, equation (2.18), which indicates that emission energy is an intermediate between the constituent binary compounds[25]. The band-gap increases with respect to a lower indium mole fraction, where the quantity of GaN ($E_{GaN} = 3.4$ eV) increases and InN ($E_{InN} = 0.7$ eV) decreases, tending towards the GaN band-gap. A single-valued bowing parameter ($b = 1.4$ eV), across the complete alloy composition range, accommodates for the bowed deviation of the band-gap with relation to the linear combination of InN and GaN[26].

2.2.1 Semiconductor PN-Junction

The Fermi level is a bulk material property, such that under equilibrium a system of different laminated materials equalise to a single value. Electrons in a material with the higher Fermi level will move to occupy the lower energetically favourable states within its neighbouring material. The charge transfer across the junction causes the conduction and valence band to bend at the interface, bringing into coincidence the two individual Fermi level[14], demonstrated in Figure 2.9.

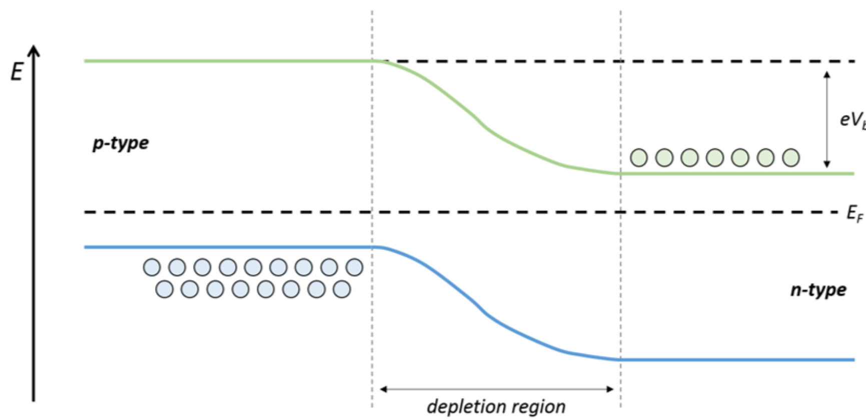

Figure 2.9: Bandstructure of an unbiased PN-Junction.

Equilibrium in the PN-junction results from the built-in electrostatic potential (V_b) across a depletion region, which acts to oppose further diffusion of majority carriers. The depletion region, an area void of free carriers, occurs because of the positive-donor and negative-acceptor atom ionisation caused by recombination at the interface of the n-type and p-type regions, respectively. This prevents light emission, until $V = V_b = \frac{E_g}{e}$, since the device is otherwise absent of areas with any significant density of both free electrons and holes[27].

The built-in potential of the PN-junction, prohibits flow of electrical current in one-direction. In forward bias the electrostatic potential across the depletion region decreases ($V_b - V(t)$), reducing the potential barrier height as the Fermi level of the p-type and n-type region shift to reduce band-bending. This allowing current flow and efficient carrier injection into the active region for electroluminescence (EL). The opposite occurs under reverse bias, such that the applied voltage acts to increase the potential barrier height and depletion region width ($V_b - (-V(t))$).

2.2.2 White Light-Emitting Diode

Luminous efficacy (η_l), equation (2.20), is a physiological measure that determines the effectiveness of a light source to stimulate the human eye. The human eye sensitivity ($V(\lambda)$) is a wavelength-dependent parabolic function, which peaks to unity at 555 nm and tends to 0 at the limits of the visible spectrum. The visible light spectrum extends from an approximate 390 nm to 720 nm wavelength in the electromagnetic spectrum[5].

$$\Phi_V(\lambda) = \eta_0 \int V(\lambda)P(\lambda)\delta(\lambda) \tag{2.19}$$

$$\eta_l(\lambda) = \frac{\Phi_V(\lambda)}{P} \tag{2.20}$$

$\mathbf{\Phi_V(\lambda)}$ = luminous flux

$\boldsymbol{\eta_0}$ = maximum luminous efficacy (683 lmW^{-1})

$\boldsymbol{V(\lambda)}$ = CIE photoptic eye sensitivity function

$\boldsymbol{P(\lambda)}$ = spectral output power

$\boldsymbol{\eta_l}$ = luminous efficacy

P = input power

The luminous flux (Φ_V) quantifies the detected visible light of the human eye, equation (2.19), where η_0 scales the function to the maximum luminous efficacy value (683 lm/W) at 555 nm[14]. The theoretical limit of luminous efficacy for white light is therefore lower, on the range of 250 lm/W to 370 lm/W, contingent on spectral length and perceived quality of white light[28].

White light is the combination of all wavelengths across the entire visible spectrum. The Commission Internationale de l'Eclairage (CIE) develop means to objectively measure colour using eye sensitivity function and chromaticity diagrams. A standardised white light includes black-body radiation with spectrum characterised by temperature; plotted on the chromaticity diagram from its centre ($x = \frac{1}{3}, y = \frac{1}{3}$) to monochromatic red[14,29].

The chromaticity co-ordinates, correlated colour temperature (CCT) and colour-rendering index (CRI) are all quantitative measurements of a light source. CCT is the temperature along the Planckian locus nearest to the lights chromaticity co-ordinates; and CRI is a measure of an illuminants ability to render true colours of

an object with relation to a standardised reference source, with highest possible CRI (100)[14].

A high-energy emitting blue InGaN/GaN LED coupled to a single yellow down-conversion material acts to produce dichromatic white light emission, as in Figure 2.10. The principle of a down-conversion material is photoluminescence (PL), which involves absorption of high-energy photon from an optical source and re-emission at longer wavelength[5]. The optimised intensity ratio of the LED and down-converting material, through concentration and thickness, allow control of the luminous efficacy and CRI. This down-conversion material is typically a powdered YAG ($Y_3Al_5O_12 : Ce^{3+}$) phosphor, requiring the optically-active rare-earth cerium (Ce) ion dopant[14]. A similar method involves the radiative excitation of a red, green and blue triphosphor combination of down-converting materials with a single high-energy wavelength ultraviolet (UV) LED. The practical advantages of using a single LED and passive light-emitting materials, where cost is comparable to the LED alone, mean this form of white LED is most commercially prevalent[7].

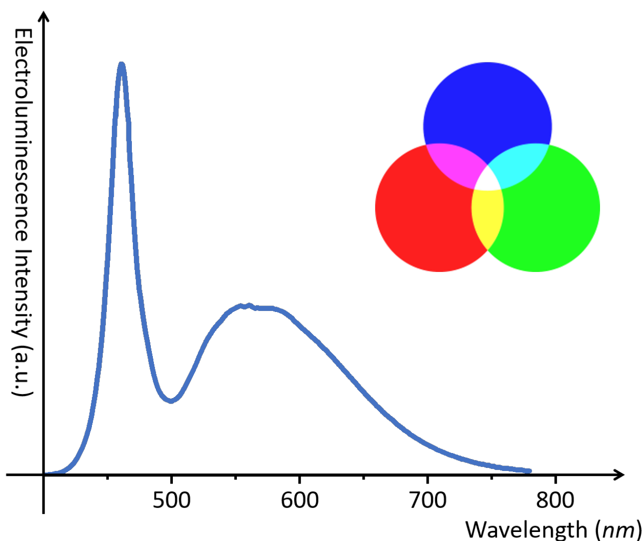

Figure 2.10: Emission spectrum of a typical dichromatic down-conversion white LED and inset RGB colour model[30].

The yellow emission YAG phosphor has a typical peak wavelength at 545 nm and a broad full width at half maximum (FWHM) of ~150 nm, potentially leading to self-absorption due to a small Stokes-shift[30]. YAG phosphors also have high

material stability, quick fluorescence lifetime decay ($\sim$70 ns), relatively low material synthesis cost and high quantum efficiency (> 85 %) under blue InGaN/GaN LED excitation[31,32]. The CRI of the dichromatic blue-yellow LED is limited to ($\sim$85) as a result of long-wavelength red deficiency, which also restricts the CCT to high "cold blue-white" temperature emission[30]. In addition the typically large grain size of the YAG phosphor ($\sim$5 μm) can prohibit use of light-emitting devices of a comparable scale[31].

A trichromatic LED is an alternative method to producing white light, avoiding use of down-converting material. The trichromatic LED consists of three independently driven primary colour (red/green/blue) LED, each emitting characteristic narrow bandwidth light, overlapping across entire spectrum[7].

2.3 Laser Diode

A laser diode (LD) emits electromagnetic radiation through a stimulated emission optical amplification; theoretical foundations were first conceptualised using probability coefficients for absorption, spontaneous emission and stimulated emission rates[33].

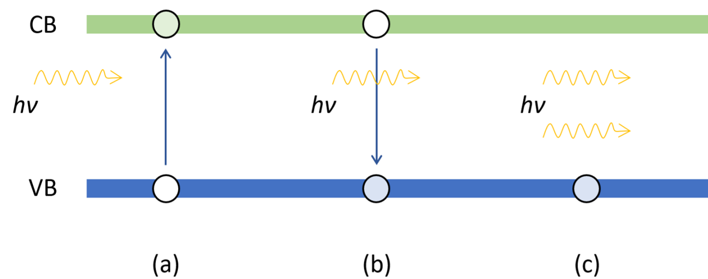

Figure 2.11: Mechanics of stimulated emission (a) absorption ($E \geq E_g$), (b) stimulated recombination and (c) stimulated emission.

Stimulated emission, as shown in Figure 2.11, involves the instantaneous recombination of an excited atom to ground state through the stimulating presence of an incident photon that is not then absorbed, inciting the generation of a second coherent photon[5,34]; this is a basic consideration for optical gain. The rate of stimulated emission is therefore proportionate to the light density and number of excited carriers at the higher energy level, stimulated emission mechanics can only dominate above absorption through a population inversion. This requires that

a greater population exists in the conduction band than the unexcited lower energy state, impossible at thermal equilibrium. Maintaining this condition after optical loss (absorption and scattering) means a continuous amplification in the emission intensity is then possible. Lasing is achieved above a threshold where stimulated emission is greater than the spontaneous emission rate, discussed previously in section 2.1.7.

As population inversion requires the system to deviate from thermal equilibrium an external means to enter the unnaturally occurring non-equilibrated state is necessary, involving either high-power optical or electrical excitation, promoting greater than half of all free carriers to the upper energy level.

The increasing photon density can however be attained with an optical resonator, confining light to the cavity, improving further the rate of interaction between incident photon and excited electron-hole pair. Coherence then means that these photon generated through stimulated emission maintain equivalent properties to allow interference[5]. The simplest form of optical resonator is the plane-parallel Fabry-Pérot cavity, where light is fed-back through multi-reflections between two facets that produce standing waves at the systems resonant frequencies, causing oscillations with greater intensity[35].

The optical cavity is designed to have large quality factor (Q), quantifying the ability to confine light with low attenuation, defined in equation (2.21) as a ratio between resonant wavelength and FWHM bandwidth.

$$Q = \frac{\lambda}{\Delta\lambda} \tag{2.21}$$

$\mathbf{Q}$ = quality factor

$\boldsymbol{\Delta\lambda}$ = bandwidth

2.3.1 Purcell Effect

Peak emission wavelength of a semiconductor laser diode is a material property. The cavity design can however allow control and enhancement of photon interactions by matching it to the resonant frequency[36]. Excited atoms can nevertheless still transition to the ground-state through spontaneous emission, producing instead incoherent photon, which are still similarly maintained within the laser gain-medium.

A decreasing cavity geometry relative to the emission wavelength modifies the spontaneous emission rate compared to free-space through a phenomenon known as the Purcell effect[37], improving the lasing threshold and therefore modulation speed as a result[38]. This is because it has the effect of increasing the spontaneous emission coupled to the lasing mode (β-factor)[39], which from equation (2.23) compares the spontaneous emission rate into the discrete cavity mode with the remaining free-space[40]. The result is higher optical-gain at a given population inversion, determined by the fraction of output intensity below and above threshold, leading to noticeable reduction in the device operating power.

This spontaneous emission rate enhancement, or Purcell factor (F_p), is proportionate to the ratio of the Q-factor and effective cavity mode volume (V_{eff}), as shown in equation (2.22)[37].

$$F_p = \frac{3}{4\pi^2}(\frac{\lambda}{n_c})^3 \frac{Q}{V_{eff}} \tag{2.22}$$

$$F_p = \frac{\beta}{1-\beta} \tag{2.23}$$

$\mathbf{F_p}$ = Purcell factor

$\mathbf{n_c}$ = cavity refractive index

$\mathbf{V_{eff}}$ = effective cavity mode volume

$\boldsymbol{\beta}$ = spontaneous emission coupling factor

A smallest effective volume therefore has the most significant effect. This is because as spatial dimensions decrease on order of the emission wavelength, discrete optical mode form, synonymous to the quantisation of particle wavefunction as in section 2.2. A spontaneous transition can therefore only occur across the cavities supported optical modes, limited by the decreasing geometry, which has the effect of increasing the spontaneous emission coupling factor accordingly[34]. The spontaneous and stimulated emission of a sufficiently small cavity allows them to then purposefully exist at the same resonant frequency, enhancing the light output to even a single optical mode.

An optical resonator mode is a self-consistent electric-field distribution, reproducing itself during propagation.

2.3.2 Whispering Gallery Mode

An optical resonator with circular geometry can sustain "whispering gallery mode" (WGM) with sufficient refractive index step outside the cavity, unlike the Fabry-Pérot cavity photon are instead confined under TIR conditions[35,41]. Light circulates continuously around the circumference of the resonator above critical angle interactions as described by Snell's law. This concept was first observed using sound-waves travelling the Whispering Gallery of St. Paul's Cathedral (UK), stating sound can only occur at defined points (nodes) along the circumference[42]. The same wave-like behaviour means at the cavity resonant wavelength light will similarly propagate tangentially to the perimeter, intensity again increasing through a constructive interference over repeated round-trip. A WGM is formed of an integer number of internal standing waves equivalent to the cavity circumference from a wave-mechanics description[43]. This on condition that to provide vertical confinement the gain material thickness is less than $\frac{\lambda}{2n_c}$, demonstrating a 2D waveguide behaviour.

The number of optical mode resonance that coincide with the spontaneous emission spectrum of the lasing medium is directly related to the cavity size. The spacing between successive resonant modes is determined for a circular cavity using the free spectral range equation, equation (2.24), where a reduction in the optical resonator radius (R) gives an increased mode separation.

$$\Delta\lambda_{FSR} = \frac{\lambda^2}{2\pi R n_c} \tag{2.24}$$

$\mathbf{\Delta\lambda_{FSR}}$ = free spectral range

$\mathbf{R}$ = optical cavity radius

This potential for creating a small effective cavity mode volume then leads to the possibility of low-threshold and threshold-less lasing; though legitimate threshold-less lasing is not expected to be even possible in room-temperature application[36]. The term is instead more often used to identify lasers with a near unity spontaneous emission coupling factor and almost negligible non-radiative recombination[44]. To achieve lasing, where $\beta \neq 1$, optical gain above the transparency condition is first required, such that stimulated emission is greater than

cavity absorption and losses[45]. The carrier density that is required to attain this condition then determines the threshold[46]. A threshold-less laser would therefore still require finite excitation power in order to reach the coherent emission regime, even though threshold characteristic do not appear in an otherwise linear input-output curve[40,47,48].

2.4 Organic Semiconductors

An organic material is a carbon-based molecular compound, including combination with other elements.

A molecular orbital (MO) is formed when distinct atomic electron orbitals overlap in covalent bonds. The interaction of electron orbitals in a single carbon (C) atom results in formation of hybridised atomic orbitals, with new energy and shape, generating increased orbital overlap in MO formation. The hybridisation of C ($1s^2 2s^2 2p^2$) involves promotion of a single $2s$ electron to one of the three $2p$ orbital ($1s^2 2s^1 2p^3$). This then causing the remaining $2s$ electron to hybridise with either one (sp), two (sp^2) or three (sp^3) of the $2p$ orbital.

Organic semiconductors have properties analogous to classical inorganic semiconductors; existing as molecules mean that the bandstructure is instead defined by its MO. The highest occupied molecular orbital (HOMO) is the last MO with both quantum states filled, synonymous to the valence band. The next incomplete MO above the HOMO, under ground state, is the lowest unoccupied molecular orbital (LUMO), which is similarly referred to as the conduction band, as shown in Figure 2.12. The difference in energy between the LUMO and HOMO of an organic semiconductor is therefore also termed the band-gap.

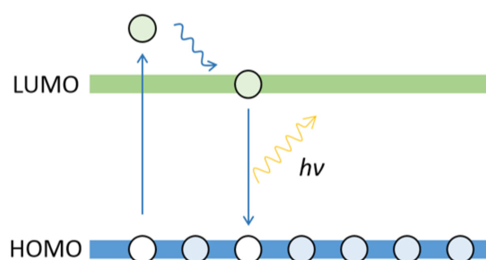

Figure 2.12: HOMO and LUMO molecular bandstructure; including absorption ($E > E_g$), phonon relaxation and radiative band-edge emission.

The prominence of organic semiconductors coincided with the first demonstration of low DC-bias (< 10 V) electroluminescence (EL) from an organic light-emitting diode (OLED), with a thin-film heterostructure emitting layer[49]. The first organic light-emitting devices before this had recorded EL up to $\sim$400 V_{DC}[50]. The efficiency of such devices then improved greatly through development of alternative organic light-emitting materials (π-conjugated polymers), with functional band-gap energy[51].

A π-conjugated polymer has carbon atoms that alternate either between single-double or single-triple bonds. In such a system the remaining unhybridised p orbitals of adjacent atoms overlap, producing π bonds, causing a delocalisation of the orbital along the entire molecular chain[52], as demonstrated in Figure 2.13. The π-conjugated polymer makes it possible to achieve small band-gaps in range of 1.5 eV to 3.0 eV, typical of a semiconductor[53]. This is because energy of π electron are usually higher than σ bond electron, which have strong covalent bonds with an in-plane overlap between atomic or hybrid orbitals[52].

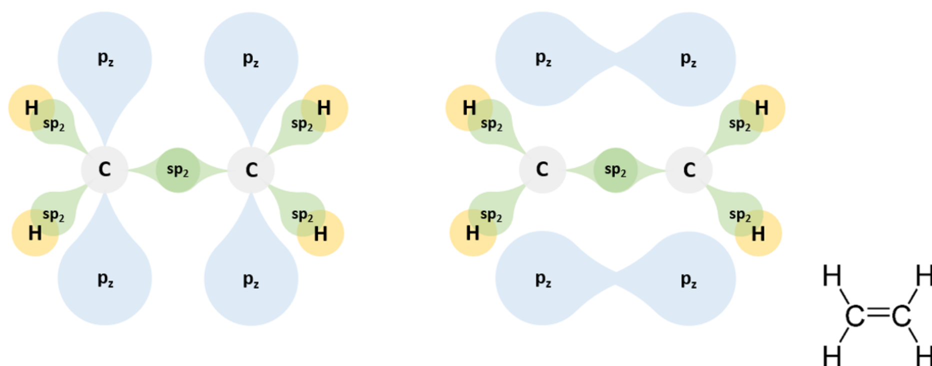

Figure 2.13: Hybridised hydrocarbon (ethylene) showing P_z (left) and delocalised π (right) orbital.

The conduction of charged carriers within organic molecules occur through intra-molecular and inter-molecular transport. Intra-molecular transport involves conduction through delocalised π orbital bonds within the molecule; whereas inter-molecular transport requires carriers to hop (quantum tunnel) between adjacent molecules. The mobility (μ) of an organic material is therefore highly dependent on the arrangement of its molecules, with typical values (< 10 $cm^2V^{-1}s^{-1}$) much lower than inorganic semiconductors[54].

2.4.1 Hybrid Organic/Inorganic White Light-Emitting Diode

A hybrid organic/inorganic light-emitting diode combines the complimentary advantages of the organic light-emitting polymer and inorganic LED[55]. The basic configuration, achieving white light emission, involves the partial down-conversion of electrically injected blue InGaN/GaN QW LED by the organic material. A prerequisite is the overlap between the polymer absorption band and narrow inorganic LED emission spectrum[56,57].

The photoluminescence of organic polymers results in high fluorescence quantum yield of up to unity, with formation of only singlet-states[58]. A singlet-state means the spin of an excited electron maintains pairing with its matched ground-state electron (Pauli exclusion principle). The fluorescence quantum efficiency of an OLED under electroluminescence (EL) is limited by phosphorescence to 0.25, assuming one singlet-state is formed to every three triplet-state; experimentation finding this value is slightly improved[59,60]. The decay lifetime of an excited singlet-state to its ground-state is significantly faster acting ($\sim$ ns), where triplet-states ($\sim$ ms) require additional improbable transition between states with different spin multiplicity through an intersystem crossing[61].

This is because triplet-states, with electron-spin flipped from its ground state, are determined by rules of multiplicity ($2s+1$). The angular momentum of two paired fermion (electron), $\frac{1}{2}$-integer spin particles, are in either parallel ($+\frac{1}{2}$) or anti-parallel ($-\frac{1}{2}$) directions. The total angular momentum (s) in the singlet-state and triplet-state equalling to $s=0$ and $s=1$, respectively.

A combination of III-nitrides and conjugated polymers, with respective high-performance electronic and photoluminescent-optical properties, is therefore an attractive proposition in efficient solid-state lighting[62]. However, the one significant benefit to using organics over phosphor down-converting materials is the highly-efficient non-radiative Förster resonance energy transfer (FRET)[55].

2.4.2 Förster Resonance Energy Transfer

FRET involves the near-field dipole-dipole coupling between the interface of InGaN/GaN QW (donor) and organic light-emitting polymer (acceptor)[63,64]. The basic principle involves radiation-less electronic energy transfer between Wannier-Mott (inorganic) and Frenkel (organic) excitons[65]. The excited acceptor-dipole then radiatively recombines at rates faster than FRET, which therefore prohibits

FRET in the direction of the inorganic device[64,66]. This avoids intermediate steps preceding the photoluminescence of the down-converting material, which before absorption includes photon emission and extraction in the inorganic LED[55].

The difficultly of FRET is the requirement of the sufficiently close proximity (< 10 nm) between the donor and acceptor dipole[67]. The structure of the inorganic LED is therefore of significant importance in the demonstration of FRET[58].

The FRET rate is defined as $k_f \propto R^{-P}$, where R is dipole-dipole separation and P is determined by the coupling dimensionality of the dipole-dipole interaction[65]. The separation is described such that FRET occurs before the donor exciton recombine and relax to its ground state[68].

FRET is typically characterised using temperature-dependent and time-resolved PL studies, observing changes in the QW and correlating them to differences in the organic material[58,65].

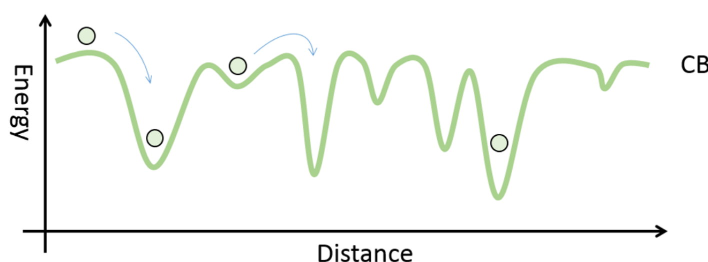

Figure 2.14: Bandstructure fluctuations and carrier localisation.

The FRET in a temperature-dependent study of an organic/inorganic hybrid device will demonstrate similar strong temperature-dependent properties of the inorganic InGaN QW, distinct to the organic polymer alone[58]. A typical InGaN/GaN QW structure exhibits a temperature-dependent IQE, related to localisation and thermal delocalisation of exciton. This is caused by compositional inhomogeneity and thickness variation in the QW that results in fluctuations within the bandstructure, affecting considerably the exciton properties as in Figure 2.14[69]. At low thermal energy ($k_B T$) the exciton can be localised (trapped) to potential minima within the bandstructure. This means that the exciton dimensionality can potentially transition, with increasing T, from a single-point (0D, $P = 4$) QD dipole to delocalised planar (2D, $P = 2$) QW dipole; having significant positive influence on the FRET rate[65,70].

The time-resolved measurements will evidence an increased decay rate in a

hybrid light-emitting device, which is otherwise absent without FRET[71], discussed in chapters 4 and 5.

2.5 References

[1]N. Bohr, "LXXIII. On the constitution of atoms and molecules", Philosophical Magazine Series 6 **26**, 857–875 (1913).

[2]P. Weinberger, "Revisiting Louis de Broglie's famous 1924 paper in the Philosophical Magazine", Philosophical magazine letters **86**, 405–410 (2006).

[3]M. Planck, "On the Law of Distribution of Energy in the Normal Spectrum", Annalen der Physik **4**, 553–563 (1901).

[4]W. Pauli, "Über den Zusammenhang des Abschlusses der Elektronengruppen im Atom mit der Komplexstruktur der Spektren", Zeitschrift für Physik **31**, 765–783 (1925).

[5]S. M. Sze and K. K. Ng, *Physics of Semiconductor Devices*, 3rd ed. (John Wiley & Sons, Inc., New Jersey, 2006).

[6]M. Fox, *Optical Properties of Solids*, 2nd ed. (Oxford University Press, Oxford, 2010).

[7]S. Nakamura and G. Fasol, *The Blue Laser Diode: GaN Based Light Emitters and Lasers* (Springer, Berlin, 1997).

[8]H. Xia, Q. Xia, and A. L. Ruoff, "High-pressure structure of gallium nitride: Wurtzite-to-rocksalt phase transition", Physical Review B **47**, 12925–12928 (1993).

[9]P. A. M. Dirac, "On the Theory of Quantum Mechanics", Proceedings of the Royal Society A: Mathematical, Physical and Engineering Sciences **112**, 661–677 (1926).

[10]E.Fermi, "On the Quantization of the Monoatomic Ideal Gas", Rend. Lincei **3**, 145–149 (1926).

[11]A. Kumar, *Introduction to Solid State Physics*, 2nd ed. (PHI Learning, New Dehli, 2010).

[12]W. Bolton, *Materials for Engineering*, 2nd ed. (Taylor & Francis Ltd., Oxford, 2000).

[13]V. Dmitriev and A. Usikov, "Hydride Vapor Phase Epitaxy of Group III Nitride Materials", in *Iii-nitride: semiconductor materials*, edited by Z. C. Feng, 1st ed. (Imperial College Press, London, 2006) Chap. 1, pp. 1–40.

[14]E. F. Schubert, *Light-Emitting Diodes*, 1st ed. (Cambridge University Press, Cambridge, 2003).

[15]J. Frenkel, “On the Transformation of light into Heat in Solids”, Physical Review **37**, 17–44 (1931).

[16]G. H. Wannier, “The Structure of Electronic Excitation Levels in Insulating Crystals”, Physical Review **52**, 191–197 (1937).

[17]W. Y. Liang, “Excitons”, Physics Education **5**, 3 (1970).

[18]M. a. Reshchikov and H. Morkoç, “Luminescence properties of defects in GaN”, Journal of Applied Physics **97**, 61301 (2005).

[19]J. Iveland, L. Martinelli, J. Peretti, J. S. Speck, and C. Weisbuch, “Direct measurement of auger electrons emitted from a semiconductor light-emitting diode under electrical injection: Identification of the dominant mechanism for efficiency droop”, Physical Review Letters **110**, 1–5 (2013).

[20]W. Shockley and W. T. Read, “Statistics of the Recombination of Holes and Electrons”, Physical Review **87**, 835–842 (1952).

[21]R. N. Hall, “Electron-Hole Recombination in Germanium”, Physical Review **87**, 387 (1952).

[22]F. K. Yam, L. L. Low, S. A. Oh, and Z. Hassan, “Gallium Nitride: An Overview of Structural Defects”, Optoelectronics - Materials and Techniques, 99–136 (2011).

[23]S. Nakamura, M. Senoh, N. Iwasa, and S.-i. Nagahama, “High-Brightness InGaN Blue, Green and Yellow Light-Emitting Diodes with Quantum Well Structures”, Japanese Journal of Applied Physics **34**, L797–L799 (1995).

[24]A. Phillips, *Introduction to Quantum Mechanics*, edited by D. J. SANDIFORD, F. MANDL, and A. C. PHILLIPS (John Wiley & Sons, Inc., 2003).

[25]C. G. Van de Walle, M. D. McCluskey, C. P. Master, L. T. Romano, and N. M. Johnson, “Large and composition-dependent band gap bowing in InxGa1xN alloys”, Materials Science and Engineering: B **59**, 274–278 (1999).

[26]J. Wu, “When group-III nitrides go infrared: New properties and perspectives”, Journal of Applied Physics **106**, 11101 (2009).

[27]S. Prasad, H. Schumacher, and A. Gopinath, *High-Speed Electronics and Optoelectronics: Devices and Circuits*, 1st ed. (Cambridge University Press, Cambridge, 2009).

[28]T. W. Murphy, “Maximum Spectral Luminous Efficacy of White Light”, (2013).

[29]M. Planck, "On the theory of the energy distribution law of the normal spectrum", Verhandlungen der Deutschen Physikalischen Gesellschaft **2**, 237–245 (1900).

[30]Y. Narukawa, M. Ichikawa, D. Sanga, M. Sano, and T. Mukai, "White light emitting diodes with super-high luminous efficacy", Journal of Physics D: Applied Physics **43**, 354002 (2010).

[31]Boston Applied Technologies Inc., *Technical Specification - YAG:Ce*, Woburn, Massachusetts, 2015.

[32]A. A. Setlur, "Phosphors for LED-based Solid-State Lighting", Electrochemical Society Interface **18**, 32–36 (2009).

[33]A. Einstein, "Zur Quantentheorie der Strahlung (On the Quantum Theory of Radiation)", Phys. Z. **18**, 121–128 (1917).

[34]L. A. Coldren, S. W. Corzine, and M. L. Mašanović, *Diode Lasers and Photonic Integrated Circuits* (John Wiley & Sons, Inc., Hoboken, NJ, USA, Mar. 2012).

[35]K. J. Vahala, "Optical microcavities", Nature **424**, 839–846 (2003).

[36]S. Noda, "Seeking the Ultimate Nanolaser", Science **314**, 260–261 (2006).

[37]E. M. Purcell, H. C. Torrey, and R. V. Pound, "Resonance Absorption by Nuclear Magnetic Moments in a Solid", Physical Review **69**, 37–38 (1946).

[38]B. Romeira and A. Fiore, "Purcell Effect in the Stimulated and Spontaneous Emission Rates of Nanoscale Semiconductor Lasers", IEEE Journal of Quantum Electronics **54**, 1–12 (2018).

[39]Q. Gu, B. Slutsky, F. Vallini, J. S. T. Smalley, M. P. Nezhad, N. C. Frateschi, and Y. Fainman, "Purcell effect in sub-wavelength semiconductor lasers", Optics Express **21**, 15603 (2013).

[40]W. W. Chow and S. Reitzenstein, "Quantum-optical influences in optoelectronics—An introduction", Applied Physics Reviews **5**, 041302 (2018).

[41]Y. Rakovich and J. Donegan, "Photonic atoms and molecules", Laser & Photonics Reviews **4**, 179–191 (2009).

[42]L. Rayleigh, "CXII. The problem of the whispering gallery", The London, Edinburgh, and Dublin Philosophical Magazine and Journal of Science **20**, 1001–1004 (1910).

[43]R. Symes, R. M. Sayer, and J. P. Reid, "Cavity enhanced droplet spectroscopy: Principles, perspectives and prospects", Physical Chemistry Chemical Physics **6**, 474 (2004).

[44]I. Prieto, J. M. Llorens, L. E. Muñoz-Camúñez, A. G. Taboada, J. Canet-Ferrer, J. M. Ripalda, C. Robles, G. Muñoz-Matutano, J. P. Martínez-Pastor, and P. A. Postigo, "Near thresholdless laser operation at room temperature", Optica **2**, 66 (2015).

[45]G. Björk, A. Karlsson, and Y. Yamamoto, "Definition of a laser threshold", Physical Review A **50**, 1675–1680 (1994).

[46]E. F. Schubert, *Light-emitting diodes*, 2nd ed. (Cambridge University Press, 2006).

[47]S. T. Jagsch, N. V. Triviño, F. Lohof, G. Callsen, S. Kalinowski, I. M. Rousseau, R. Barzel, J. F. Carlin, F. Jahnke, R. Butté, C. Gies, A. Hoffmann, N. Grandjean, and S. Reitzenstein, "A quantum optical study of thresholdless lasing features in high-β nitride nanobeam cavities", Nature Communications **9** (2018).

[48]M. Khajavikhan, A. Simic, M. Katz, J. H. Lee, B. Slutsky, A. Mizrahi, V. Lomakin, and Y. Fainman, "Thresholdless nanoscale coaxial lasers", Nature **482**, 204–207 (2012).

[49]C. W. Tang and S. a. Vanslyke, "Organic electroluminescent diodes", Applied Physics Letters **51**, 913–915 (1987).

[50]M. Pope, H. P. Kallmann, and P. Magnante, "Electroluminescence in Organic Crystals", The Journal of Chemical Physics **38**, 2042 (1963).

[51]J. H. Burroughes, D. D. C. Bradley, a. R. Brown, R. N. Marks, K. Mackay, R. Friend, P. L. Burns, and a. B. Holmes, "Light-emitting diodes based on conjugated polymers", Nature **347**, 539 (1990).

[52]J. Shinar and V. Savvateev, "Introduction to Organic Light-Emitting Devices", in *Organic light-emitting devices: a survey*, edited by J. Shinar, 1st ed. (Springer-Verlag New York, Inc., New York, 2004) Chap. 1, pp. 1–34.

[53]G. R. Strobl, *Conjugated Polymers*, 3rd ed. (Springer Berlin Heidelberg, Berlin, Heidelberg, 2007), pp. 287–301.

[54]C. D. Dimitrakopoulos and D. J. Mascaro, "Organic thin-film transistors: A review of recent advances", IBM Journal of Research and Development **45**, 11–27 (2001).

[55]R. M. Smith, B. Liu, J. Bai, and T. Wang, “Temperature dependence of non-radiative energy transfer in hybrid structures of InGaN/GaN nanorods and F8BT films”, Applied Physics Letters **105**, 171111 (2014).

[56]S. Guha, R. A. Haight, N. A. Bojarczuk, and D. W. Kisker, “Hybrid organic–inorganic semiconductor-based light-emitting diodes”, Journal of Applied Physics **82**, 4126 (1997).

[57]N. J. Findlay, J. Bruckbauer, A. R. Inigo, B. Breig, S. Arumugam, D. J. Wallis, R. W. Martin, and P. J. Skabara, “An organic down-converting material for white-light emission from hybrid LEDs.”, Advanced materials (Deerfield Beach, Fla.) **26**, 7290–7294 (2014).

[58]G. Heliotis, G. Itskos, R. Murray, M. D. Dawson, I. M. Watson, and D. D. C. Bradley, “Hybrid inorganic/organic semiconductor heterostructures with efficient non-radiative energy transfer”, Advanced Materials **18**, 334–338 (2006).

[59]M. a. Baldo, D. F. O’Brien, and S. R. Forrest, “Excitonic singlet-triplet ratio in a semiconducting organic thin film”, Physical Review B **60**, 14422–14428 (1999).

[60]M. Wohlgenannt, K. Tandon, S. Mazumdar, S. Ramasesha, and Z. V. Vardeny, “Formation cross-sections of singlet and triplet excitons in pi-conjugated polymers.”, Nature **409**, 494–497 (2001).

[61]P. W. Atkins and J. De Paula, *Atkins’ Physical Chemistry*, 8th ed. (Oxford University Press, Oxford, 2006).

[62]J. Huang, G. Li, E. Wu, Q. Xu, and Y. Yang, “Achieving high-efficiency polymer white-light-emitting devices”, Advanced Materials **18**, 114–117 (2006).

[63]T. Forster, “Energiewanderung und Fluoreszenz”, Naturwissenschaften **33**, 166–175 (1946).

[64]D. Basko, G. C. La Rocca, F. Bassani, and V. M. Agranovich, *Förster energy transfer from a semiconductor quantum well to an organic material overlayer*, 1999.

[65]C. R. Belton, G. Itskos, G. Heliotis, P. N. Stavrinou, P. G. Lagoudakis, J. Lupton, S. Pereira, E. Gu, C. Griffin, B. J. E. Guilhabert, I. M. Watson, A. R. Mackintosh, R. A. Pethrick, J. Feldmann, R. Murray, M. D. Dawson, and D. D. C. Bradley, “New light from hybrid inorganic–organic emitters”, Journal of Physics D: Applied Physics **41**, 94006 (2008).

[66]J. J. Rindermann, G. Pozina, B. Monemar, L. Hultman, H. Amano, and P. G. Lagoudakis, "Dependence of resonance energy transfer on exciton dimensionality", Physical Review Letters **107**, 1–5 (2011).

[67]H. Sahoo, "Förster resonance energy transfer - A spectroscopic nanoruler: Principle and applications", Journal of Photochemistry and Photobiology C: Photochemistry Reviews **12**, 20–30 (2011).

[68]X. Xu and H. Wang, "Resonant energy transfer between patterned InGaN/GaN quantum wells and CdSe/ZnS quantum dots", Nanoscale **8**, 342–347 (2016).

[69]S. Chichibu, "Exciton localization in InGaN quantum well devices", Journal of Vacuum Science & Technology B: Microelectronics and Nanometer Structures **16**, 2204 (1998).

[70]S. Chichibu, T. Azuhata, T. Sota, and S. Nakamura, "Spontaneous emission of localized excitons in InGaN single and multiquantum well structures", Applied Physics Letters **69**, 4188 (1996).

[71]M. Achermann, M. a. Petruska, S. Kos, D. L. Smith, D. D. Koleske, and V. I. Klimov, "Energy-transfer pumping of semiconductor nanocrystals using an epitaxial quantum well.", Nature **429**, 642–646 (2004).

Chapter 3

Experimental Techniques

3.1 Experimental Techniques

A number of experimental techniques are employed throughout this research project in semiconductor micron and sub-micron featured device fabrication and characterisation. It is important to understand in detail the function and operation of all such equipment; where optical, electrical and structural results can then be correlated back to their origin so that they might be replicated and/or improved.

In this study two separate as-grown sample structures are used respectively in chapters 4 to 6 and chapter 5, as detailed in section 8.2.

3.2 Device Fabrication

3.2.1 Photolithography

The principle of photolithography involves modulation of light to generate a desired pattern in light-sensitive photoresist material, subsequently used as a sacrificial layer that selectively resists stages of device formation. Photoresist reacts chemically to ultraviolet (UV) exposure to become more or less soluble in its counterpart developer solution, divided into a respective positive or negative tone polarity[1].

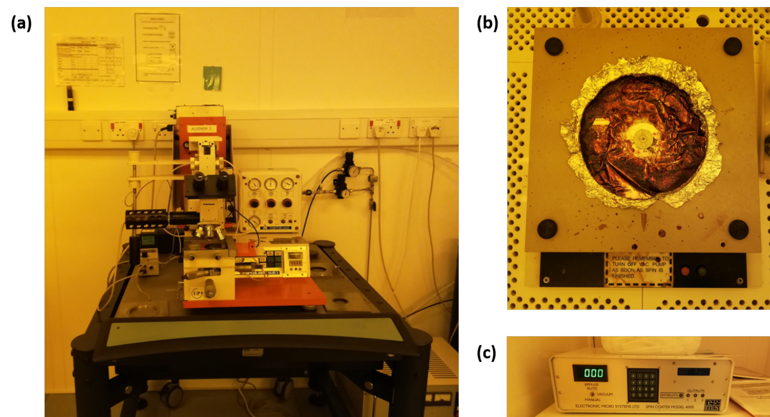

Figure 3.1: Image of (a) Karl Suss MJB3 mask-aligner, (b) Electronic Micro System Photoresist Spin Coater Model 4000 and (c) control unit.

A Karl Suss MJB3 mask-aligner, Figure 3.1a, allows the registration of successive fabrication level. This involves matching the position of the photomask overlaid on previously patterned structure and repeating the photolithographic transfer

process; vernier screws moving the sample in X, Y and θ_Z. Intimate contact between photoresist and photomask is made with an approximate 1 µm resolution before homogeneous exposure using mercury-arc lamp that moves into place of the microscope objectives[2]. Feature-sizes approaching the optical wavelength result in the effects of diffraction, where fluctuations in the finite photoresist thickness and light-scattering limit resolution. The minimum resolvable linewidth (W_{min}) of conventional proximity photolithography is defined from exposure wavelength (λ) and mask-substrate separation (Z) by equation (3.1)[3].

$$W_{min} = \sqrt{\lambda Z} \tag{3.1}$$

$\mathbf{W_{min}}$ = minimum resolvable linewidth

$\mathbf{Z}$ = mask-substrate separation

The photoresist composition consists of three principle parts that control mechanical properties and viscosity that include an adhesive resin, solvent and photosensitive polymer[2]. A photoresist is spin-coated to achieve a different thickness that each satisfies a unique fabrication requirement. An Electronic Micro System Photoresist Spin Coater Model 4000 is used with a rotational speed ranging between 150 - 9500 RPM, as shown in Figure 3.1b and 3.1c. The sample is held in position on a vacuum chuck inside polypropylene bowl before a static-dispensed photoresist is spun on-axis, where the applied centrifugal force result in a uniform coverage. The film thickness is then determined both by viscosity (η) and spin-speed (ω) proportional to $\frac{\eta}{\sqrt{(\omega)}}$[4,5].

3.2.2 Dry-Etching

Reactive-Ion Etching

The use of dry-etching techniques is required due to the high chemical stability of III-N materials, preventing standard wet-chemical etch methods, transferring a patterned image into the layer under photoresist. Reactive-ion etching (RIE) allows a combined plasma-assisted reactive chemical and physical ion-bombardment anisotropic etch process, where vertical and lateral etch-rate differ significantly to provide improving aspect ratio[6].

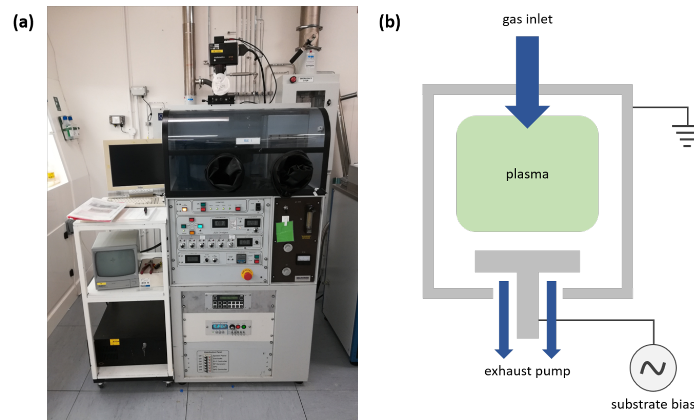

Figure 3.2: Image of (a) JLS Design Plasma Technology RIE system and (b) schematic diagram illustrating reactive-ion etching.

Sustained plasma is generated under vacuum with a single radio frequency (RF) generator applied across parallel electrode above the gas breakdown potential; electric-field oscillations and particle collisions ionising molecules. The charged particles of the partially ionised neutral gas are strongly influenced by an applied electric and/or magnetic field, which are then accelerated toward the isolated biased substrate platen gaining kinetic energy[2]. A JLS Design Plasma Technology RIE system has a parallel-plate configuration, where the reactor chamber walls act as the secondary large effective-area ground electrode, as demonstrated in Figure 3.2.

A number of chemistries are used in SiO_2 and Si_3N_4 dielectric (CHF_3, Ar and O_2) etching, which are broken-down to chemical reactive species in plasma. The flow-rates are controlled into the process chamber through gas inlet valves , determining in part the etch-rate requirements. High-energy ion of the RF induced reactant plasma diffuse to attack the sample surface through adsorbed chemical reaction and ion-bombardment, by-products are desorbed and extracted through a background vacuum exhaust system[1].

Inductively Coupled Plasma Reactive-Ion Etching

An Oxford Instruments Plasmalab System 100, shown in Figure 3.3a, is an inductively coupled plasma (ICP) reactive-ion etching instrument. ICP is a variation on the anisotropic RIE dry-etching process, removing surface atoms through the same combined plasma-assisted reactive chemical and physical surface interaction at increased rates[2]. An independent substrate and ICP RF generator is used to produce

high-density plasma, allowing the isolated control of both ion energy and density.

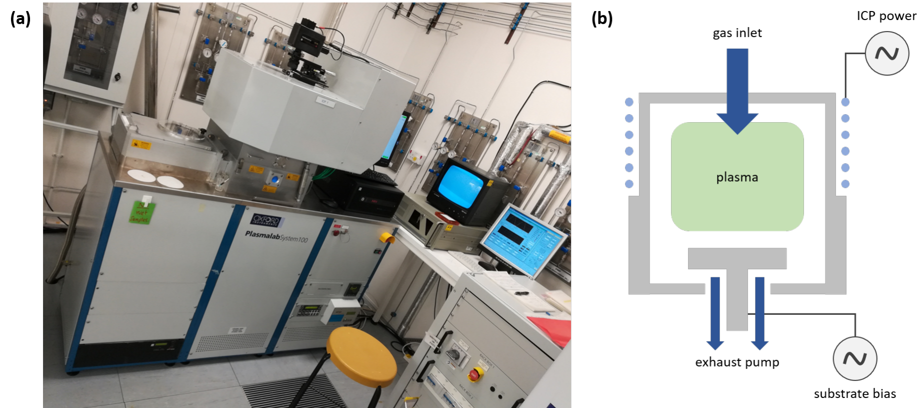

Figure 3.3: Image of (a) Oxford Instruments Plasmalab System 100 ICP-RIE system and (b) schematic diagram illustrating inductively coupled plasma reactive-ion etching.

Different chemistries are each used in SiO_2 (CHF_3 and Ar) and III-N ($SiCl_4$, Cl_2 and Ar) etching, which breakdown into chemical reactant species in the plasma[7].

Enhanced plasma density is achieved using an electromagnetic winding that surrounds the reactor chamber. The ICP generator then drives an RF current through this coil inducing an alternating magnetic-field within the plasma, as demonstrated in Figure 3.3b. This influences the perpendicular motion of the free-electrons that instead follow a helical path, effectively increasing their path length and opportunity for impact ionisation[1]. The higher ion mass however mean that they travel unperturbed through the magnetic-field oscillation[8].

The second RF generator is applied as in the RIE system to the decoupled lower electrode, increasing again kinetic energy through net acceleration of high-density ion toward the biased substrate platen. An increasing number of reactant charged particles diffuse and attack the surface as a result of the enhanced ion density, where neutral species are otherwise unaffected by the secondary RF substrate bias with fewer off-axis interactions.

3.2.3 Thin-Film Deposition

Plasma-Enhanced Chemical Vapour Deposition

A plasma-enhanced chemical vapour deposition (PECVD) involves formation of high-quality homogeneous dielectric thin-films through chemical reaction of gaseous compounds under vacuum.

Low-temperature depositions at around 300 °C are possible using plasma-enhanced processing with increasing reaction rate; conventional thermal chemical vapour deposition (CVD) instead requiring closer to 800 °C[1].

The precursor gas in a Plasma-Therm 790 series PECVD system is introduced into the reactor chamber between substrate and RF generator electrode through a shower-head inlet valve, as in Figure 3.4. Plasma is then initiated through a capacitive coupling across the parallel-plates, using mechanism similar to that of RIE, where a ground substrate platen instead minimises effects of ion-bombardment. Dielectric SiO_2 and Si_3N_4 thin-films are deposited using combination of precursor SiH_4 and N_2 gas with respective reactant oxygen (N_2O) or nitrogen (NH_3) source[1,9].

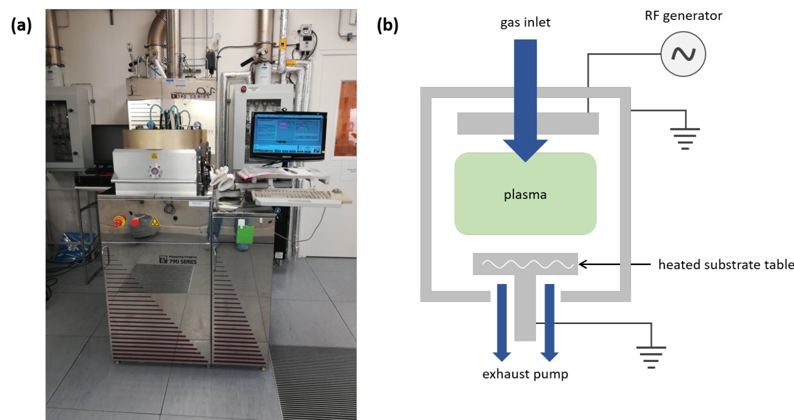

Figure 3.4: Image of (a) Plasma-Therm 790 series PECVD system and (b) schematic diagram illustrating plasma-enhanced chemical vapour deposition.

Products of the precursor reactant gas are adsorbed at the surface of the heated susceptor, elevated temperatures catalysing the decomposition of ionised compounds at the substrate surface forming epitaxial growth of the target material. A cold-wall (60 °C) process chamber has a non-uniform temperature distribution limiting unintended deposition outside of the substrate platen, minimising memory-effects. Chemical by-products ultimately desorb and diffuse into diluent carrier

gas away from surface before being extracted through a background vacuum exhaust system[2].

Thermal Physical Vapour Deposition

Thermal physical vapour deposition (PVD) using an Edwards Coating System 306A, as demonstrated in Figure 3.5, involves the resistive heating of a refractory-metal filament to vapourise loaded target material (Al, Au, Ni or Ti) in thin-film metal deposition under high-vacuum. A tungsten coil minimises out-gassing as a result of its significantly higher boiling point ($\sim$ 5930 °C)[10].

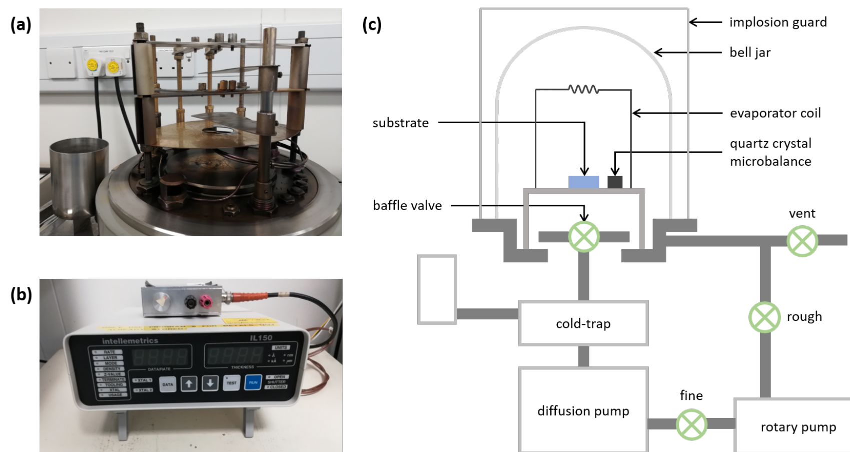

Figure 3.5: Image of (a) Edwards Coating System 306A, (b) Intellemetrics IL150 quartz crystal growth rate monitor and (c) schematic diagram illustrating thermal physical vapour deposition.

Low-pressure evaporation reduces significantly the disruption of vapour deposition, impurity concentration and heat transfer caused by the otherwise residual background gas. The combination of a rotary and diffusion pump is applied in sequence to reach high-vacuum (10^{-6} mBar), where a diffusion pump is unable to operate at atmospheric pressure above approximately 1 mBar. A cold-trap prevents the backstreaming of hot contaminant diffusion pump oil vapours into the process chamber, condensing instantaneously and extracting with it gas molecules within the sealed bell jar using a momentum transfer[1].

An external power supply is feedthrough to the low-pressure chamber with high-currents (20 - 40 A) controlled using a variable transformer between four isolated sources, permitting multi-layer deposition without breaking vacuum. Tem-

peratures above the boiling point mean the charge material transitions each through the solid, molten and gas phases. Evaporated atomic material inside the evacuated chamber then travel at high-velocity in omnidirectional straight line trajectories from the filament before condensing and freezing across the substrate to form a thin-film.

Film thicknesses are monitored in real-time using an in-situ Intellemetrics IL150 quartz crystal growth rate monitor, Figure 3.5b, which incorporates a crystal oscillator that is calibrated to detect change in resonant frequency from the resulting increasing mass. A mechanical shutter above the sample can then be used to obstruct evaporation and abruptly stop/start deposition.

Electron-Beam Physical Vapour Deposition

Electron-beam (e-beam) PVD is a process similar to that of the thermal evaporation technique described above in section 3.2.3, using an Edwards Auto306 Vacuum Coater with samples instead located at the top of the process chamber.

An electron-gun emits a high-energy 10 kV e-beam through thermionic emission, which is situated beneath the crucible mount that is otherwise outside the deposition line-of-sight. The e-beam is then steered magnetically 270° so as to come back into incidence with either ITO (indium tin oxide) or SiO_2 source material, different targets are contained within individual tungsten crucible that are mechanically rotated into position. A continuous rasterised sweeping across the surface directly energises the charge into its vapourised phase, which under low-pressure will then condense and freeze indiscriminately across the substrate to form a thin-film[2].

3.2.4 Anaerobic Glove-Box

Organic materials are highly-sensitive to degradation in the presence of atmospheric moisture and oxygen; photo-oxidation in particular results in a considerable permanent emission quenching facilitated by a radiant energy[11,12]. This means organic materials require processing in a COY Laboratories Anaerobic Glove-Box environment, Figure 3.6a and 3.6b, where O_2 content is monitored below 0.5 ppm using a COY model 10 gas analyser. A background pre-mixed forming gas atmosphere of $N_2 > 95$ % and $H_2 < 5$ % avoids degradation mechanics despite the high-stability of polyfluorene materials[13,14].

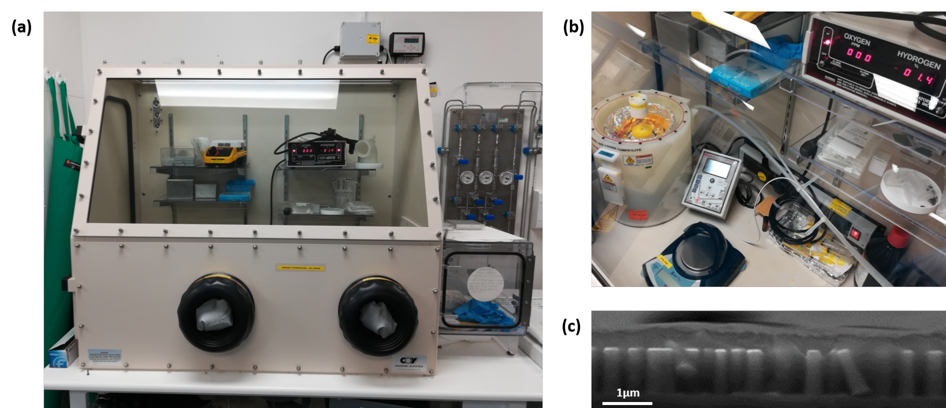

Figure 3.6: Image of (a) COY Laboratories Anaerobic Glove-Box, (b) main anaerobic process chamber interior and (c) self-assembled nanorod array cross-sectional SEM with spin-coated F8BT in 10 mg/mL toluene concentration[15].

A fan-box ensures an homogeneous anaerobic environment and temperature gradient throughout the glove-box, recirculating atmosphere through filters. The combination of deoxo-catalyst, desiccant and activated charcoal together extract respective ambient O_2, H_2O and solvent vapours within the process chamber; deficient hydrogen content is the usual cause for losing anaerobic condition. Palladium deoxo-catalyst exothermically reacts in the presence of both H_2 and O_2 to form H_2O, where oxygen constantly re-enters the chamber through airlock operation and diffusion. Hydroscopic aluminium desiccant then absorbs atmospheric H_2O in order to restrict ambient humidity levels, becoming less effective as pores saturate with water vapours. Activated charcoal with a highly-porous micro-capillary structure will indiscriminately adsorb vapour molecules across the large area-to-volume ratio, collecting molecules at the surface.

OLEPs are prepared as a solution in toluene and deposited with a drop-cast or spin-coating technique. This results in an approximate 90 nm film thickness using Laurell Technologies WS-650 Series Spin Processor at 4000 RPM, as shown in 3.6c, which is otherwise limited by low molecular weight and viscosity[4,5]. Organic materials are weighed using a 1 mg precision electronic laboratory balance to control the dilution concentration of solute in measured solvent volume.

3.3 Device Characterisation

3.3.1 Optical and Electrical Characterisation

Photoluminescence

Optical characterisation involves the instantaneous non-destructive and non-contact photoluminescence (PL) spectroscopy analysis of material properties that include band-gap, QCSE, crystalline defect and chemical composition.

PL includes a generation of excited electron-hole pair beyond the band-edge through light absorption, investigating the mechanics that act to restore excess minority carriers in the material to equilibrium[16]. A recombination of the free carrier back to the valence state occur through the different radiative and non-radiative action. The radiative transition of electron-hole pair across the band-gap (E_g) releasing change in equivalent energy as a photon, discussed in sections 2.1.6 and 2.1.7.

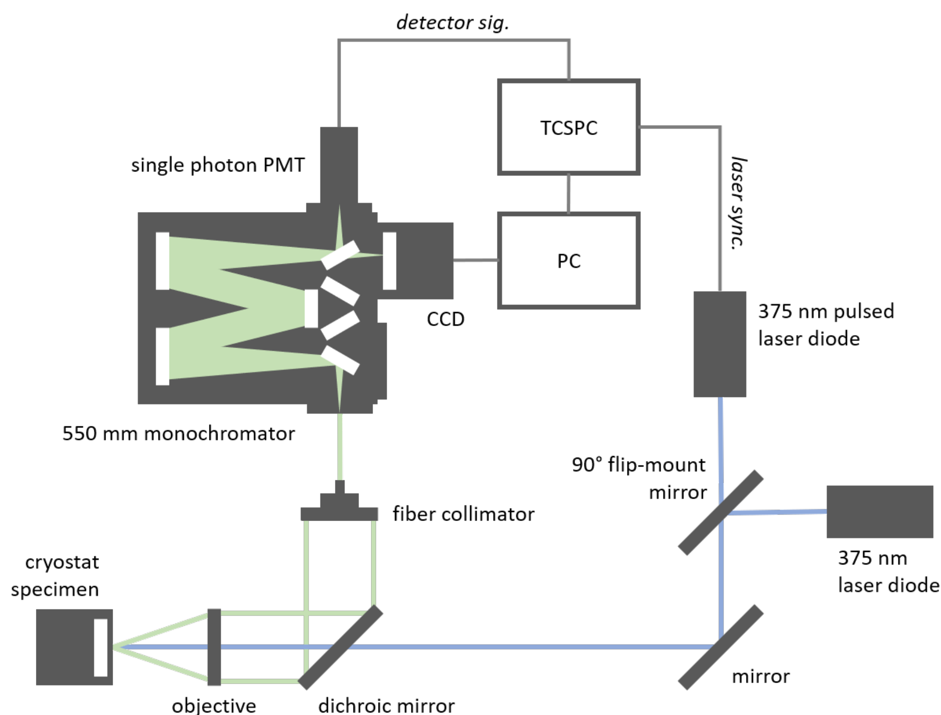

Figure 3.7: Image of schematic diagram illustrating photoluminescence and time-resolved photoluminescence optical characterisation system.

Specimen are mounted under high-vacuum ($\sim 10^{-6}$ mBar) in a continuous-

flow Janis ST-500 Microscopy Cryostat with temperature range between 77 and 300 K; room-temperature and oxygen-free measurements are performed to minimise photo-oxidation degradation of organic material in chapters 4 and 5.

Figure 3.7 shows a continuous wave (CW) Vortran Laser Technologies 375 nm Stradus laser diode used to excite exclusively the InGaN QW, necessitating a photon energy above the material band-gap. This allows investigation of the active regions optical properties in isolation as GaN is effectively transparent beyond 364 nm (3.4 eV). The laser beam is then directed in free-space to high-performance UV-enhanced 50x magnification objective with a 0.42 NA through dichroic mirror that is reflective below 412 nm, focussing to an estimated micron-scale spot-size. PL emission is collected in-plane with the same objective and dichroic mirror, which can now transmit the longer wavelength down-converted light. A 50:50 beam-splitter then provides an optical-path to both video camera and off-axis parabolic reflective collimator to 1 mm multi-mode optical-fiber.

Spectra are measured using a Horiba Jobin Yvon iHR550 spectrometer and Synapse thermoelectric cooled charged-coupled device (CCD) detector at -70 °C. The 550 mm focal length Czerny-Turner spectrometer consists of two aspheric mirrors and a three grating turret; collimating first to the diffraction grating and then focusing dispersed monochromatic light to the CCD for spectral acquisition.

A linear polariser in a continuous 360° rotation mount is positioned before the optical-fiber coupling in polarisation dependent measurement as in chapter 5, correcting the system polarisation with normalisation over the emission spectra of a halogen calibration lamp.

Time-Resolved Photoluminescence

Time-resolved photoluminescence (TRPL) investigates the recombination dynamics of free carriers, measuring PL intensity as a function of time[16]. The recombination rate is controlled by carrier lifetime, defined as the mean time between generation and recombination of minority carriers from equation (2.12).

PL and TRPL share the same system to allow simultaneous optical measurements in both the spatial and temporal domain at identical points, separated only by a 90° flip-mount mirror as shown in Figure 3.7.

The TRPL configuration instead uses a pulsed PicoQuant PDL 800-B 375 nm laser diode with 50 ps pulse-width over a 2.5 – 40 MHz frequency range, incorporating a synchronisation output to trigger time-correlated single photon counting

(TCSPC) electronics. Additionally, dispersed monochromatic light of the Horiba Jobin Yvon iHR550 spectrometer is focused rather to a Becker & Hickl HPM-100-40 with a Hamamatsu R10467 GaAsP hybrid photomultiplier tube (PMT) detector. A hybrid PMT releases an electron that is accelerated at high-voltage within a vacuum-tube when incident photon interact with the GaAsP photocathode, high-energy electron then strike the silicon avalanche photodiode (APD) to generate a measurable current at the anode[17]. This high-gain enables individual photon detection under low-light conditions with a single photon response time down to 120 ps. The overall system has an approximate 15 ps timing resolution and instrument response function (IRF) around 150 ps, which is the convoluted system timing-artefact applied in each measurement.

The pulsed laser diode and hybrid PMT detector both directly interface with Becker & Hickl Simple-Tau 130 TCSPC electronics, recording individual free-carrier excitation and relaxation event.

TCSPC in a reverse start-stop mode correlates the time between detection of the first single photon and next excitation pulse using a time-to-amplitude converter (TAC)[16], which when triggered by the hybrid PMT will start capacitor charging. The following synchronised laser diode pulse stops the charging and an analogue-to-digital converter (ADC) provides a time since excitation from the measured voltage[17]. This is repeated until statistically large number of single photon events have been registered, compiling a histogram decay profile matching the real-time intensity distribution with a deviation from equilibrium. The probability of a relaxation event decreasing with time since pulsed excitation.

A TCSPC system allows simplification over single pulse measurements, using slower components to measure significantly faster mechanics. The only requirement is that the chance for multiple photon detection between consecutive excitation pulses is made negligible, avoiding unintentional bias to earlier photon. This can be realised by controlling the single photon detection below approximately 1:20 of the laser repetition rate[17].

Confocal Photoluminescence

A high-resolution WITec Alpha300 confocal PL spectral imaging microscopy system, shown in Figure 3.8a, uses a single-point excitation and collection that is focused to a 10 μm pinhole, rejecting light outside the image-plane. This improves the imaging contrast and lateral confocal resolution.

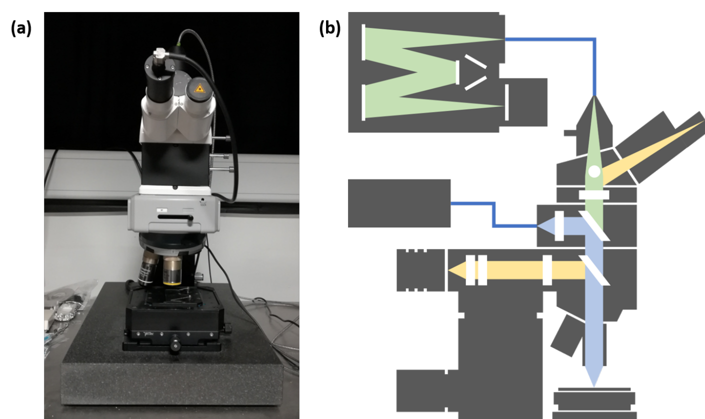

Figure 3.8: Image of (a) WITec Alpha300 and (b) simplified schematic diagram illustrating confocal spectral imaging microscopy system.

Specimen can be considered the superposition of infinite point-like objects with dimensions below the optical systems resolution. Confocal PL mapping produces a point-like 0D to 3D spectral array, where elements are complete spectra measured at each scan position. Fluctuations in the PL intensity map distribution then correspond to the sample's structure and/or material composition.

The sample position is controlled in relation to a focused laser beam in the microscope optical axis, where a stationary diffraction-limited spot is much easier to maintain. A sub-nanometre precision 3-axis piezoelectric flexure scan-stage is used with a lateral 100 x 100 µm and axial 20 µm range, which ultimately determines maximum image sizes. The scan-stage is then mounted above an additional coarse alignment 20 mm XY dovetail translation stage.

Figure 3.8b identifies the different instrument beam path and measurement modes that include bright-field optical microscopy (yellow), reflected confocal fluorescence spectral imaging (green) and 375 nm laser excitation (blue); sharing an optical axis in the vertical direction.

A Vortran Laser Technologies 375 nm Stradus laser diode source is coupled externally to a single-mode optical-fiber. The laser beam is directed to the sample-plane using a holographic beam-splitter, which subsequently transmits PL and reflected bright-field illumination between either pinhole or ocular colour eye-piece video camera. A 100x magnification objective with 0.95 NA and 310 µm working distance is used to both focus excitation and collect emitted light along the same axis, giving high-performance confocality and spatial resolution. The spectra

are then acquired using a Princeton Instruments SprectraPro 300i Czerny-Turner spectrometer and Andor Newton DU970N-UVB-353 back-illuminated CCD, thermoelectrically cooled to -60 °C minimising dark current. The input aperture is an SMA multi-mode optical-fiber that also forms the 10 μm pinhole.

Along the propagation axis a transverse laser beam profile remains Gaussian. The objective focuses collimated light to the beam-waist of an hyperboloid in the Z-axis, setting a principal limit to the optical system's resolution. Image scan parameters are restricted below the number of resolvable point-like measurements in each dimension, providing necessary distinction between adjacent spectral points. This limit is defined by the Rayleigh criterion ($0.61\frac{\lambda}{NA}$) from the excitation wavelength and objective properties, where a diffraction-limited beam-waist is given to an approximate 240 nm[18].

The microscopy system is used in a combined high-resolution confocal spectral imaging and direct-write laser photolithography single-instrument, described in chapter 6.

Electroluminescence

Electroluminescence (EL) is the generation of light through radiative electron-hole recombination that results from an applied electric-field.

The forward-bias of a PN-junction diode above the built-in electrostatic potential allows current to flow and efficient injection of majority carrier into the active region; n-type and p-type material providing a respective high-concentration of electrons and holes. A localised quantum-confinement of the electron-hole pair improves the respective carrier wavefunction overlap, enhancing probability of relaxation to the ground-state as required through EL.

A digital microscope is mounted above the samples, which includes a XIMEA xiQ global-shutter CMOS colour video camera with an infinity corrected objective and 12x UltraZoom Navitar lens tube. A probe-station is then used to mechanically contact the electrodes to both apply and/or acquire an electrical signal using a Keithley 2400 SourceMeter, analysing optoelectronic properties at ambient condition. High-precision micromanipulator locate the 600 nm passive tungsten probe-tips to the anode and cathode.

Emitted light is collected using a high-performance 50x magnification objective with 0.42 NA and 20.5 mm long working distance, as demonstrated in Figure 3.9. A sufficient 1.6 μm depth-of-focus and field-of-view ensure that an entire 100

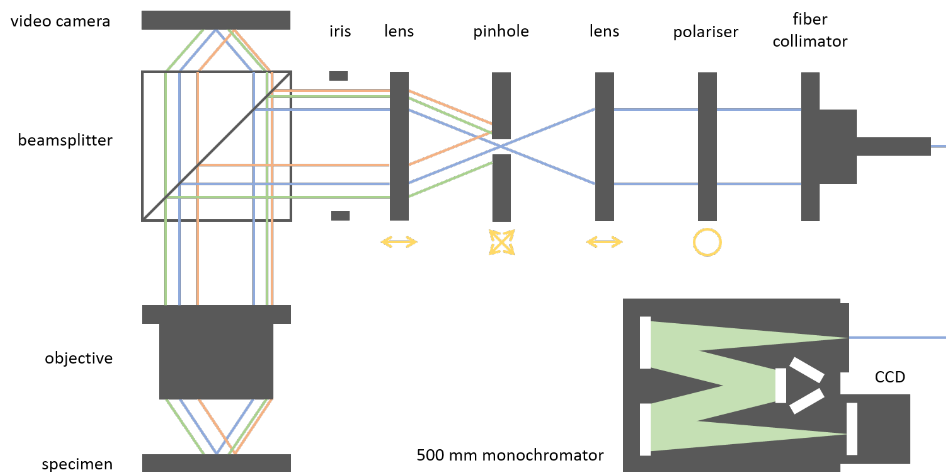

Figure 3.9: Image of schematic diagram illustrating electroluminescence optoelectronic characterisation system.

x 100 µm emission area is observed. Infinity corrected light is then directed and focused to an off-axis parabolic reflective optical-fiber collimator through 50:50 beam-splitter. Spectra are then detected using an Andor Newton CCD and Shamrock 500i Czerny-Turner monochromator with a 500 mm focal length; 400 µm diameter multi-mode fiber-optic probe with 0.22 NA coupled to StellarNet EPP2000-HR spectrometer is used alternatively in chapter 4.

Additional optical components can be included and changed along the collimated perpendicular beam path: lever-actuated continuous iris diaphragm controls effective NA; 10 µm pinhole and paired Hastings triplet achromatic lens reject light outside the focal-plane; and a continuous 360° rotating linear polariser allows polarisation dependent measurements as in chapter 5.

A Standa motorised XY scan-stage with 75 x 75 mm travel is used to align the devices in the optical-axis. The microscope is then mounted to a combined Standa motorised 360° continuous rotation and 100 mm linear Z focusing translation stage.

3.3.2 Scanning Electron Microscopy

A Raith EO field-emission scanning electron microscope (FE-SEM) is used in high-magnification imaging between 10 - 10^5 times in morphological characterisation.

The field-emission gun emits high-energy electron under vacuum with volt-

age ranging 0.1 and 30 kV, low-pressure operation minimises electron collisions on the beam path. A combination of magnetic condensers and objective lens focus the electron-beam to a smallest diameter spot-size in highest-resolution nanoscale imaging[19]. Images are then generated as the focused electron-beam is raster-scanned across three-dimensional topology, where position is controlled over a fixed area using pairs of scanning coils in the final magnetic lens that deflect the electron-beam in X and Y directions[20].

Atomic interactions at the surface produce detectable secondary electron and/or back-scattered electron, converted to an electrical signal that are reconstituted in to two-dimensional images from the variations in measured intensity distribution. Electrons lose and transfer energy through a continuous elastic and inelastic scattering within a shallow droplet interaction volume, producing the reflected primary and emitted secondary electron. The secondary electron produce a highest-resolution geometric imaging, where a back-scattered detector provides increased contrast between atomic material compositions[20]. An insulating sample without path to electrical-ground will however accumulate electrostatic charge across the surface from the primary electron-beam, resulting in potential image degradation and scanning faults.

3.4 References

[1]S. A. Campbell, *The Science and Engineering of Microelectronic Fabrication*, 2nd ed. (Oxford University Press, Oxford, 2001), pp. 1–624.

[2]G. S. May and S. M. Sze, *Fundamentals of Semiconductor Fabrication*, 1st ed. (John Wiley & Sons, Inc., New York, 2003), pp. 1–320.

[3]J. J. Toriz-Garcia, G. L. Williams, R. McWilliam, R. Curry, N. L. Seed, A. Purvis, and P. A. Ivey, "Controlled-width track in through silicon via using 3D holographic photolithography with modified electrodepositable photoresist", Journal of Micromechanics and Microengineering **20**, 015012 (2010).

[4]A. G. Emslie, F. T. Bonner, and L. G. Peck, "Flow of a Viscous Liquid on a Rotating Disk", Journal of Applied Physics **29**, 858–862 (1958).

[5]H. J. Levinson, *Principles of Lithography*, 3rd ed. (SPIE Press, Washington, 2011), pp. 1–32.

[6]T. M. Mayer, R. A. Barker, and L. J. Whitman, "Investigation of plasma etching mechanisms using beams of reactive gas ions", Journal of Vacuum Science and Technology **18**, 349–352 (1981).

[7]R. Cheung, B. Rong, E. van der Drift, and W. G. Sloof, "Etch mechanism and etch-induced effects in the inductively coupled plasma etching of GaN", Journal of Vacuum Science & Technology B: Microelectronics and Nanometer Structures **21**, 1268 (2003).

[8]T. Okumura, "Inductively Coupled Plasma Sources and Applications", Physics Research International **2010**, 1–14 (2010).

[9]S. W. King, "Plasma enhanced atomic layer deposition of SiN x :H and SiO 2", Journal of Vacuum Science & Technology A: Vacuum, Surfaces, and Films **29**, 041501 (2011).

[10]Y. Zhang, J. R. G. Evans, and S. Yang, "Corrected Values for Boiling Points and Enthalpies of Vaporization of Elements in Handbooks", Journal of Chemical & Engineering Data **56**, 328–337 (2011).

[11]J. S. Lewis and M. S. Weaver, "Thin-film permeation-barrier technology for flexible organic light-emitting devices", IEEE Journal on Selected Topics in Quantum Electronics **10**, 45–57 (2004).

[12]J. Shinar and V. Savvateev, "Introduction to Organic Light-Emitting Devices", in *Organic light-emitting devices: a survey*, edited by J. Shinar, 1st ed. (Springer-Verlag New York, Inc., New York, 2004) Chap. 1, pp. 1–34.

[13]P. Lane, "Polyfluorene Electroluminescence", in *Organic light-emitting devices: a survey*, edited by J. Shinar, 1st ed. (Springer-Verlag New York, Inc., New York, 2004) Chap. 10, pp. 265–299.

[14]Y.-Y. Lin, Y.-N. Chang, M.-H. Tseng, C.-C. Wang, and F.-Y. Tsai, "Air-Stable flexible organic light-emitting diodes enabled by atomic layer deposition", Nanotechnology **26**, 24005 (2015).

[15]R. M. Smith, M. Athanasiou, J. Bai, B. Liu, and T. Wang, "Enhanced non-radiative energy transfer in hybrid III-nitride structures", Applied Physics Letters **107**, 121108 (2015).

[16]J. R. Lakowicz, *Principles of Fluorescence Spectroscopy*, 3rd ed. (Springer US, Boston, MA, 2006), pp. 1–954.

[17]W. Becker, *The bh TCSPC Handbook*, 7th ed. (Becker & Hickl GmbH, Berlin, 2017), pp. 1–891.

[18]WITec GmbH, *Application Note: Raman, PL & AFM measurements on lithographically created structures*, 2009.

[19]K. C. A. Smith and C. W. Oatley, "The scanning electron microscope and its fields of application", British Journal of Applied Physics **6**, 391–399 (1955).

[20]R. Egerton, *Physical Principles of Electron Microscopy: An Introduction to TEM, SEM, and AEM*, 1st ed. (Springer, Edmonton, 2005), pp. 1–202.

Chapter 4

Electrically Injected Hybrid Organic/Inorganic White Light-Emitting Diode with Non-Radiative Förster Resonance Energy Transfer

Reproduced (in part) with permission from ACS Photonics 2018, 5, 642647.
Copyright © 2017 American Chemical Society.

An electrically injected hybrid organic/inorganic white light-emitting diode (LED) is presented with a two-dimensional (2D) micro-hole array structure fabricated through the blue emitting InGaN/GaN multi-quantum well (MQW) of a high-performance inorganic device. The LED geometry improves proximity between the inorganic active region and down-converting organic light-emitting polymer (OLEP), enabling the highly-efficient near-field Förster resonance energy transfer (FRET) process whilst retaining excellent electrical characteristics of an unpatterned planar LED. A reduction in the average recombination lifetime in the InGaN/GaN MQW is measured with organic/inorganic hybridisation, providing confirmation of FRET. This results in a highest FRET efficiency of 16.7 %, where the FRET interaction area accounts for approximately 0.64 % of the remaining blue emitting inorganic LED, enhancing total device efficiency. An optimised white light electroluminescence (EL) emission is demonstrated with typical CIE colour co-ordinates at (0.29, 0.32).

4.1 Introduction

Analogous to the technological development of conventional telephones to the smartphone, lighting is expected to experience a similar evolution leading towards "smart-lighting" that is utilised simultaneously in general illumination and ultra-fast high-bandwidth visible light communication (VLC, i.e. Li-Fi). In such a case a white light source of certain characteristics is first needed to meet this multi-function requirement.

The past two-decades have seen a tremendous progress in the advancement of solid-state lighting, based primarily on III-nitride semiconductor materials. The current state-of-the-art remains founded on the well-established "blue LED + yellow phosphor" approach, dependent on blue emission from InGaN/GaN LEDs to radiatively pump down-conversion phosphor materials that provide longer wavelength yellow emission to generate together white light. This approach has several drawbacks, which includes self-absorption of the down-converting phosphor, limiting the colour-conversion efficiency from blue to yellow wavelengths and therefore colour-rendering.

However, the fundamental limitation of such an LED in Li-Fi applications is the intrinsically slow response time of phosphor materials, typically on the order of microseconds, restricting the potential bandwidth to below 1 MHz[1]. A receiver

instead would typically use blue filters to remove the slow-response of the phosphors' yellow light[2], resulting in a significant loss ($\sim$ 50 %) to signal intensity.

OLEPs have seen rapid development in recent years, resulting from several key advantages, including high luminescence efficiencies, solubility, low-cost manufacturing and flexibility. In addition the much faster response times of organic materials, in comparison to existing phosphors, offers particular advantages in ultra-fast Li-Fi[3]. OLEPs also however suffer from a number of fundamental problems, in particular poor electrical properties. A hybrid organic/inorganic III-nitride white LED therefore combines the complimentary advantages of the two major semiconductor material groups. The basic arrangement achieving white light emission involves the partial down-conversion of an electrically injected blue InGaN/GaN LED by yellow OLEP. A resulting hybrid device therefore features the respective high-performance electrical properties and photoluminescent (PL) quantum yield of the inorganic and organic material systems, as well as the ultra-fast response of the latter[4], potentially demonstrating superior performance to a standard white LED.

The issues of self-absorption are also eliminated by using OLEPs because of their intrinsically large Stokes-shift (> 100 nm)[5]. However, unlike existing phosphors, which are prepared in grains typically tens of micrometre in size, OLEPs can be dissolved in solvent. This allows the possibility to obtain homogenous microstructures using standard spin-coating techniques, used extensively throughout semiconductor optoelectronics. OLEPs can therefore simplify the process of fabricating white LEDs, which is particularly attractive to industry.

The most significant benefit to phosphor-free down-converting materials is the prospect and utilisation of the highly-efficient non-radiative Förster resonance energy transfer (FRET) process, enhancing colour-conversion efficiency[5–15]. FRET involves the near-field radiation-less energy transfer from the inorganic active region (donor) to OLEP (acceptor), through dipole-dipole Coulombic interactions[14]. The organic down-conversion material then emits radiatively at a rate above FRET, effectively stopping a reverse transfer process[12]. This avoids intermediate steps preceding the PL of the down-converting material, which before absorption includes the photon emission and then extraction in the LED. The energy transfer process consequently generates a change in carrier recombination dynamics, resulting in an enhancement in total device efficiency, where the FRET rate is sufficient to suppress non-radiative recombination in the inorganic LED[5].

The FRET rate is however strongly dependent on proximity between the donor and acceptor dipole, where a dipole-dipole separation of only a few nanometre (< 10 nm) is necessary to achieve an efficient FRET process[5–10]. This separation is described such that statistically FRET occurs before the donor exciton recombines and relaxes to its ground state[16]. The structure of the inorganic LED is therefore of significant importance to the demonstration of FRET.

Previous attempts to employ FRET have utilised a single-quantum well structure with a thin GaN cap layer of only several nanometres[6–14]. This form of structure cannot be fabricated into an electrically injected white LED due to the requirement of a thin (< 15 nm) cap layer, while a standard InGaN/GaN MQW blue LED would typically require an approximate 200 nm p-GaN cap layer. An electrically injected hybrid organic/inorganic white LED of this form has been demonstrated previously[17], where the deposition of an OLEP above the standard blue LED replaces a yellow phosphor without introducing the non-radiative FRET process[18,19].

This investigation reports the fabrication of a 2D micro-hole array structure through the InGaN/GaN MQW of a standard blue LED, producing for the first time an electrically injected hybrid organic/inorganic white LED compatible with the near-field requirements of FRET. The LED geometry increases proximity between the inorganic active region and down-converting OLEP, enabling the highly-efficient non-radiative FRET process whilst retaining excellent electrical characteristics.

A reduction in the carrier recombination lifetime in the InGaN/GaN MQW has been observed with organic/inorganic hybridisation, demonstrating a FRET efficiency of 16.7 %. This where the FRET interaction area accounts for approximately only 0.64 % of the remaining blue emitting inorganic LED, enhancing total device efficiency.

4.2 Method

4.2.1 Fabrication

The geometric configuration of this hybrid white LED aims to minimise separation between donor and acceptor dipoles using a top-down fabrication of a 2D micro-hole array structure within a standard planar LED device. A yellow down-converting OLEP is used to fill the volume of the 2D array of micro-holes, allowing

adjacent coupling with the exposed InGaN/GaN MQW side-walls. As a consequence to this structure, an inherently continuous p-GaN layer is also maintained, ensuring the electrical properties of the unpatterned device. Figure 4.1 depicts a schematic of the hybrid organic/inorganic LED with a 2D micro-hole array structure.

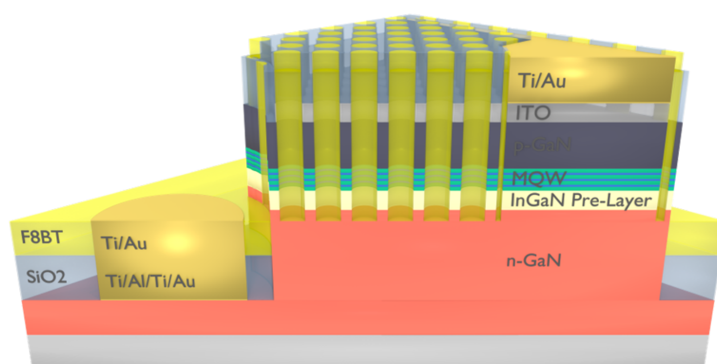

Figure 4.1: Schematic diagram of the hybrid organic/inorganic white LED with a 2D micro-hole array structure.

Planar LEDs with a standard 350 × 350 μm size are initially fabricated here from commercial blue InGaN/GaN LED wafer grown on c-plane sapphire. The structure consists: 1 μm n-GaN layer with a thick un-doped GaN buffer on a standard thin low-temperature GaN nucleation layer; 100 nm InGaN pre-layer; 160 nm InGaN/GaN MQW active region; and final 230 nm p-GaN layer.

Figure 4.2a shows a schematic diagram of the complete fabrication process (I-VIII) producing the micro-hole array structured hybrid organic/inorganic white LED. Standard planar LED fabrication (I) briefly involves an initial mesa etch, meaning part of the wafer is selectively etched into the n-GaN region for the later fabrication of isolated devices. A 100 nm ITO (indium tin oxide) layer is then deposited across the remaining p-type regions, forming an Ohmic contact after thermally annealing at 600 °C for 60 seconds in air. The n-contact electrode consists of Ti/Al/Ti/Au (20/100/20/60 nm), and then finally Ti/Au (20/200 nm) bond-pads are deposited on both the p-type and n-type contacts.

A 2D micro-hole array structure is then fabricated through the active region using a combination of standard photolithography techniques and selective dry-etching process. The exposed active region along the micro-hole circumference ensures minimal separation between donor and acceptor dipole, where the FRET

interaction volume becomes the outer radius of the remaining InGaN/GaN MQW structure[5]. This significantly enhances the coupling between adjacent donor (InGaN/GaN MQW) and acceptor (OLEP) dipoles. The micron-scale used is a close fundamental limitation to conventional photolithography, where minimum resolvable linewidth is dependent on exposure wavelength and mask-substrate separation[9].

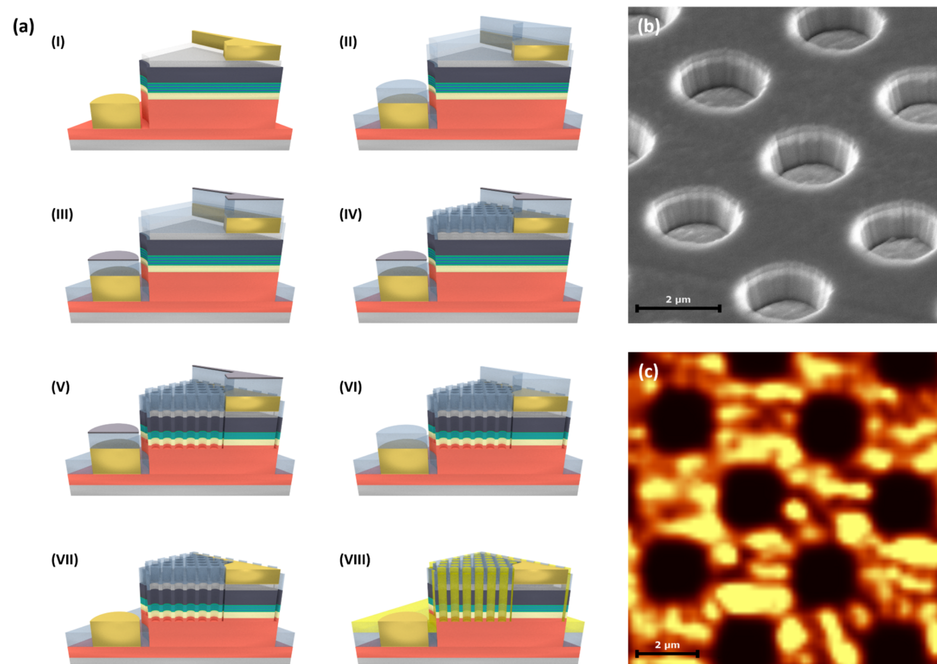

Figure 4.2: (a) Schematic diagram of the micro-hole array structured hybrid organic/inorganic white LED fabrication process (I-VIII), (b) SEM image (45° angle) and (c) confocal PL map under 375 nm laser excitation of the 2D micro-hole array structured blue LED after etching InGaN/GaN MQW.

The top-down process used for the fabrication of 2D micro-hole array begins with (II) a 250 nm SiO_2 layer deposited across the fabricated planar LED using plasma-enhanced chemical vapor deposition (PECVD), before (III) 20 nm Ni is then selectively evaporated above the n-type and p-type electrodes to prevent etching in subsequent steps. A thin photoresist film is then patterned with an array of circles packed in a polka-dot sequence, with a 2.5 µm diameter and a centre-to-centre spacing 3.5 µm minimum. This precedes (IV) the transfer of this pattern to

the SiO_2 layer using a standard CHF_3/Ar reactive-ion etch (RIE) process, which then acts as a secondary mask in further fabrication steps to overcome issues of etch-rate selectivity. The patterned 2D micro-hole array is then (V) formed in the planar LED, through the active region, using Cl_2/Ar inductively coupled plasma (ICP) etching via the 100 nm ITO current spreading layer (CSL). The undamaged n-type and p-type electrodes are then (VI-VII) re-exposed using the same selective SiO_2 RIE processing, previously concealed by the 20 nm Ni that is first removed using a NHO_3 wet-etch.

Figure 4.2b shows a scanning electron microscope (SEM) image taken at a 45° angle, confirming a 2.5 μm diameter hole with a 900 nm depth that is sufficient to completely expose the active region side-walls, while also demonstrating the continuity of the top p-contact. An etch depth of just 390 nm is adequate to pass the InGaN/GaN MQW of the as-grown LED wafer, where the measured 900 nm depth also includes the 250 nm SiO_2 layer and 100 nm ITO layer.

Figure 4.2c provides a high spatial resolution confocal PL map of the InGaN/GaN MQW emission under a 375 nm laser diode excitation, exhibiting the same periodic pattern in PL intensity as the corresponding 2D micro-hole array. The complete absence of PL emission from within the micro-hole regions acts to verify the complete exposure of the active region side-walls as is necessary to create a FRET interaction volume. The dark area trenches shown between some micro-holes are a variation in intensity, which is widely accepted in III-nitride materials to be related to an inhomogeneity in QW composition and thickness[20–23].

A prerequisite of FRET is the significant spectral overlap between the donor emission and the acceptor absorption energy to attain exciton coupling[5]. The π-conjugated yellow emitting polyfluorene co-polymer F8BT, Poly[(9,9-dioctylfluorenyl-2,7-diyl)-alt-co-(1,4-benzo-2,1',3-thiadiazole)], has pronounced absorption peaks at 320 and 455 nm with a high fluorescent quantum yield and relative ambient stability[24], confirmed by previous absorption spectral measurements[5]. In addition F8BT emits a broad yellow peak between 500 and 650 nm, displaying an overall yellow appearance, meaning it is ideally suited in the application of hybrid white LEDs demonstrating FRET colour-conversion. The top-down fabrication process is thus completed with (VIII) the deposition of F8BT to fill the volume of the micro-holes. Organic materials however are highly susceptible to degradation in the presence of atmospheric moisture and oxygen, resulting in permanent emission quenching[25]. To mitigate this organic material processing is completed

within an anaerobic ($O_2 < 0.5$ ppm) glove-box environment with hydrogen gas (H_2) < 5 % in nitrogen (N_2).

4.3 Results and Discussion

4.3.1 Electroluminescence

To make accurate comparison, an electrically injected LED with an unpatterned planar structure is fabricated and full characterisation measurements are then conducted. This same device then undergoes the top-down 2D micro-hole array fabrication process, explained above; full characterisation measurements are then repeated. The 2D micro-hole array structured LED is then completed with deposition of F8BT, filling the micro-hole array cavity, forming the hybrid organic/inorganic device, before full characterisation measurements are then completed once again.

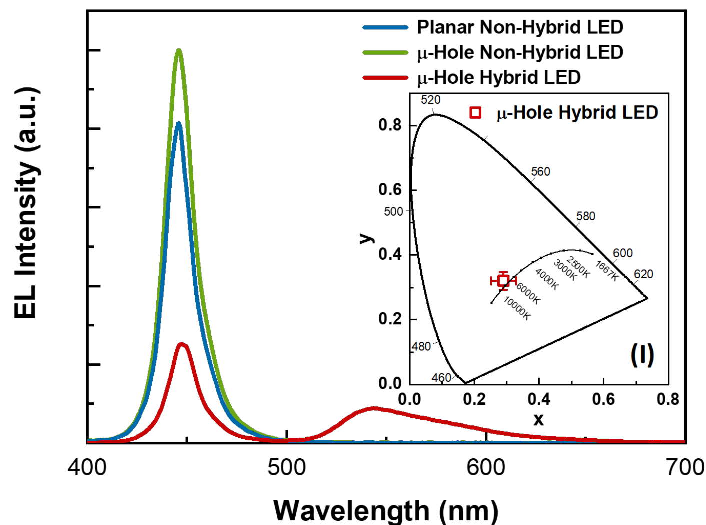

Figure 4.3: Room-temperature EL spectrum of the unpatterned planar blue LED, micro-hole array structured blue LED and hybrid organic/inorganic white LED measured at respective 20 mA injection current. Inset (I) CIE 1931 chromaticity diagram with co-ordinates at (0.29, 0.32) of the hybrid organic/inorganic white LED emission measured at 2 mA injection current.

Figure 4.3 presents the unaltered EL spectrum of the same blue LED, before and after the top-down 2D micro-hole array fabrication process (without F8BT)

under a 20 mA injection current. A slight improvement in EL intensity is seen after fabrication of the 2D micro-hole array, which may relate to an increased light extraction efficiency (LEE) resulting from the existence of the micro-hole array[26]. Figure 4.3 also includes the typical EL spectrum of the hybrid organic/inorganic white LED also measured under a 20 mA injection current, again no data manipulation is applied. A peak blue emission at 450 nm and yellow emission centred at 550 nm is demonstrated, with a 65 % difference in peak emission intensity, shown also as an optical image inset in Figure 4.4.

Chromaticity is then quantified using standardised Commission Internationale de l'Eclairage (CIE) calculations. A dichromatic colour mixing allows generation of all CIE 1931 chromaticity co-ordinates between the two individual points through change in dominant emission[27], where the blue InGaN/GaN LED and the F8BT polymer have respective (0.15, 0.04) and (0.42, 0.57) co-ordinates on the colour-space diagram[28]. The inset of Figure 4.3 shows the typical CIE colour co-ordinates of (0.29 $\pm$0.039, 0.32 $\pm$0.027) and the 8,336 K correlated colour temperature of the hybrid organic/inorganic white LED measured at a 2 mA injection current, corresponding to a colour-rendering index (CRI) of 52. This is achieved when the yellow emitting F8BT polymer is drop-cast in a 5 mg/mL toluene concentrated solution, allowing this to naturally fill the micro-hole volume, improving the contribution of F8BT emission to the EL spectrum significantly. However, in order to further improve CCT and CRI additional optimisation is still required. This might involve increasing deposited F8BT thickness and concentration in toluene or decreasing the remaining blue emission area by increasing the micro-hole density, which would also have the effect of increasing the FRET interaction area.

Figure 4.4 shows the IV characteristics of the unpatterned planar blue LED and micro-hole array structured blue LED. The electrical properties between the two inorganic blue LEDs remain relatively unchanged, exhibiting only a small 90 mV increase in turn-on voltage (V_o) from 3.46 V after the top-down 2D micro-hole array fabrication (without F8BT), in addition to a 2.68 Ω increase in series resistance from 10.27 Ω. Figure 4.4 also includes the IV characteristics of the hybrid organic/inorganic white LED, demonstrating no discernible change in electrical properties after F8BT deposition on the micro-hole array structured blue LED, exhibiting an identical 3.55 V turn-on voltage and almost identical effects of series resistance with only a small further 930 mΩ increase[29].

An increase in parasitic parallel resistance is observed at low and reverse volt-

age, indicating the introduction of additional shunting paths across the micro-hole side-walls, with higher reverse leakage current than in the planar LED device. This effect increases further with organic/inorganic hybridisation, where the organic semiconductor presents a short-circuit condition across the PN-junction with a slight micro-hole over-etch into the n-GaN layer.

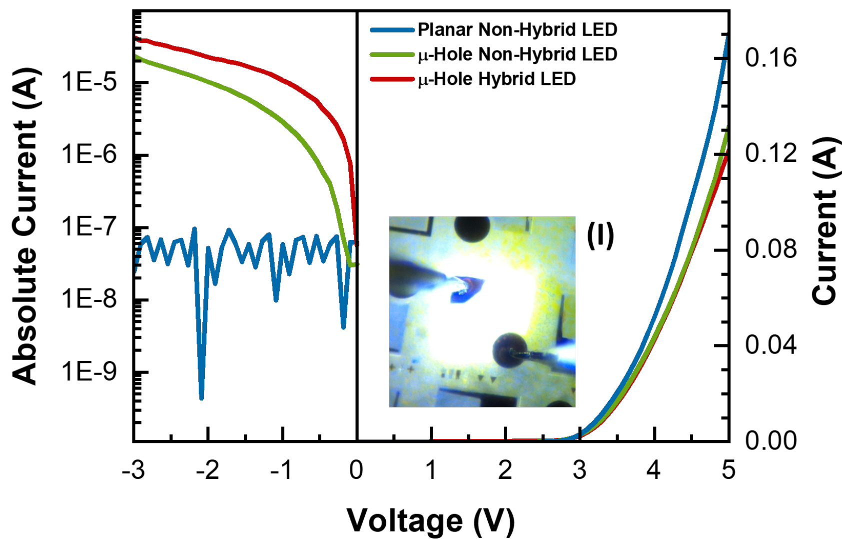

Figure 4.4: Room-temperature IV characteristics of the unpatterned planar blue LED, micro-hole array structured blue LED and hybrid organic/inorganic white LED with reverse-bias on semi-log scale. Inset (I) optical image of the hybrid organic/inorganic white LED emission measured at 20 mA injection current.

4.3.2 Photoluminescence and Time-Resolved Photoluminescence

Figure 4.5 shows the room-temperature PL spectrum of the micro-hole array structured blue LED and hybrid organic/inorganic LED measured using a 375 nm laser-diode excitation source. The micro-hole array structured blue LED shows strong PL emission at the 420 nm peak, while the hybrid organic/inorganic LED also demonstrates a clear broad second peak from the F8BT from 500 nm. Figure 4.5 also provides initial evidence of energy transfer with a 42 % quenching of the InGaN/GaN MQW PL emission with the organic/inorganic hybridisation, as observed previously[5,30].

FRET is typically characterised using time-resolved PL (TRPL) measurements,

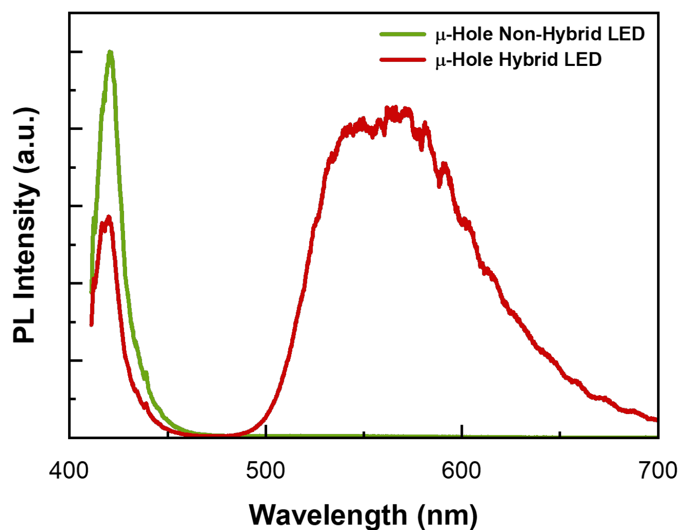

Figure 4.5: Room-temperature PL spectrum of the micro-hole array structured blue LED and hybrid organic/inorganic white LED under 375 nm CW laser diode excitation.

observing a change in the MQW recombination dynamics of the same compatible structured LED device with and without the possibility of FRET near-field interactions[5,29–34]. TRPL measurements have therefore been performed on the micro-hole array structured blue LED and hybrid organic/inorganic LED. These measurements are completed using a 375 nm pulsed laser diode time-correlated single photon counting (TCSPC) system, as described in section 3.3.1. The same LED sample with a 2D micro-hole array structure was measured before and after F8BT deposition in an optical cryostat under identical 10^{-6} mBar vacuum and room-temperature conditions. This eliminates as far as is reasonably practicable the effects of photo-oxidation in the organic material, with a combined negligible exposure to air and background light irradiation.

Figure 4.6 presents the room-temperature TRPL decay traces of the leading micro-hole array structured blue LED and hybrid organic/inorganic LED at the InGaN/GaN MQW peak emission, showing highest visible reduction in decay lifetime (k^{-1}) with the organic/inorganic hybridisation. This reduction cannot be observed without involvement of the non-radiative FRET process[6].

The decay parameters are extracted from a standard bi-exponential fit, as de-

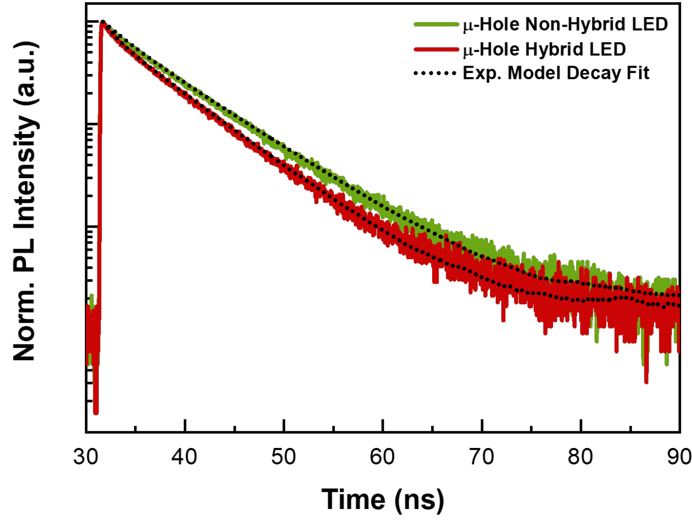

Figure 4.6: Room-temperature peak MQW normalised TRPL decay traces of the leading micro-hole array structured blue LED and hybrid organic/inorganic white LED under 375 nm pulsed laser diode excitation.

fined in equation (4.1). The two-component PL decay is described as having two decay elements, attributed first to the relaxation of localised excitons and second the exciton relaxation of free carriers and localised states[35], where α_x and τ_x define the individual magnitude and decay lifetime of the two terms. Furthermore, the decay rate is equal to $k_x = \tau_x^{-1}$.

$$I(t) = \alpha_1 exp(-\frac{t}{\tau_1}) + \alpha_2 exp(-\frac{t}{\tau_2}) \tag{4.1}$$

$\mathbf{I(t)}$ = instantaneous intensity

$\boldsymbol{\alpha_x}$ = bi-exponential magnitude decay components

$\boldsymbol{\tau_x}$ = bi-exponential lifetime decay components

A significant number of measurements have been repeatedly performed, as in Figure 4.6 and 4.7, demonstrating a decrease in the decay lifetime in 88.9 % of all measured devices. The FRET rate between the InGaN/GaN MQWs and F8BT can be obtained by extracting the change in decay lifetimes measured from the micro-hole array structured blue LED and hybrid organic/inorganic LED, shown in Table

4.1. TRPL measurements as expected evidence a consistent reduction in the decay lifetime (τ) in a hybrid LED, otherwise absent without FRET, with exception to the device in Figure 4.7h.

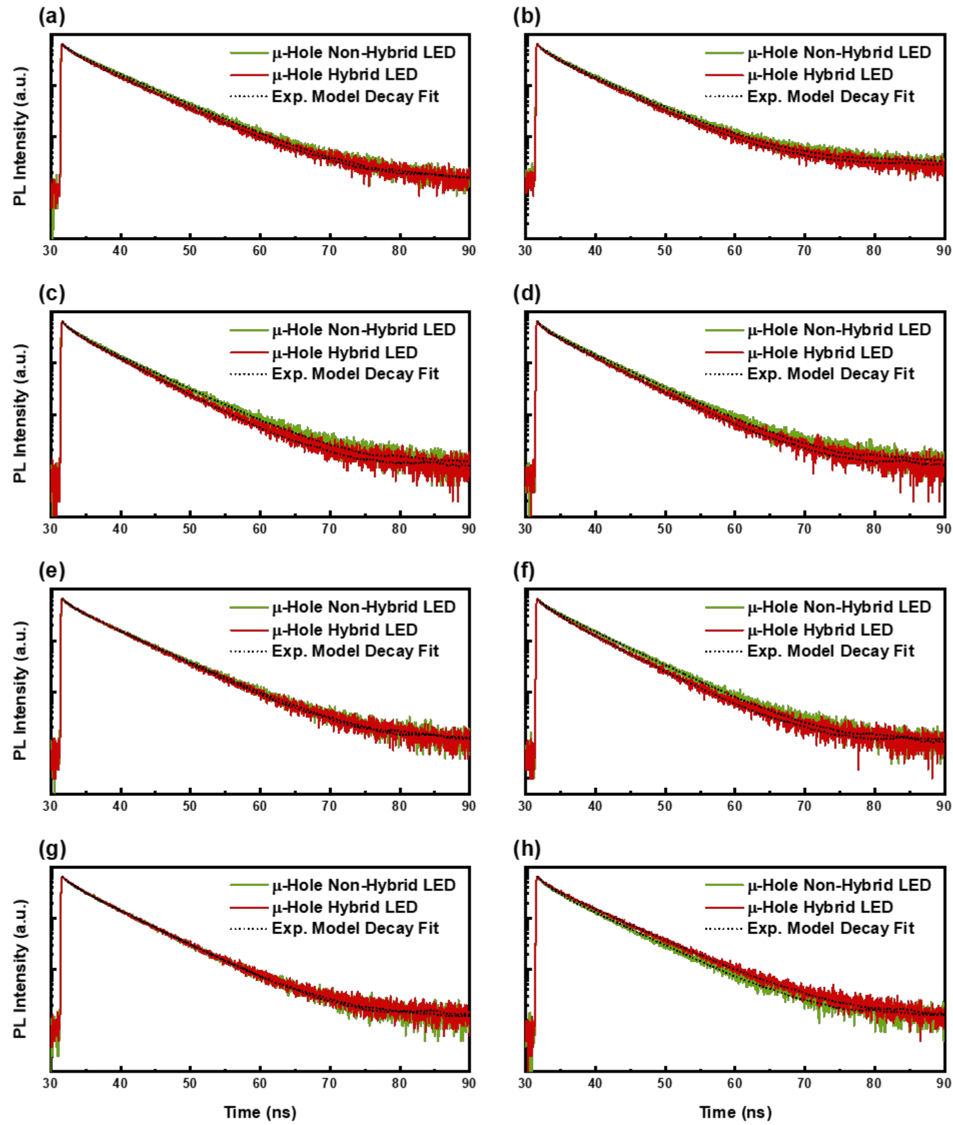

Figure 4.7: Room-temperature peak MQW TRPL decay traces of the remaining (a-h) micro-hole array structured blue LEDs and hybrid organic/inorganic white LEDs under 375 nm pulsed laser diode excitation.

The decay rate of a bare InGaN/GaN LED (k_{MQW}) is dependent on just radiative (k_r) and non-radiative (k_{nr}) recombination rates, as is given in equation (4.2).

FRET coupling in a hybrid device however generates a change in decay dynamics, in that an additional energy transfer channel is present. This meaning that the total recombination rate ($k_{Hyb.}$) requires modification in order to include a non-radiative FRET (k_{FRET}) decay term, as in equation (4.3)[5].

$$k_{MQW} = k_r + k_{nr} \tag{4.2}$$

$$k_{Hyb.} = k_r + k_{nr} + k_{FRET} \tag{4.3}$$

$\mathbf{k_{MQW}}$ = total inorganic multi-quantum well recombination rate

$\mathbf{k_r}$ = radiative recombination rate

$\mathbf{k_{nr}}$ = non-radiative recombination rate

$\mathbf{k_{Hyb.}}$ = total hybrid organic/inorganic recombination rate

$\mathbf{k_{FRET}}$ = FRET recombination rate

The efficiency of the non-radiative FRET process can ultimately be determined from the measured difference in decay rates between the patterned inorganic blue and hybrid white LED, isolating the FRET rate, as considered quite standard[5,6,9,12,28–34]. This assuming reasonably that the MQW radiative and non-radiative recombination rates remain constant with F8BT deposition to cancel out the common factors, excluding the effects of the additional k_{FRET} term.

$$\bar{\tau} = \frac{\alpha_1 \tau_1^2 + \alpha_2 \tau_2^2}{\alpha_1 \tau_1 + \alpha_2 \tau_2} \tag{4.4}$$

$\bar{\boldsymbol{\tau}}$ = average weighted lifetime

The average weighted lifetime ($\bar{\tau}$) of a bi-exponential decay, calculated using equation (4.4)[36], results in a highest decrease from 6.6 to 5.7 ns with the organic/inorganic hybridisation, as shown in Figure 4.6. This corresponds to an accelerated decay rate of $k_{MQW} = 0.15\ ns^{-1}$ to $k_{Hyb.} = 0.18\ ns^{-1}$, isolating a 0.03 ns^{-1} FRET rate that produces a 16.7 % FRET efficiency from equation (4.5)[5,28,30].

$$\eta_{FRET} = \frac{k_{FRET}}{k_{FRET} + k_{MQW}} \tag{4.5}$$

$$\eta_{\mathbf{FRET}} = \text{FRET efficiency}$$

Table 4.1: Room-temperature peak MQW TRPL decay parameter and calculated FRET efficiency of the leading and remaining (a-h) micro-hole array structured blue LEDs and hybrid organic/inorganic white LEDs (shown to 2 d.p.).

Figure		α_1	τ_1	α_2	τ_1	$\bar{\tau}$	$\Delta\bar{\tau}$	$\bar{k}$	k_{FRET}	η_{FRET}
		a.u.	*ns*	*a.u.*	*ns*	*ns*	*ns*	ns^{-1}	ns^{-1}	%
4.6	–	207.8	2.36	756.9	6.99	6.60	0.95	0.15	0.03	16.67 ±2.06
		289.9	1.36	731.7	6.04	5.65		0.18		
4.7	a	211.3	1.31	777.8	7.25	6.98	0.44	0.14	0.01	6.67 ±2.30
		261.0	1.54	723.7	6.94	6.54		0.15		
	b	257.9	1.78	713.4	7.02	6.58	0.34	0.15	0.01	6.25 ±2.55
		291.6	1.22	710.2	6.62	6.24		0.16		
	c	281.8	1.61	698.3	6.68	6.23	0.55	0.16	0.02	11.11 ±2.45
		291.9	1.01	733.9	6.00	5.68		0.18		
	d	243.5	1.26	756.4	6.65	6.34	0.40	0.16	0.01	5.88 ±2.45
		292.6	0.94	734.5	6.24	5.94		0.17		
	e	241.5	1.24	754.4	6.97	6.67	0.26	0.15	0.01	6.25 ±2.31
		228.5	1.06	800.1	6.65	6.41		0.16		
	f	210.4	1.12	787.8	6.53	6.29	0.57	0.16	0.02	11.11 ±2.32
		282.5	1.36	721.1	6.11	5.72		0.18		
	g	239.3	1.45	754.0	6.45	6.12	0.05	0.16	0.01	5.88 ±2.50
		229.0	1.21	782.6	6.34	6.07		0.17		
	h	308.9	1.42	671.7	6.62	6.16	-0.47	0.16	-0.01	-6.67 ±2.79
		272.5	1.41	731.6	7.02	6.63		0.15		

TRPL decay parameter and FRET efficiency of the measured device are each included in Table 4.1, accounting for the effects of non-uniformity in the fabrication process. It is evident that the bi-exponential average weighted lifetime ($\bar{\tau}$) is lower statistically after the organic/inorganic hybridisation of the micro-hole array structured LED; though measurements with and without F8BT may not have been made at identical locations on the same device. However, an approximate 88.9 % of the devices show a degree of improvement with an average 8.73 % FRET efficiency.

It is also worth highlighting that the FRET efficiency is often corrected by aver-

aging across the active FRET interaction area or generated electron-hole pairs experiencing FRET[5,33]. A corrected FRET efficiency would therefore be significantly increased, but is not calculated here[5,30]. The FRET interaction area of an individual micro-hole can be determined by anticipating a 10 nm dipole-dipole separation following the micro-hole circumference, outside which FRET cannot occur. Using this assumption and other known dimensions of the device and photomask it can be reliably estimated that just 0.64 % of the device volume contributes to the highly-efficient non-radiative FRET process. The relatively small area in which recombination is dominated by the fast-acting FRET process between the InGaN/GaN MQW and F8BT highlights the enhancement in down-converted yellow emission.

4.4 Conclusion

In summary, an electrically injected hybrid organic/inorganic III-nitride white LED has been demonstrated with an architecture compatible with the near-field requirements of non-radiative FRET, providing an increased dipole-dipole proximity. A top-down 2D micro-hole array structure is transferred to the InGaN/GaN MQW of a standard blue planar LED using a novel combination of standard fabrication process. The resulting device maintains relatively unchanged electrical performance and a white light EL spectrum with typical CIE colour co-ordinates at (0.29, 0.32). TRPL measurements of the compatible LED reveal consistent reduction in recombination lifetime of the InGaN/GaN MQW with organic/inorganic hybridisation, confirming FRET between the inorganic LED and OLEP. The non-radiative FRET process contributes a 16.7 % best FRET efficiency across a device in which it can account a 0.64 % total interaction area, suppressing likely non-radiative recombination mechanics and therefore enhancing total device efficiency.

4.5 References

[1] C. Chow, C. Yeh, Y. Liu, and Y. Liu, "Improved modulation speed of LED visible light communication system integrated to main electricity network", Electronics Letters **47**, 867 (2011).

[2] J. Vucic, C. Kottke, S. Nerreter, A. Buttner, K.-D. Langer, and J. W. Walewski, "White Light Wireless Transmission at 200+ Mb/s Net Data Rate by Use of Discrete-Multitone Modulation", IEEE Photonics Technology Letters **21**, 1511–1513 (2009).

[3] N. Laurand, B. Guilhabert, J. McKendry, A. E. Kelly, B. Rae, D. Massoubre, Z. Gong, E. Gu, R. Henderson, and M. D. Dawson, "Colloidal quantum dot nanocomposites for visible wavelength conversion of modulated optical signals", Optical Materials Express **2**, 250 (2012).

[4] V. M. Agranovich, Y. N. Gartstein, and M. Litinskaya, "Hybrid resonant organic-inorganic nanostructures for optoelectronic applications", Chemical Reviews **111**, 5179–5214 (2011).

[5] R. Smith, B. Liu, J. Bai, and T. Wang, "Hybrid III-Nitride/Organic Semiconductor Nanostructure with High Efficiency Nonradiative Energy Transfer for White Light Emitters", Nano Letters **13**, 3042–3047 (2013).

[6] M. Achermann, M. a. Petruska, S. Kos, D. L. Smith, D. D. Koleske, and V. I. Klimov, "Energy-transfer pumping of semiconductor nanocrystals using an epitaxial quantum well.", Nature **429**, 642–646 (2004).

[7] Š. Kos, M. Achermann, V. I. Klimov, and D. L. Smith, "Different regimes of Förster-type energy transfer between an epitaxial quantum well and a proximal monolayer of semiconductor nanocrystals", Physical Review B **71**, 205309 (2005).

[8] V. M. Agranovich, D. M. Basko, G. C. L. Rocca, and F. Bassani, "Excitons and optical nonlinearities in hybrid organic-inorganic nanostructures", Journal of Physics: Condensed Matter **10**, 9369–9400 (1998).

[9] M. Achermann, M. a. Petruska, D. D. Koleske, M. H. Crawford, and V. I. Klimov, "Nanocrystal-based light-emitting diodes utilizing high-efficiency nonradiative energy transfer for color conversion", Nano Letters **6**, 1396–1400 (2006).

[10]S. Blumstengel, S. Sadofev, C. Xu, J. Puls, and F. Henneberger, "Converting Wannier into Frenkel excitons in an inorganic/organic hybrid semiconductor nanostructure", Physical Review Letters **97**, 8–11 (2006).

[11]G. Heliotis, G. Itskos, R. Murray, M. D. Dawson, I. M. Watson, and D. D. C. Bradley, "Hybrid inorganic/organic semiconductor heterostructures with efficient non-radiative energy transfer", Advanced Materials **18**, 334–338 (2006).

[12]J. J. Rindermann, G. Pozina, B. Monemar, L. Hultman, H. Amano, and P. G. Lagoudakis, "Dependence of resonance energy transfer on exciton dimensionality", Physical Review Letters **107**, 1–5 (2011).

[13]G. Itskos, C. R. Belton, G. Heliotis, I. M. Watson, M. D. Dawson, R. Murray, and D. D. C. Bradley, "White light emission via cascade Förster energy transfer in (Ga, In)N quantum well/polymer blend hybrid structures", Nanotechnology **20**, 275207 (2009).

[14]D. Andrews, "A unified theory of radiative and radiationless molecular energy transfer", Chemical Physics **135**, 195–201 (1989).

[15]D. L. Andrews and D. S. Bradshaw, "Virtual photons, dipole fields and energy transfer: a quantum electrodynamical approach", European Journal of Physics **25**, 845–858 (2004).

[16]H. Sahoo, "Förster resonance energy transfer - A spectroscopic nanoruler: Principle and applications", Journal of Photochemistry and Photobiology C: Photochemistry Reviews **12**, 20–30 (2011).

[17]N. J. Findlay, J. Bruckbauer, A. R. Inigo, B. Breig, S. Arumugam, D. J. Wallis, R. W. Martin, and P. J. Skabara, "An organic down-converting material for white-light emission from hybrid LEDs.", Advanced materials (Deerfield Beach, Fla.) **26**, 7290–7294 (2014).

[18]S. Guha, R. a. Haight, N. a. Bojarczuk, and D. W. Kisker, "Hybrid organic–inorganic semiconductor-based light-emitting diodes", Journal of Applied Physics **82**, 4126 (1997).

[19]F. Hide, P. Kozodoy, S. P. DenBaars, and A. J. Heeger, "White light from InGaN/conjugated polymer hybrid light-emitting diodes", Applied Physics Letters **70**, 2664 (1997).

[20]M. S. Jeong, J. Y. Kim, Y.-W. Kim, J. O. White, E.-K. Suh, C.-H. Hong, and H. J. Lee, "Spatially resolved photoluminescence in InGaN/GaN quantum wells by near-field scanning optical microscopy", Applied Physics Letters **79**, 976–978 (2001).

[21]K. Okamoto, J. Choi, Y. Kawakami, M. Terazima, T. Mukai, and S. Fujita, "Submicron-Scale Photoluminescence of InGaN/GaN Probed by Confocal Scanning Laser Microscopy", Japanese Journal of Applied Physics **43**, 839–840 (2004).

[22]K. Okamoto, A. Kaneta, Y. Kawakami, S. Fujita, J. Choi, M. Terazima, and T. Mukai, "Confocal microphotoluminescence of InGaN-based light-emitting diodes", Journal of Applied Physics **98**, 064503 (2005).

[23]J. Bruckbauer, P. R. Edwards, S.-L. Sahonta, F. C.-P. Massabuau, M. J. Kappers, C. J. Humphreys, R. A. Oliver, and R. W. Martin, "Cathodoluminescence hyperspectral imaging of trench-like defects in InGaN/GaN quantum well structures", Journal of Physics D: Applied Physics **47**, 135107 (2014).

[24]P. Lane, "Polyfluorene Electroluminescence", in *Organic light-emitting devices: a survey*, edited by J. Shinar, 1st ed. (Springer-Verlag New York, Inc., New York, 2004) Chap. 10, pp. 265–299.

[25]S. Linde and R. Shikler, "Comprehensive study of the influence of different environments on degradation processes in F8BT: Correlating optoelectronic properties with Raman measurements", Journal of Applied Physics **114** (2013).

[26]B. Sun, L. Zhao, T. Wei, X. Yi, Z. Liu, G. Wang, and J. Li, "Shape designing for light extraction enhancement bulk-GaN light-emitting diodes", Journal of Applied Physics **113** (2013).

[27]E. F. Schubert, *Light-Emitting Diodes*, 1st ed. (Cambridge University Press, Cambridge, 2003).

[28]C. R. Belton, G. Itskos, G. Heliotis, P. N. Stavrinou, P. G. Lagoudakis, J. Lupton, S. Pereira, E. Gu, C. Griffin, B. Guilhabert, I. M. Watson, A. R. Mackintosh, R. A. Pethrick, J. Feldmann, R. Murray, M. D. Dawson, and D. D. C. Bradley, "New light from hybrid inorganic–organic emitters", Journal of Physics D: Applied Physics **41**, 094006 (2008).

[29] Z. Zhuang, X. Guo, B. Liu, F. Hu, Y. Li, T. Tao, J. Dai, T. Zhi, Z. Xie, P. Chen, D. Chen, H. Ge, X. Wang, M. Xiao, Y. Shi, Y. Zheng, and R. Zhang, "High Color Rendering Index Hybrid III-Nitride/Nanocrystals White Light-Emitting Diodes", Advanced Functional Materials **26**, 36–43 (2016).

[30] R. M. Smith, M. Athanasiou, J. Bai, B. Liu, and T. Wang, "Enhanced non-radiative energy transfer in hybrid III-nitride structures", Applied Physics Letters **107**, 121108 (2015).

[31] X. Xu and H. Wang, "Resonant energy transfer between patterned InGaN/GaN quantum wells and CdSe/ZnS quantum dots", Nanoscale **8**, 342–347 (2016).

[32] C. Krishnan, M. Brossard, K.-Y. Lee, J.-K. Huang, C.-H. Lin, H.-C. Kuo, M. D. B. Charlton, and P. G. Lagoudakis, "Hybrid photonic crystal light-emitting diode renders 123% color conversion effective quantum yield", Optica **3**, 503 (2016).

[33] S. Chanyawadee, P. G. Lagoudakis, R. T. Harley, M. D. B. Charlton, D. V. Talapin, H. W. Huang, and C. H. Lin, "Increased color-conversion efficiency in hybrid light-emitting diodes utilizing non-radiative energy transfer", Advanced Materials **22**, 602–606 (2010).

[34] S. Nizamoglu, B. Guzelturk, D. W. Jeon, I. H. Lee, and H. V. Demir, "Efficient nonradiative energy transfer from InGaN/GaN nanopillars to CdSe/ZnS core/shell nanocrystals", Applied Physics Letters **98**, 48–51 (2011).

[35] S.-W. Feng, Y.-C. Cheng, C.-C. Liao, Y.-Y. Chung, C.-W. Liu, C.-C. Yang, Y.-S. Lin, K.-J. Ma, and J.-I. Chyi, "Two-Component Photoluminescence Decay in InGaN/GaN Multiple Quantum Well Structures", physica status solidi (b) **228**, 121–124 (2001).

[36] J. R. Lakowicz, *Principles of Fluorescence Spectroscopy*, 3rd ed. (Springer US, Boston, MA, 2006), pp. 1–954.

Chapter 5

Polarised Light Emission from Inorganic and Hybrid Organic/Inorganic Nano-Grating Structured Device

Reproduced (in part) with permission from Scientific Reports 2017, 7, 39677.
Copyright © 2017 Springer Nature.

A highly polarised light emission from optically-pumped hybrid organic/inorganic (white) and electrically injected InGaN/GaN inorganic (blue) devices has been achieved with the fabrication of one-dimensional (1D) nano-grating structures. 1D nano-grating structures through the InGaN-based inorganic multi-quantum well (MQW) acts first to generate a polarised blue emission; high-polarised yellow emission is then realised with alignment of the high-efficiency F8BT organic light-emitting polymer (OLEP) to the periodic nano-grating channels through an enhanced polymer chain confinement, producing together down-converted polarised white light. The polarisation dependent measurements show that the hybrid organic/inorganic devices demonstrates a combined polarisation degree up to 44 % with the smallest nano-channel width, where electrically injected blue emitting devices have a highest 34 % polarisation degree with largest nano-grating duty-cycle. The near-field donor (InGaN/GaN MQW) and acceptor (F8BT) dipole arrangement of the nano-grating structured hybrid device also enables the possibility for the highly-efficient Förster resonance energy transfer (FRET) colour-conversion process. Time-resolved photoluminescence (TRPL) measurements have shown a maximum FRET efficiency reaching 31.3 %, where the FRET interaction volume accounts just approximately 3.91 % of the remaining blue emitting nano-grating structure, enhancing total device efficiency. The approach developed here allows the fabrication of both high-efficiency polarised blue and white light-emitting devices.

5.1 Introduction

In the last twenty years there has been an unprecedented development in solid-state white lighting based on III-nitride blue light-emitting diodes (LEDs)[1], leading to a semiconductor lighting revolution with the provision of significant reductions in energy consumption. The combination of a blue emitting InGaN/GaN LED with down-conversion yellow phosphor is still the main approach to achieving white light. However, this method has a number of major drawbacks, which includes self-absorption and the induced inefficient conversion of blue to longer wavelength yellow light. The low-quality colour-rendering has also been linked negatively to human behaviours in sleep patterns and subsequently mental health[2]. In addition, the existing approach generates significant limitations in application of display backlighting that first requires polarised white light, as well as in visible light

communication (VLC) that is otherwise restricted in bandwidth by the intrinsically slow-response time of phosphors.

A number of approaches have been proposed in order to address these challenging issues, such as monolithically integrated white LEDs, hybrid inorganic/inorganic colloidal quantum-dots and hybrid inorganic/organic conjugated polymers[3–8]. The ideal solution would be a monolithically grown white LED with all necessary emission components (blue and yellow) exhibiting both polarised and high-efficiency performance. However, the well-known quantum-confined Stark effect (QCSE) makes growth of III-nitride materials that emit beyond the blue spectral region quite difficult[9,10], leading to a significant reduction in quantum efficiency. At present this approach is therefore considered unlikely as it would require a high-efficiency yellow emission with a large degree of both optical polarisation and emission matched to the polarised blue light. Additionally, emission from a standard c-plane LED is intrinsically unpolarised.

A combination of CdSe/ZnS colloidal quantum-dots with inorganic III-N blue LEDs have been used previously to achieve high-performance white light sources with excellent CIE chromaticity co-ordinates and colour-rendering index (CRI) value[11,12]. This method still faces the significant challenge of achieving polarised white light. Compared to existing phosphors or colloidal quantum-dots, down-conversion OLEPs have a number of key advantages, which includes first a high PL quantum efficiency in the yellow spectral region. It is also well-known that an OLEP exhibits generally a large Stokes-shift, effectively eliminating issues of self-absorption. In addition, the solubility of organic materials can simplify the fabrication process of hybrid organic/inorganic nano-scale structured devices by use of standard spin-coating technique. However, most significantly is that down-converting OLEPs have the potential to allow enhanced colour-conversion efficiency through non-radiative Förster resonance energy transfer (FRET) process[5,12–14]. This means that the colour quality of such hybrid inorganic/organic white LED can be significantly enhanced by contrast to current solid-state devices fabricated using phosphors.

The utilisation of light-emitting conjugated polymers is significant to the fabrication of polarised white emitters, where liquid crystalline (LC) phases can exist due to the conjugated backbone and long alkyl side-chains[15]. A liquid-crystal polymer naturally exhibits a preferential alignment on the microscopic domain, demonstrating unique properties such as increased carrier mobility and polarised

light emission[15–18]. Engineering of the alignment properties from the microscopic to macroscopic scale therefore allows polarised light to be effectively produced[19].

A further requirement is to convert the unpolarised blue emission from a standard c-plane InGaN/GaN multi-quantum well (MQW) structure into polarised light. The fabrication of a one-dimensional (1D) nano-grating structure through the MQW is a promising approach, in such case the structure can also serve as a polariser. Combining the inorganic nano-structured LED with a conjugated OLEP compatibly will produce a hybrid organic/inorganic device that is potentially capable of emitting highly polarised white light with high CRI.

A number of approaches have also been explored in the alignment of conjugated polymer chains, which include nano-imprinting, electro-spinning and thermomechanical alignment techniques[15,18,20–23]. In this work a novel and efficient method for fabricating 1D nano-grating structures in a standard InGaN/GaN MQW epi-wafer is demonstrated, producing polarised blue emission. The 1D nano-grating consists of a large number of periodic channels into which yellow emitting F8BT OLEP can be filled, nano-channels are then further used to accurately align the polymer chains over the macroscopic domain in generation of polarised yellow light.

Such a hybrid organic/inorganic structure is also expected to result in a significant enhancement in the radiation-less FRET process between InGaN/GaN MQW (donor) and F8BT (acceptor) through dipole-dipole Coulombic interactions. As a result of FRET a reduction in non-radiative recombination dynamics in the donor material is expected due to the additional channels by which excitons can now transfer to the acceptor. The near-field FRET process is highly sensitive to the dipole-dipole separation (< 10 nm)[14,24], and also the resonant overlap between respective dipole emission and absorption spectrum. The optimisation of these parameters can potentially lead to a high FRET rate that in turn would dramatically increase the white light colour-conversion efficiency. This has previously been demonstrated with the fabrication of a hybrid organic/inorganic device with an underlying self-assembled nano-rod structure that minimises this dipole-dipole separation[14,25]. However, due to the perceived arbitrary nature of the self-assembled III-nitride nano-rod arrays and random distribution of F8BT, polarised white light cannot be achieved.

In this work, as mentioned, hybrid organic/inorganic top-down nano-structured devices containing periodic nano-channels of different widths are fabricated in

standard c-plane InGaN/GaN MQW, where F8BT is then effectively filled into the nano-channels. The hybrid configuration can also allow effective manipulation of the relative orientation of donor-acceptor dipoles to produce polarised emission. The resulting high-efficiency polarised white light source is particularly useful in display-screen backlighting applications.

5.2 Hybrid Nano-Grating Photoluminescence

5.2.1 Fabrication

A standard five-period InGaN/GaN MQW epi-wafer is used in the PL investigation, where each InGaN quantum well has a 2.5 nm thickness and approximate 20 % indium content between 10 nm GaN barriers. The samples are grown on a double-side polished c-plane sapphire substrate using a metal-organic chemical vapour deposition (MOCVD) system. The structure also includes an initial high-temperature 200 nm AlN buffer-layer, 1.2 µm undoped GaN and a final 10 nm GaN capping-layer above the MQW.

A commercial WITec Alpha300 confocal microscopy system equipped with a 375 nm excitation laser diode has been repurposed to direct-write 1D nano-grating mask patterns on a sub-micron scale using high-powered laser ablation of soft photoresist material. The patterned gratings are then transferred through the InGaN/GaN MQW structure using subsequent combined dry-etch techniques.

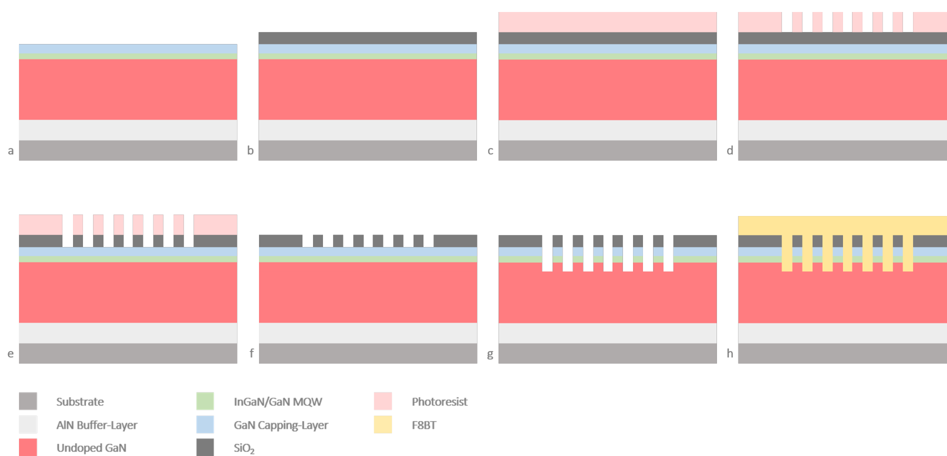

Figure 5.1: Schematic diagram of the nano-grating structured hybrid organic/inorganic device fabrication process (a-h).

Figure 5.1 shows a schematic diagram of the complete fabrication process (a-h) producing the 1D nano-grating structured hybrid organic/inorganic white device. A (b) 250 nm thick SiO_2 layer is first deposited directly on top of the epi-wafer using plasma-enhanced vapor deposition (PECVD), serving later as secondary hard mask. Next (c) a thin (650 nm) negative-tone photoresist film is spin-coated, before UV flood exposure and development that allows further processing outside yellow light conditions. The nano-grating patterns are then (d) written into the photoresist soft-mask through high-powered laser ablation using a confocal fluorescence microscopy system, which has a 100x magnification and 0.95 NA objective that provides an approximate 480 nm focused laser spot-size. The 1D array patterns are transferred utilising the systems high-resolution XYZ piezoelectric scan-stage, which raster-scans the sample relative to the fixed laser over a 70 x 70 µm area. This is followed by an O_2 plasma ash that removes organic residues from within the patterned channels. A (e) standard CHF_3/Ar reactive-ion etch (RIE) process is then used to subsequently transfer this pattern to the SiO_2, acting as a hard-mask in the subsequent step to overcome issues of etch-rate selectivity. The nano-grating structure (g) is then formed through InGaN/GaN MQW using an Cl_2/Ar inductively coupled plasma (ICP) etching, resulting in an approximate combined 500 nm etch depth.

A set of nine nano-grating structures each with different channel widths, ranging from 43 to 294 nm with a consistent 510 nm centre-to-centre spacing were fabricated to investigate the polarisation degree relative to the nano-channel width. Figure 5.2 shows the top-view (0°) scanning electron microscope (SEM) images of each of the following nine nano-grating structures.

In the fabrication of the hybrid organic/inorganic device F8BT polymer is dissolved in a 5 mg/mL toluene concentration, which is then (h) spin-coated across the nano-grating structures to fill the nano-channel void with an approximate 1.6 refractive index. This form of OLEP deposition yields microscopic random alignment of the F8BT molecule chains, despite filling the nano-channels. Consequently, the random alignment of polymer chains does not lend itself to polarisation or optimal FRET coupling between the inorganic and organic dipole intrinsically. To then produce a best possible alignment of the OLEP along the nano-channel (h) the hybrid samples are heated for 1 hour to 160 °C, above the F8BT glass transition temperature ($T_g \approx 90$ °C), transforming to its LC phase. A high-pressure is then also simultaneously applied in order to further enhance the alignment of

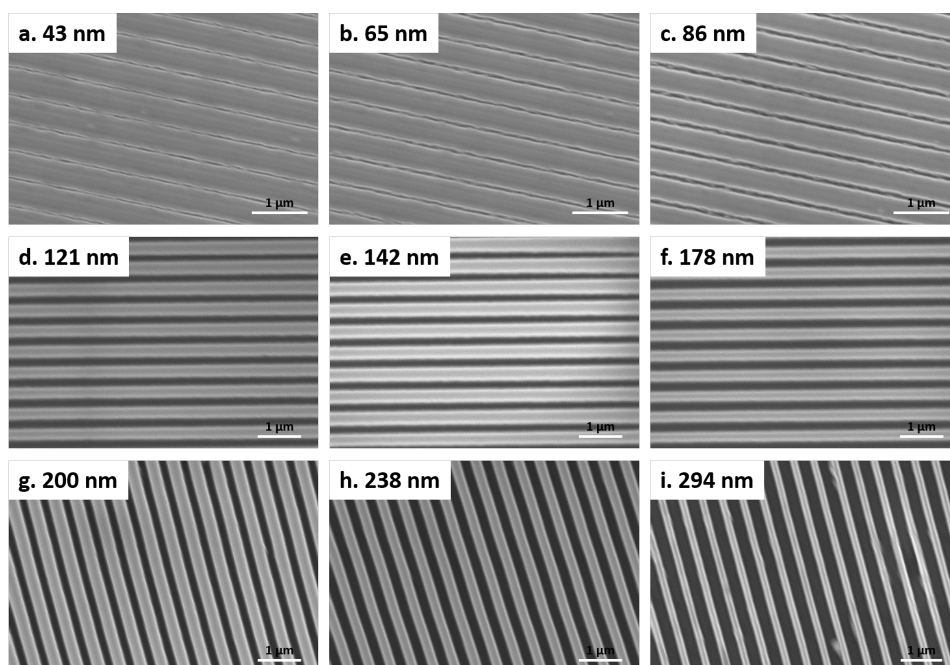

Figure 5.2: SEM images (0° angle) of the (a-i) nano-grating structured devices after etching InGaN/GaN MQW; fixed 510 nm centre-to-centre spacing and nano-channel width ranging 43 - 294 nm.

the F8BT to the nano-channel forcibly between aluminium plates that are maximally torqued. The samples are then left to cool-down to room-temperature, where the chains are again *frozen* in position below the transition temperature, before the applied clamping pressure can be removed. Organic materials are susceptible to degradation in the presence of atmospheric moisture and oxygen, resulting in a permanent emission quenching, therefore organic material processing is completed within an anaerobic (O_2 < 0.5 ppm) glove-box.

5.2.2 Photoluminescence

The room-temperature optical properties of the 1D nano-grating structures have then been investigated as a function of the nano-channel width relative to an un-patterned planar sample, using photoluminescence (PL) measurements with a 375 nm laser diode excitation (section 3.3.1). In the polarisation dependent PL measurements a linear polariser in a 360° continuous rotation mount is placed before the collection fiber.

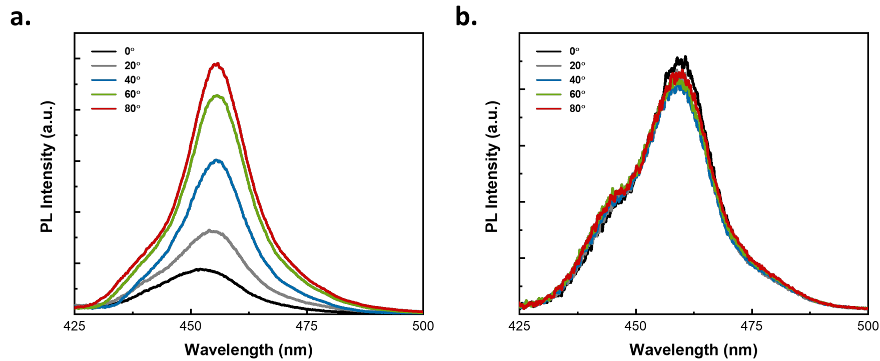

Figure 5.3: Polarisation dependent PL spectrum of the (a) nano-grating (294 nm) and (b) planar structured blue emitting devices under 375 nm CW laser diode excitation.

Figure 5.3 shows the PL spectrum of an inorganic 1D nano-grating structure with a 294 nm channel width as function of the polarisation angle between 0° and 80°, also given as comparison is the polarisation dependent PL spectra of the unpatterned sample. As expected, PL of the unpatterned device remains unchanged with the polarisation angle, this is a result of the unpolarised nature of c-plane InGaN/GaN MQW emission. In contrast an obvious intensity variation and change in peak-emission wavelength with the nano-grating structure is measured with respect to the polarisation angle.

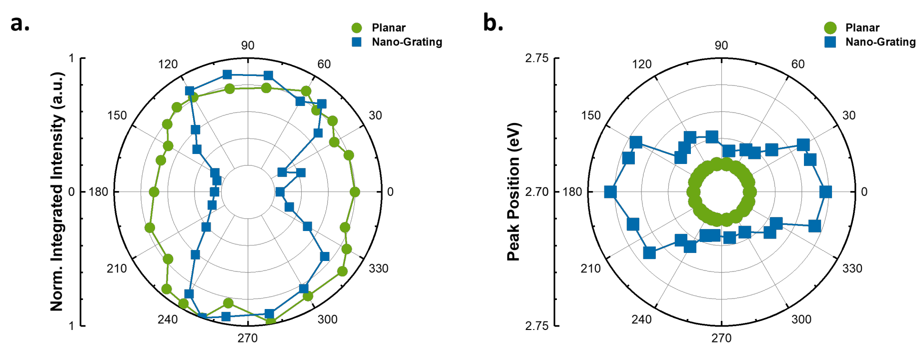

Figure 5.4: Polarisation dependent (a) normalised integrated PL intensity and (b) peak-energy position of the nano-grating (294 nm) and planar structured blue emitting device under 375 nm CW laser diode excitation; plotted in the polar coordinate system.

Figure 5.4a and 5.4b present respectively the integrated PL intensity and peak wavelength position against polarisation angle in the polar co-ordinate system; showing an approximate 20 meV red-shift toward low-energy emission at the highest integrated PL intensity as similarly reported elsewhere in literature[26]. A clear polarised emission is demonstrated with the nano-gratings, while the emission from the unpatterned sample exhibits no polarisation dependent behaviours due to an intrinsic isotropic strain. A strain relaxation can however be introduced through the top-down fabrication into nano-structures, as previously studied[9,10,27].

In the case of the nano-grating structure the 1D configuration leads to an anisotropic strain relaxation; because relaxation takes place only in the direction perpendicular to the grating orientation the intrinsic strain condition resides in the remaining material along the direction of the nano-channels. As a result of the anisotropic strain relaxation two dominant optical transitions then exist due to the valence band splitting between two distinct sub-bands[26,28], where electron-hole pair recombine preferentially at the lowest transition energy, leading to the optical polarisation effects as observed in Figure 5.3 and 5.4.

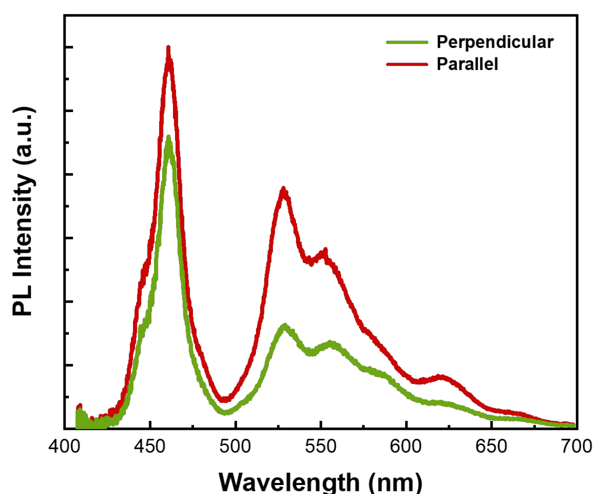

Figure 5.5: PL spectrum of the nano-grating (43 nm) structured hybrid organic/inorganic white emitting device under 375 nm CW laser diode excitation; polariser positioned perpendicular and parallel to the nano-gratings.

The same polarisation dependent PL measurements have also been repeated

with the hybrid nano-grating samples after OLEP deposition. Figure 5.5 then shows the PL spectrum of a hybrid 1D nano-grating structure with a 43 nm channel width, measured at the extreme polarisation angles, where the polariser is positioned parallel and perpendicular to the nano-gratings. The measurements both before and after F8BT deposition are complete under identical high-vacuum room-temperature conditions in an optical cryostat, eliminating effects of photo-oxidation in the organic material.

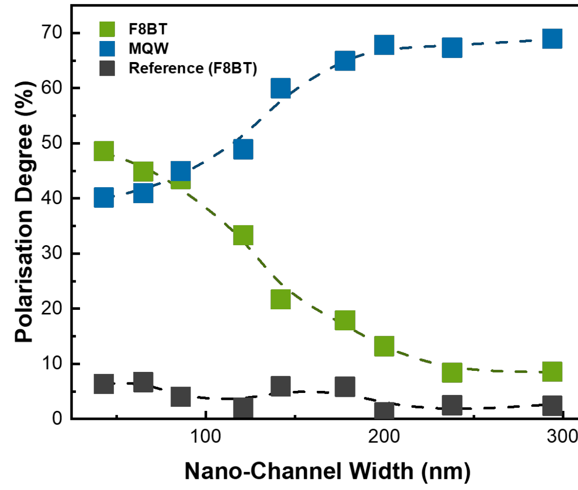

Figure 5.6: Polarisation degree of F8BT, MQW and reference (F8BT) emission of the nano-grating structured hybrid organic/inorganic white emitting device; fixed 510 nm centre-to-centre spacing and nano-channel width ranging 43 - 294 nm.

Figure 5.6 displays the polarisation degree of the nine hybrid nano-grating samples as a function of channel width, considering MQW and OLEP emission separately, polarisation degree is calculated using equation (5.1)[29].

$$\rho = \frac{I_{//} - I_{\perp}}{I_{\perp} + I_{//}} \tag{5.1}$$

$\boldsymbol{\rho}$ = polarisation degree

$\mathbf{I}_{//}$ = total parallel intensity

$\mathbf{I}_{\perp}$ = total perpendicular intensity

A decrease in the polarisation degree is observed from 68 % to 40 % in the inorganic MQW emission with a reducing nano-channel width. The polarised emission from the c-plane InGaN/GaN active region is generated through an anisotropic strain relaxation[26], caused by the fabrication of the nano-grating structure through the MQW. The increasing nano-channel width results in an enhanced anisotropic strain relaxation relative to the constant 510 nm centre-to-centre period, leading to an increase in the polarisation degree[26].

Alternatively, the F8BT polarisation degree increases gradually with a decreasing nano-channel width, allowing polymer chains to exist in fewer different orientations within the channel causing polarisation degree to increase[30]. The highest polarisation degree of the OLEP alone is 48 % with the 43 nm channel width, which for the combined hybrid white emission (MQW and F8BT) gives a 44 % polarisation degree. This suggests that a reduction in nano-channel width enhances the confinement of the F8BT[18], leading to improved alignment of molecules along the nano-grating direction[30].

To further strengthen this theory an identical set of hybrid nano-grating devices were fabricated for comparison, where F8BT polymer is instead filled into the nano-channels without subjection to the previously described macroscopic alignment process. Figure 5.6 includes also the measured PL polarisation degree against nano-channel width of these hybrid reference sample (black); zero polarisation dependent behaviour is exhibited regardless of the dimension. This because the preferential random alignment of molecules is still on the microscopic scale, where neighbouring polymer chains are arranged with different orientation[15–18].

5.2.3 Time-Resolved Photoluminescence

The recombination dynamics of a hybrid organic/inorganic nano-grating structured sample has also been measured, investigating the possible non-radiative FRET process. Room-temperature time-resolved PL (TRPL) measurements have been performed using a time-correlated single photon counting (TCSPC) system, where the excitation source is a 375 nm pulsed laser diode as described in section 3.3.1.

As a comparison an identical nano-grating structure is fabricated with a PMMA top layer, where the absorption spectrum is unmatched to the InGaN/GaN MQW emission, effectively blocking FRET between the donor-acceptor dipole.

Figure 5.7 shows the TRPL decay trace of both the nano-grating structured reference (PMMA) and hybrid (F8BT) sample with the smallest 43 nm channel

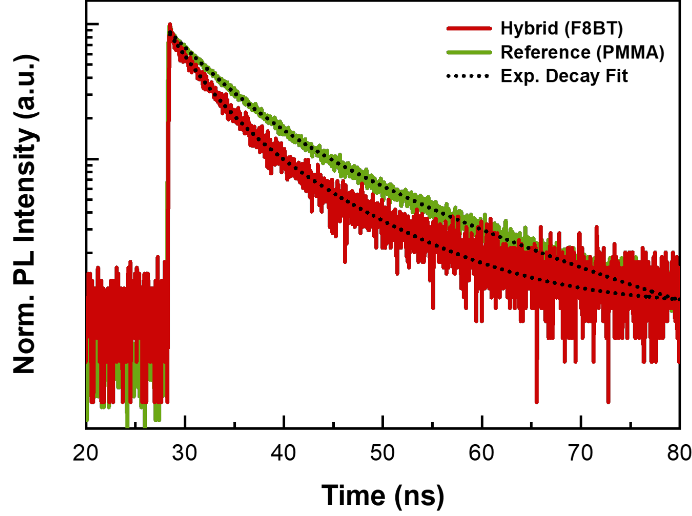

Figure 5.7: Peak MQW normalised TRPL decay traces of the nano-grating (43 nm) structured hybrid organic/inorganic (F8BT) and reference (PMMA) devices under 375 nm pulsed laser diode excitation.

width, measured at the InGaN/GaN MQW peak wavelength ($\sim$ 460 nm). This demonstrates a significantly reduced PL decay lifetime for the hybrid sample with OLEP deposition and LC alignment process.

The decay parameters are extracted from a standard bi-exponential fit, as defined in equation (5.2)[31], where the decay rate is equal to $k_x = \tau_x^{-1}$.

$$I(t) = \alpha_1 exp(-\frac{t}{\tau_1}) + \alpha_2 exp(-\frac{t}{\tau_2}) \tag{5.2}$$

The decay rate of the PMMA coated InGaN/GaN device (k_{MQW}) is dependent on just radiative (k_r) and non-radiative (k_{nr}) recombination rates, as is given again in equation (5.3).

$$k_{MQW} = k_r + k_{nr} \tag{5.3}$$

FRET coupling in the hybrid device with F8BT generates a change in decay dynamics, in that an additional energy transfer channel is present, meaning that the total recombination rate ($k_{Hyb.}$) requires modification in order to include a non-radiative FRET (k_{FRET}) decay term, as in equation (5.4)[14].

$$k_{Hyb.} = k_r + k_{nr} + k_{FRET} \tag{5.4}$$

The efficiency of the non-radiative FRET process can then ultimately be determined from the measured difference in decay rates between the patterned reference PMMA and hybrid inorganic/organic F8BT device, isolating the FRET rate. FRET efficiency is calculated using equation (5.5)[14,24,25].

$$\eta_{FRET} = \frac{k_{FRET}}{k_{FRET} + k_{MQW}} \tag{5.5}$$

The lifetime (τ) from the bi-exponential decay results in a consistent decrease from 4.5 to 3.1 ns in the fast-decay component between the PMMA and F8BT coated hybrid samples, as shown in Figure 5.7. This corresponds to an accelerated decay rate of $k_{MQW} = 0.22\ ns^{-1}$ to $k_{Hyb.} = 0.32\ ns^{-1}$, isolating a 0.10 ns^{-1} FRET rate that produces a highest 31.3 % FRET efficiency.

The FRET efficiency is again often averaged across the active FRET interaction area; corrected FRET efficiency is therefore expected to be significantly enhanced, but is still not included here[32]. The FRET interaction area of an individual nano-channel can be determined by anticipating a 10 nm dipole-dipole separation following the perimeter edge, outside which FRET cannot occur. Using this assumption and other known dimensions it can be reliably estimated that just 3.91 % of the remaining device volume contributes to the highly-efficient non-radiative FRET process. The comparatively small area in which recombination is dominated by the fast-acting FRET between the InGaN/GaN MQW and F8BT highlights the enhancement in the down-converted yellow emission process.

5.3 Inorganic Nano-Grating Electroluminescence

5.3.1 Fabrication

Planar LEDs with a standard 120 × 280 μm size are first fabricated using a commercial blue InGaN/GaN LED wafer grown on c-plane sapphire in this now EL investigation. The epitaxial structure consists of a 1 μm n-GaN layer with a thick undoped GaN buffer on a standard thin low-temperature GaN nucleation layer, 100 nm InGaN pre-layer, 160 nm InGaN/GaN multi-quantum well (MQW) active region and then final 230 nm p-GaN layer.

Figure 5.8 shows a schematic diagram of the complete fabrication process (a-h) producing the 1D nano-grating structured inorganic blue LED. A standard planar LED fabrication (a) briefly involves an initial mesa etch, where parts of the wafer are selectively etched 730 nm into the n-GaN region for the later fabrication of isolated devices. A 100 nm ITO (indium tin oxide) layer is then deposited across the remaining p-type regions, forming an Ohmic p-contact after thermally annealing at 600 °C for 60 seconds in air. The n-contact electrode consists of Ti/Al/Ti/Au (20/100/20/60 nm), before then final Ti/Au (20/200 nm) bond-pads are deposited on both the p-type and n-type contacts.

A 1D nano-grating structure is then fabricated through the active region of a planar LED device using a combination of standard photolithography, novel direct-write laser ablation and selective dry-etching technique.

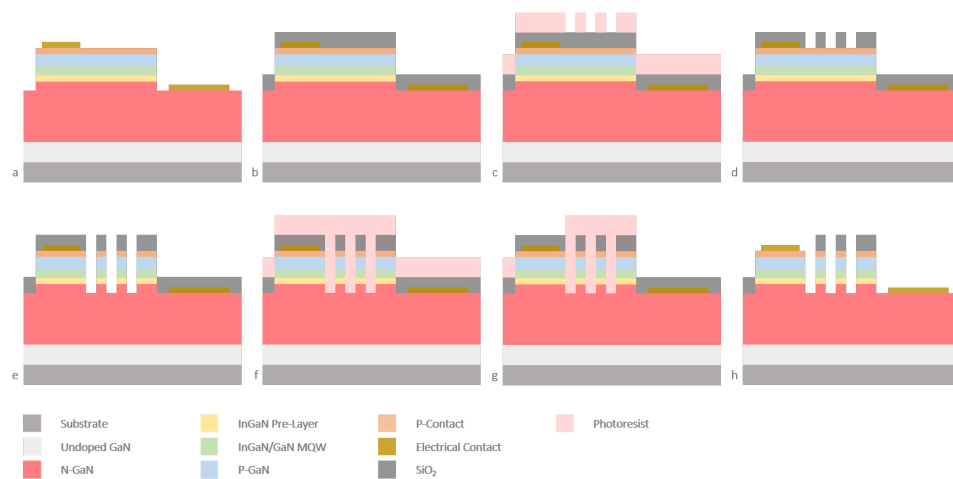

Figure 5.8: Schematic diagram of the nano-grating structured inorganic LED fabrication process (a-h).

The top-down fabrication procedure in detail begins with (b) a 250 nm SiO_2 layer deposited across the fabricated planar LED using PECVD, which later acts as a secondary hard-mask overcoming issues of etch-rate selectivity. A subsequent (c) 650 nm negative-tone photoresist film is then deposited, processing outside yellow light conditions is allowed following UV flood exposure and development. 1D nano-channel arrays are then patterned in the soft photoresist material through a laser ablation direct-write action using a confocal fluorescence microscopy system, which again has a 375 nm laser diode excitation and 100x magnification objective with 0.95 NA. The patterns are written utilising the systems high-resolution XYZ

piezoelectric scan-stage to raster-scan samples over a 70 x 70 µm area relative to a fixed $\sim$ 480 nm focused laser spot-size. The mesa emission area is designed to match the maximum 100 x 100 µm travel range of the scan-stage, restricting size to a single-run exposure. This pattern is (d) then transferred to the SiO_2 layer using a standard CHF_3/Ar RIE process; prerequisite O_2 plasma ashing first removing residual organic matter from within the patterned nano-channels. The preceding 1D nano-grating structure is then (e) formed within the InGaN/GaN MQW of the planar LED using an Cl_2/Ar ICP etch, resulting in an approximate 620 nm depth through the inclusive p-contact. The undamaged n-type and p-type electrodes are then ultimately (f-h) re-exposed using a combined conventional photolithography step and the same selective SiO_2 RIE processing.

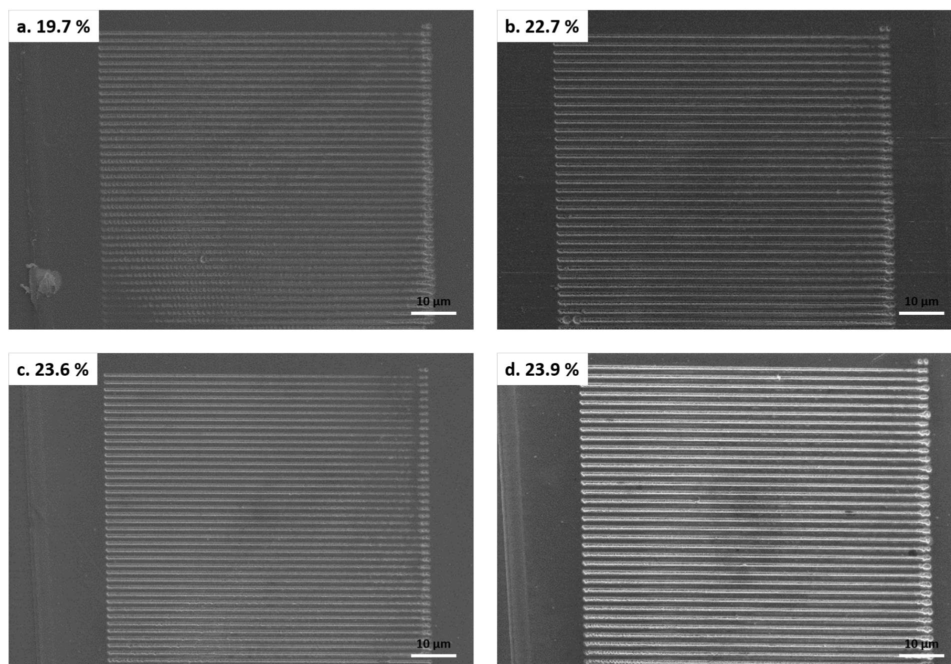

Figure 5.9: SEM images (0° angle) of the (a-d) nano-grating structured inorganic LEDs after etching InGaN/GaN MQW; duty-cycle ranging 19.7 - 23.9 %.

The particular geometric configuration of the nano-grating structured inorganic LED aims to demonstrate similarly polarised blue emission under an applied electrical injection. A necessary consequence to the fabricated top-down structure is an inherently continuous p-GaN layer that is maintained around the nano-channels, allowing full current spreading across the device.

A set of four nano-grating structures each with different channel widths and centre-to-centre spacing are fabricated, characterising effects of polarisation degree relative to duty-cycle. The duty-cycle here is a percentage ratio of channel width to the total period, giving most accurate representation of the remaining anisotropically strained inorganic blue emitting material after the top-down 1D nano-grating fabrication[26].

Figure 5.9 shows the top-view (0°) SEM images of the aforementioned four nano-grating structures, where measured channel width ranges between 332 - 491 nm with either a designed 1.67 µm or 2 µm centre-to-centre spacing. The LED denoted *a*-*d* each assiduously have a respective nano-grating duty-cycle of 19.7 % (332:1687 nm), 22.7 % (451:1987 nm), 23.6 % (395:1672 nm) and 23.9 % (491:2057 nm).

5.3.2 Electroluminescence

The ambient electrical properties of the 1D nano-grating structured LED have been investigated as a function of duty-cycle relative to an unpatterned planar LED, emitting intrinsically unpolarised light in c-plane materials. The devices are all subject to parallel fabrication conditions, where the measured planar LED excludes the mask-less laser ablation process.

Figure 5.10 shows the IV characteristics of the unpatterned planar and nano-grating structured blue LED, including comparison of typical behaviour before and after the top-down fabrication. The electrical properties of an unpatterned planar LED pre-fabrication demonstrate a 3.38 V turn-on voltage (V_o) and 12.4 Ω series resistance; post-fabrication this increases to an average 4.41 V and 63.1 Ω with and without the nano-grating structure. A negative change in IV characteristics is therefore largely attributed to the top-down fabrication process regardless of the device architecture. However, a non-linear increase in series resistance is also observed between LED *a* and *d* from 56.6 Ω to 67.6 Ω, where resistance is related inversely to the remaining cross-sectional area.

Electroluminescence (EL) is captured using a probe-station as described in section 3.3.1, where the approximate 100 x 100 µm emission area is collected simultaneously under 20 mA injection current. This is shown as an optical image inset in Figure 5.10. However, in polarisation dependent measurements the infinity corrected light is instead focused to the parabolic reflective optical-fiber collimator through a 360° continuous rotation linear polariser.

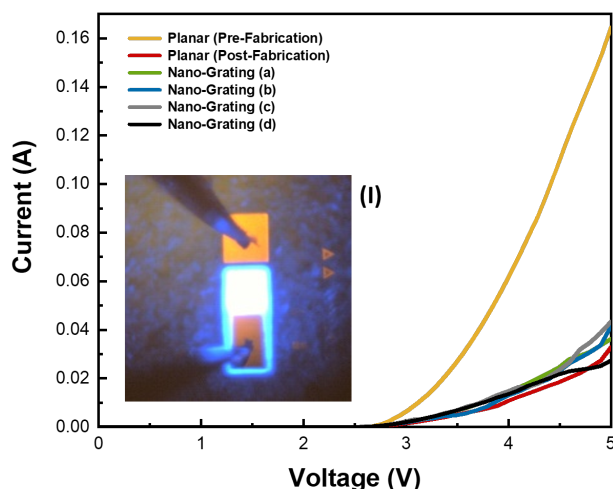

Figure 5.10: IV characteristics of the planar (pre/post-fabrication) and nano-grating structured inorganic LEDs; duty-cycle ranging 19.7 - 23.9 % (a-d). Inset (I) optical image of the nano-grating (23.9 %) structured inorganic blue emitting LED under 20 mA injection current.

Figure 5.11 presents the EL spectrum of the $\sim$ 445 nm blue emitting nano-grating structured LED *d* as a function of polarisation angle from 0° to 80°, as reference the post-fabrication planar LED is also included. EL of the nano-grating structured LED demonstrates significant intensity variation between extreme polarisation angles with a corresponding 2 nm change in the peak-emission wavelength, whereas this remains consistent in the unpatterned LED due to the unpolarised nature of c-plane InGaN/GaN MQW emission.

Figure 5.12 shows the normalised integrated EL intensity of LED *a-d* against polarisation angle in the polar co-ordinate system. A clear polarised emission is demonstrated in each of the nano-grating structures, showing a typical asymmetric behaviour, which is exaggerated with the increasing duty-cycle. The EL emission from a planar LED is also shown as reference, exhibiting again no polarisation dependence because of the intrinsic isotropic strain across a continuous emission area.

The 1D array configuration of a nano-grating structure again leads to an anisotropic strain relaxation. This effect occurs predominately in the directions

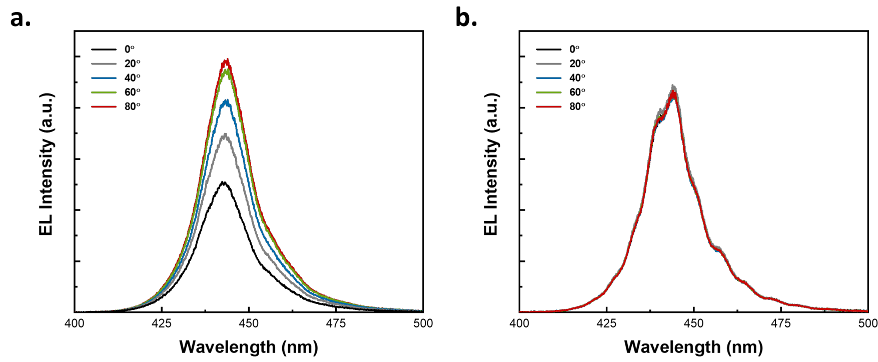

Figure 5.11: Polarisation dependent EL spectrum of the (a) nano-grating (23.9 %) and (b) planar structured inorganic LEDs under 20 mA injection current.

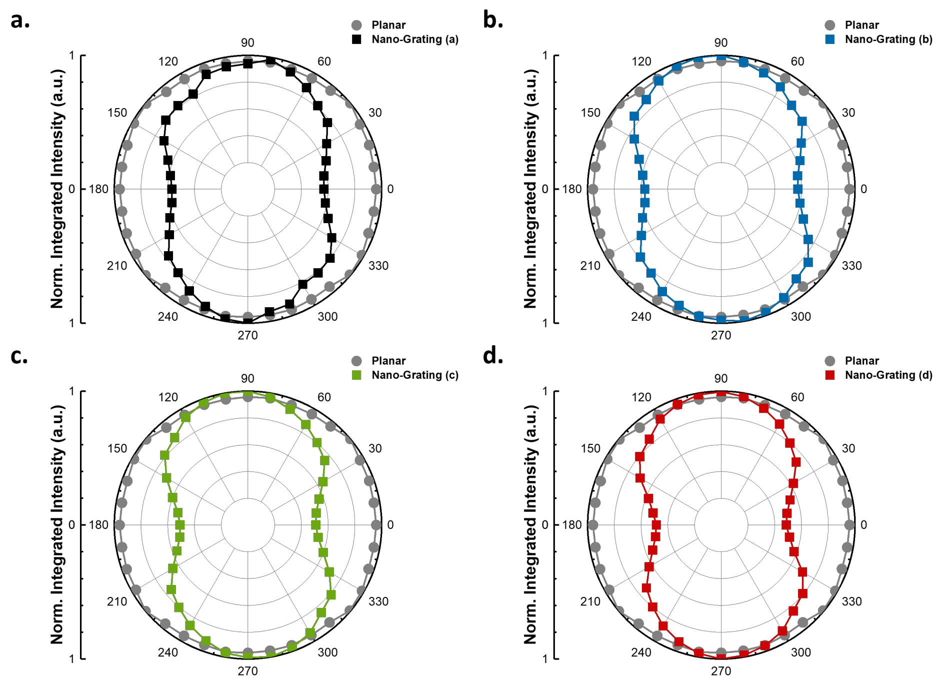

Figure 5.12: Polarisation dependent (a-d) normalised integrated EL intensity of the planar and nano-grating structured inorganic LEDs under 20 mA injection current; plotted in the polar co-ordinate system and duty-cycle ranging 19.7 - 23.9 %.

perpendicular to the grating orientation, which means the intrinsic strained condition resides in the remaining material parallel to the nano-channels. As a result

of the anisotropic strain relaxation the dominant optical transitions are split between distinct sub-bands[26,32], where electron-hole pair recombine preferentially at the lowest transition energy. This is evidenced partially by a red-shift toward low-energy emission at the highest integrated EL intensity[28], leading to the optical polarisation effects as observed in Figure 5.11 and 5.12.

Figure 5.13 displays the polarisation degree of the four nano-grating LED as a function of duty-cycle. The polarisation degree is a ratio of the difference and total intensity measured parallel and perpendicular to the 1D nano-channel array, calculated using equation (5.1)[29]. An improvement in the polarisation degree is observed from 24.4 % to 34.4 % with an increasing nano-channel duty-cycle. The polarised emission is caused by the fabrication of nano-structures through the c-plane InGaN/GaN MQW[9,10,27], generating that anisotropic strain relaxation[26]. The increasing duty-cycle therefore results in a greater anisotropic effect relative to the period over a 70 x 70 μm nano-grating area, leading to an enhanced polarisation degree[26].

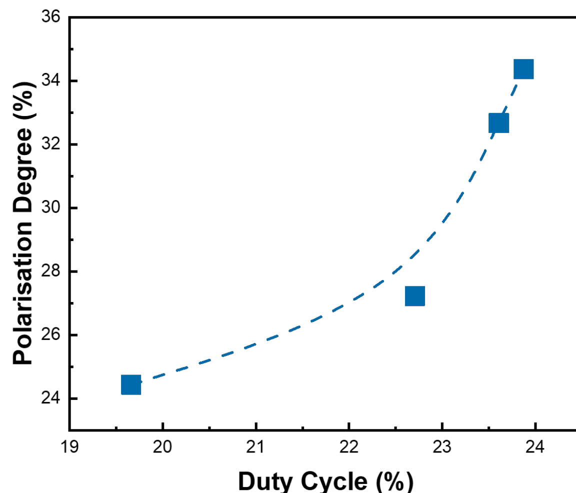

Figure 5.13: Polarisation degree of the MQW emission of the nano-grating structured inorganic LEDs under 20 mA injection current; duty-cycle ranging 19.7 - 23.9 %.

5.4 Conclusion

In conclusion, optically-pumped hybrid organic/inorganic and electrically injected inorganic devices are fabricated with a respective highly polarised white and blue emission. The 1D nano-grating structures were fabricated through application of a novel mask-less laser ablation process, transferring the pattern through the active region using a subsequent dry-etching technique. A nano-structured inorganic active region emits first polarised blue light through an anisotropic strain relaxation, relative to the nano-grating direction. The occupation of F8BT down-converting material to the nano-channel volume then allows the demonstration of polarised yellow light emission, after a LC phase macroscopic alignment process. This together generates a down-converted polarised white light, where a strong relationship between the nano-channel duty-cycle and polarisation degree is observed. The polarisation of a structured InGaN/GaN MQW improves with an increasing channel width, as a result of enhanced strain relaxation; conversely the polarisation degree of F8BT strengthens with a decreasing size, where a greater nano-confinement improves the alignment of polymer chains. Polarisation dependent optical measurements show the hybrid organic/inorganic device with a combined white light polarisation degree up to 44 %, where electrically injected blue emitting devices have a highest 34 % polarisation degree with the largest nano-grating duty-cycle. The effects of near-field FRET process are also considered due to the compatible proximity between donor (InGaN/GaN MQW) and acceptor (F8BT) dipole of the nano-grating structured hybrid device. TRPL measurements characterise a FRET efficiency reaching 31.3 %, where the interaction volume accounts approximately 3.91 % of the remaining MQW structure, enhancing the total device efficiency.

5.5 References

[1] S. Nakamura, M. Senoh, N. Iwasa, and S.-i. Nagahama, "High-Brightness InGaN Blue, Green and Yellow Light-Emitting Diodes with Quantum Well Structures", Japanese Journal of Applied Physics **34**, L797–L799 (1995).

[2] T. Kozaki, S. Kitamura, Y. Higashihara, K. Ishibashi, H. Noguchi, and A. Yasukouchi, "Effect of Color Temperature of Light Sources on Slow-wave Sleep", Journal of PHYSIOLOGICAL ANTHROPOLOGY and Applied Human Science **24**, 183–186 (2005).

[3] B. Damilano, P. Demolon, J. Brault, T. Huault, F. Natali, and J. Massies, "Blue-green and white color tuning of monolithic light emitting diodes", Journal of Applied Physics **108**, 073115 (2010).

[4] S. Jahangir, I. Pietzonka, M. Strassburg, and P. Bhattacharya, "Monolithic phosphor-free InGaN/GaN quantum dot wavelength converter white light emitting diodes", Applied Physics Letters **105** (2014).

[5] M. Achermann, M. a. Petruska, S. Kos, D. L. Smith, D. D. Koleske, and V. I. Klimov, "Energy-transfer pumping of semiconductor nanocrystals using an epitaxial quantum well.", Nature **429**, 642–646 (2004).

[6] S. Chanyawadee, P. G. Lagoudakis, R. T. Harley, M. D. B. Charlton, D. V. Talapin, H. W. Huang, and C. H. Lin, "Increased color-conversion efficiency in hybrid light-emitting diodes utilizing non-radiative energy transfer", Advanced Materials **22**, 602–606 (2010).

[7] G. Itskos, C. R. Belton, G. Heliotis, I. M. Watson, M. D. Dawson, R. Murray, and D. D. C. Bradley, "White light emission via cascade Förster energy transfer in (Ga, In)N quantum well/polymer blend hybrid structures", Nanotechnology **20**, 275207 (2009).

[8] G. Heliotis, G. Itskos, R. Murray, M. D. Dawson, I. M. Watson, and D. D. C. Bradley, "Hybrid inorganic/organic semiconductor heterostructures with efficient non-radiative energy transfer", Advanced Materials **18**, 334–338 (2006).

[9] J. Bai, Q. Wang, and T. Wang, "Characterization of InGaN-based nanorod light emitting diodes with different indium compositions", in Journal of applied physics, Vol. 111, 11 (2012).

[10]B. Liu, R. Smith, J. Bai, Y. Gong, and T. Wang, "Great emission enhancement and excitonic recombination dynamics of InGaN/GaN nanorod structures", Applied Physics Letters **103** (2013).

[11]Z. Zhuang, X. Guo, B. Liu, F. Hu, Y. Li, T. Tao, J. Dai, T. Zhi, Z. Xie, P. Chen, D. Chen, H. Ge, X. Wang, M. Xiao, Y. Shi, Y. Zheng, and R. Zhang, "High Color Rendering Index Hybrid III-Nitride/Nanocrystals White Light-Emitting Diodes", Advanced Functional Materials **26**, 36–43 (2016).

[12]M. Achermann, M. a. Petruska, D. D. Koleske, M. H. Crawford, and V. I. Klimov, "Nanocrystal-based light-emitting diodes utilizing high-efficiency nonradiative energy transfer for color conversion", Nano Letters **6**, 1396–1400 (2006).

[13]S. Blumstengel, S. Sadofev, C. Xu, J. Puls, and F. Henneberger, "Converting Wannier into Frenkel excitons in an inorganic/organic hybrid semiconductor nanostructure", Physical Review Letters **97**, 8–11 (2006).

[14]R. Smith, B. Liu, J. Bai, and T. Wang, "Hybrid III-Nitride/Organic Semiconductor Nanostructure with High Efficiency Nonradiative Energy Transfer for White Light Emitters", Nano Letters **13**, 3042–3047 (2013).

[15]Z. Zheng, K. H. Yim, M. S. M. Saifullah, M. E. Welland, R. H. Friend, J. S. Kim, and W. T. S. Huck, "Uniaxial alignment of liquid-crystalline conjugated polymers by nanoconfinement", Nano Letters **7**, 987–992 (2007).

[16]H. Sirringhaus, R. J. Wilson, R. H. Friend, M. Inbasekaran, W. Wu, E. P. Woo, M. Grell, and D. D. C. Bradley, "Mobility enhancement in conjugated polymer field-effect transistors through chain alignment in a liquid-crystalline phase", Applied Physics Letters **77**, 406–408 (2000).

[17]C. L. Donley, J. Zaumseil, J. W. Andreasen, M. M. Nielsen, H. Sirringhaus, R. H. Friend, and J.-s. Kim, "Effects of Packing Structure on the Optoelectronic and Charge Transport Properties in Poly(9,9-di- n -octylfluorene- alt -benzothiadiazole)", Journal of the American Chemical Society **127**, 12890–12899 (2005).

[18]S. a. Schmid, K. H. Yim, M. H. Chang, Z. Zheng, W. T. S. Huck, R. H. Friend, J. S. Kim, and L. M. Herz, "Polarization anisotropy dynamics for thin films of a conjugated polymer aligned by nanoimprinting", Physical Review B **77**, 115338 (2008).

[19]N. J. Findlay, J. Bruckbauer, A. R. Inigo, B. Breig, S. Arumugam, D. J. Wallis, R. W. Martin, and P. J. Skabara, "An organic down-converting material for white-light emission from hybrid LEDs.", Advanced materials (Deerfield Beach, Fla.) **26**, 7290–7294 (2014).

[20]Z. Hu, B. Muls, L. Gence, D. A. Serban, J. Hofkens, S. Melinte, B. Nysten, S. Demoustier-Champagne, and A. M. Jonas, "High-throughput fabrication of organic nanowire devices with preferential internal alignment and improved performance", Nano Letters **7**, 3639–3644 (2007).

[21]V. Vohra, U. Giovanella, R. Tubino, H. Murata, and C. Botta, "Electroluminescence from Conjugated Polymer Electrospun Nanofibers in Solution Processable Organic Light-Emitting Diodes", ACS Nano **5**, 5572–5578 (2011).

[22]F. Di Benedetto, A. Camposeo, S. Pagliara, E. Mele, L. Persano, R. Stabile, R. Cingolani, and D. Pisignano, "Patterning of light-emitting conjugated polymer nanofibres", Nature Nanotechnology **3**, 614–619 (2008).

[23]O. Fenwick, L. Bozec, D. Credgington, A. Hammiche, G. M. Lazzerini, Y. R. Silberberg, and F. Cacialli, "Thermochemical nanopatterning of organic semiconductors", Nature Nanotechnology **4**, 664–668 (2009).

[24]C. R. Belton, G. Itskos, G. Heliotis, P. N. Stavrinou, P. G. Lagoudakis, J. Lupton, S. Pereira, E. Gu, C. Griffin, B. Guilhabert, I. M. Watson, A. R. Mackintosh, R. A. Pethrick, J. Feldmann, R. Murray, M. D. Dawson, and D. D. C. Bradley, "New light from hybrid inorganic–organic emitters", Journal of Physics D: Applied Physics **41**, 094006 (2008).

[25]R. M. Smith, M. Athanasiou, J. Bai, B. Liu, and T. Wang, "Enhanced non-radiative energy transfer in hybrid III-nitride structures", Applied Physics Letters **107**, 121108 (2015).

[26]Z. Zhuang, Y. Li, B. Liu, X. Guo, J. Dai, G. Zhang, T. Tao, T. Zhi, Z. Xie, H. Ge, Y. Shi, Y. Zheng, and R. Zhang, "Optical polarization characteristics of c -plane InGaN/GaN asymmetric nanostructures", Journal of Applied Physics **118** (2015).

[27]Q. Wang, J. Bai, Y. P. Gong, and T. Wang, "Influence of strain relaxation on the optical properties of InGaN/GaN multiple quantum well nanorods", Journal of Physics D: Applied Physics **44**, 395102 (2011).

[28]M. Athanasiou, R. M. Smith, Y. Hou, Y. Zhang, Y. Gong, and T. Wang, "Enhanced polarization of (11–22) semi-polar InGaN nanorod array structure", Applied Physics Letters **107**, 141110 (2015).

[29]P. Y. Dang and Y. R. Wu, "Optical polarization anisotropy of tensile strained InGaN/AlInN quantum wells for TM mode lasers", Journal of Applied Physics **108**, 083108 (2010).

[30]M. Campoy-Quiles, M. I. Alonso, D. D. C. Bradley, and L. J. Richter, "Advanced Ellipsometric Characterization of Conjugated Polymer Films", Advanced Functional Materials **24**, 2116–2134 (2014).

[31]S.-W. Feng, Y.-C. Cheng, C.-C. Liao, Y.-Y. Chung, C.-W. Liu, C.-C. Yang, Y.-S. Lin, K.-J. Ma, and J.-I. Chyi, "Two-Component Photoluminescence Decay in InGaN/GaN Multiple Quantum Well Structures", physica status solidi (b) **228**, 121–124 (2001).

[32]M. Athanasiou, R. M. Smith, S. Ghataora, and T. Wang, "Polarized White Light from Hybrid Organic/III-Nitrides Grating Structures", Scientific Reports **7**, 39677 (2017).

Chapter 6

Direct-Write Laser Photolithography Fabrication of Micron and Sub-Micron Single Pillar Inorganic Light-Emitting Device

A technical demonstration of direct-write laser photolithography below the diffraction-limited spot-size has been achieved using a modified high-resolution confocal fluorescence spectral imaging microscopy system. The single-instrument is used to both fabricate and characterise III-nitride nano-photonics, transforming a 375 nm excitation source into a direct-write laser photolithography instrument with sub-micron resolution. An optimisation of the variable parameter allows construction of precise arbitrary mask-less designs, resulting in a minimum 145 nm feature-size through combined application of the non-linearities in inhomogeneous photolithography and development rate. A detailed and thorough investigation reviewing the feature-size relative to direct-write conditions has then been presented, calibrating relationship between measured feature-size and design parameter to reproduce required images or better in photoresist. The findings have then been applied to the fabrication of electrically injected single micro-pillar structured III-nitride light-emitting diodes, showing the electrical characteristics of a 3.7 µm and 13 µm diameter device. This approach demonstrates the capacity to also produce single nano-pillar LED with respective 326.2 nm and 382.1 nm diameter; measurable structures are however restricted by the ability to electrically-probe.

6.1 Introduction

The semiconductor photomask industry records market revenues reaching $4.04 billion worldwide, accounting 13 % of the entire semiconductor wafer fabrication market[1].

A standard UV contact photolithography system transfers 10^{11} - 10^{12} parallel bits stored on time-constant binary photomasks in a single exposure[2], with resolution registered down to approximately 1 µm. This provides high-speed consistent replication of micro-features in photosensitive material as required in larger-scale and industrial fabrication. System complexity increases with significant improvement below this limit, requiring expensive projection and reduction lenses[2]. Long design and manufacturing times dictate also the high-cost of even an individual photomask, increasing further with advancing complexity and density of modern integrated-circuits[3–5]. High-throughput therefore comes at the expense of flexibility and cost, making it non-conducive to instantaneous prototyping and low-scale research. A well-established alternative approach is direct-write laser photolithography[6–11].

Direct-write lithography delivers instead exposure energy through a focused laser beam at only pre-defined and configurable positions, rather than using masked broad-area uniform radiation across the entire substrate. This allows rapid autonomy to construct arbitrary mask-less designs spontaneously and without loss of even sub-micron resolution, encouraging scientific innovation.

In this study a commercial WITec Alpha300 confocal fluorescence spectral imaging microscopy system is used to both fabricate and characterise III-nitride nano-photonic devices in a single-instrument. The microscopy set-up has been able to demonstrate both high-resolution direct-write laser photolithography and confocal photoluminescence (PL) mapping using the same common control electronics. This is possible using WITec's elective DaVinci Nanolithography software package to arbitrarily control relative position between the prepared sample and focused laser beam spot. In addition this also provides function to define all necessary direct-write photolithography variable settings with integrated laser shutter control. Transforming the 375 nm coherent excitation source to a precise writing tool in direct photolithographic masking.

This investigation presenting a first demonstration and optimisation study of direct-write nano-photolithography using dedicated single-instrument optical characterisation system, previously also used in laser-ablation and thermal-reaction only[12–15].

The highly flexible and modular microscopy system requires first after-market modification, positioning an original equipment manufacturer (OEM) slider with a 550 nm optical longpass filter after the Köhler illumination white light LED source. This blocks the unintentional exposure of the standard mid-critical all-purpose I-line Rohm and Haas MEGAPOSIT SPR350 1.2 photoresist used exclusively throughout this study, blocking wavelengths below the absorption cut-off.

This system now lends itself to both raster and vector direct-write laser photolithography, as well its originally intended confocal spectral imaging purpose.

6.2 Method

6.2.1 System Description

Figure 6.1 shows a detailed schematic illustration of the microscopy system used in this study, as also previously described in section 3.3.1. The different instrument

beam path and measurement mode have been identified in colour as bright-field optical microscopy (yellow), reflected confocal fluorescence spectral imaging (green) and 375 nm laser excitation (blue); sharing optical axis in the vertical direction.

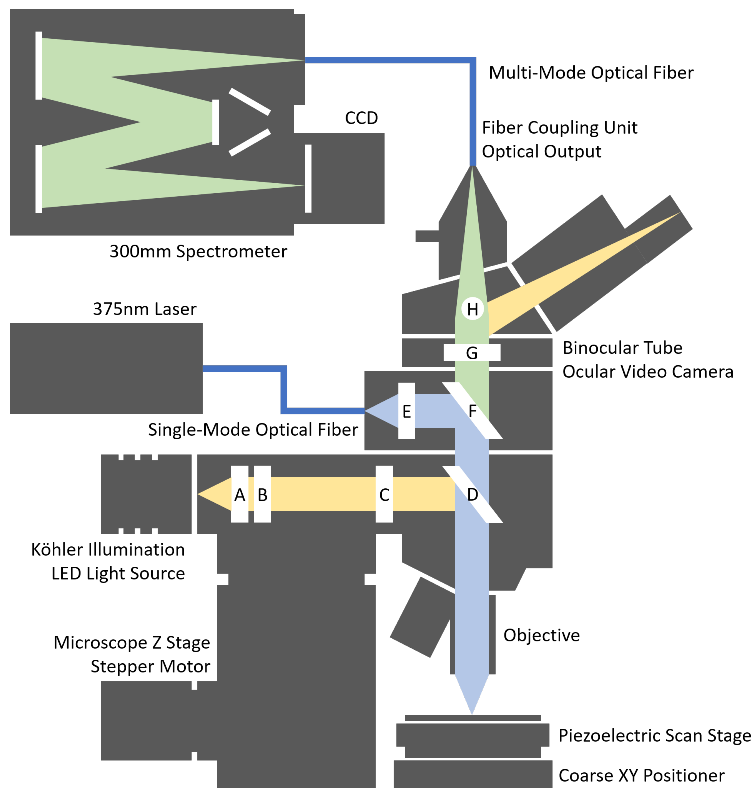

Figure 6.1: Schematic diagram of single-instrument confocal spectral imaging and direct-write photolithography system.

Position *A* on the bright-field illumination path identifies the OEM filter slider unit and 550 nm longpass filter. Following this positions *B* and *C* consist of an aperture and field-stop diaphragm; reflector slider *D* contains a 50:50 beam-splitter that directs bright-field light down onto the sample when selected in position.

A 375nm laser diode is coupled externally with adjustable focus to a single-mode optical-fiber. The polarisation maintaining fiber supports only the lowest-order transverse mode Gaussian beam, which can be focused to a diffraction-limited spot, giving high-performance confocality and spatial resolution. The laser coupling unit consists fundamentally of a micrometer attenuator and three-axis position and tilt adjustment plate, aligning the optical-fiber core to laser beam axis. A THORLABS SHB05T electronic controlled diaphragm shutter with a 29 ms mini-

mum exposure pulse is retrofitted to allow laser beam modulation.

The internal microscope body laser coupling unit is connected with an FC coupler, *E* is an achromatic collimating lens that adjusts focus to the sample-plane. Laser excitation is then directed toward this using positionable holographic beam-splitter *F*, which subsequently transmits specimen photoluminescence and reflected bright-field illumination through longpass laser rejection filter *G*.

High-performance 100x magnification objective with 0.95 NA and 310 μm working distance is used in both confocal spectral imaging and direct-write laser lithography; focusing and collecting light.

A sliding prism *H* on push-rod switches the optical-path between the SMA fiber-coupling unit and ocular colour eye-piece video camera. The fiber-coupling unit is a micrometer controlled lateral XY position adjustable SMA fiber-adapter that maximises optical signal coupled to the 10 μm confocal pinhole multi-mode fiber with alignment to the optical plane centre.

The 3-axis piezoelectric scan-stage has maximum lateral 100 x 100 μm and axial 20 μm scan range; with integrated capacitive closed-loop position feedback that provides stable sub-nanometre spatial resolution. The scan-stage is mounted above an additional coarse alignment 20 mm XY dovetail translation stage, upgradable to an expanded motor-controlled 150 x 80 mm XY sample positioner to allow full-wafer fabrication.

6.3 Micron and Sub-Micron Pillar Photoluminescence

6.3.1 Fabrication

Figure 6.2 depicts a schematic of the full fabrication process. A standard commercial *(a)* blue InGaN/GaN LED wafer grown on c-plane sapphire is used in fabrication of the device structures throughout. This consists of a 1 μm n-GaN layer with a thick undoped GaN buffer on a standard thin low-temperature GaN nucleation layer, 100 nm InGaN pre-layer, 160 nm InGaN/GaN multi-quantum well (MQW) active region and then final 230 nm p-GaN layer.

An approximate 300 nm MicroChem PMGI resist pre-layer and then subsequent 1 μm thin photoresist film *(b)* are spin-coated at 8000 RPM; intermixing after a sufficient soft-bake is negligible due to PMGI's insolubility in photoresist solvent. PMGI is used to assist in high-yield metal lift-off and to extend resolution

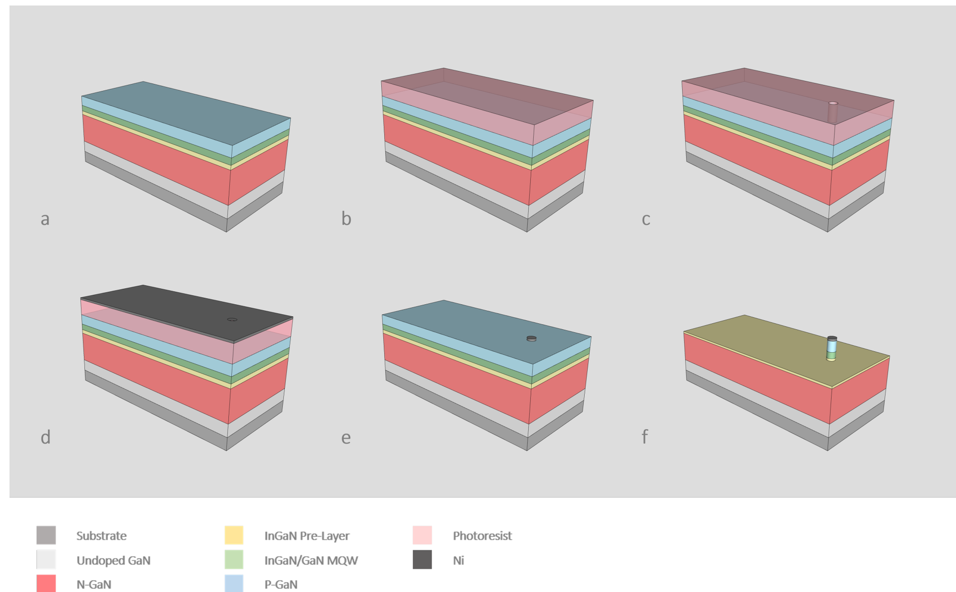

Figure 6.2: Schematic diagram of complete fabrication procedure using direct-write photolithography.

limits beyond a single photoresist layer strategy. The still photo-sensitive sample is then transferred to a darkened non-cleanroom environment for further processing, avoiding ambient light exposure.

The direct-write exposure *(c)* across the planar photoresist layer is then achieved using the previously detailed WITec confocal spectral imaging system without needing intermediate static photomasks. The sample position is controlled relative to the focused diffraction-limited CW 375 nm laser fixed in the microscope optical axis using DaVinci Nanolithography scripting software; sub-micron diffraction-limited spots are much easier to maintain from a stationary laser beam. The DaVinci scripting function facilitates both arbitrary movement and electronic shutter control to close the optical path where exposure is undesired, a method therefore suited overall to small-feature rapid prototyping.

Scanning and modulating the laser beam induces a local chemical change in molecular structure and solubility at the focal-point in positive-tone photoresist. A single-step development *(c)* then selectively removes exposed areas of resist; critical-dimensions are therefore strongly dependent on the writing parameter. Development provides a negative retrograde side-wall slope in the PMGI that also undercuts the photoresist imaging layer to give improved tear-free lift-off[16]. This

is followed with a reactive-ion etching (RIE) O_2 plasma ash that clears remaining residues from the exposed areas.

A 75 nm nickel layer is then deposited *(d)* under a low-pressure thermal evaporation. The patterned resist layer offers a sacrificial template that is *(e)* lifted-off to leave only the defined areas in metal. PMGI thicknesses significantly above that of the deposited nickel provide a discontinuity with the metal-film, ensuing clean lift-off. This acts then as an inversion secondary hard-mask in subsequent selective processing.

Transfer of the patterned nickel layer into the InGaN/GaN MQW structure *(f)* is achieved after a further 660 - 940 nm high flow-rate $SiCl_4\,/\,Cl_2\,/\,Ar_2$ inductively coupled plasma RIE (ICP) dry-etch; high ion-energy and plasma density result in smallest side-wall angle.

The flexibility of direct-write fabrication avoids the need for individual static photomasks with every design change[17]. Also the consolidation of processing exclusively to the all-purpose SPR350 photoresist means that each step is compatible with standard fabrication procedures at a higher-resolution and double exposures.

6.3.2 Direct-Write Optimisation

Along propagation axis the transverse laser beam profile purportedly remains Gaussian. The objective focuses collimated light to the beam-waist of an hyperboloid in the Z-axis, understood in diffraction theory, setting a principal limit to the optical systems resolution. A result of the Gaussian having no distinct edge and apparent boundary to characterise dimensions, diameter of a Gaussian beam can be somewhat arbitrary. The diffraction-limited beam-waist (ω_0) is however given to an approximate 240 nm minimum[12]. The diffraction-limited spot-size is directly proportional to wavelength, and therefore higher-energy light can be focused to a smaller diameter beam-waist; 375 nm laser point-source defining the best possible lateral results.

The objective of the exposure process is to reproduce closely the required image into photoresist, transferring the pattern with sufficient intensity and homogeneity across the full substrate[18]. An enhancement in feature-size can however be attained through investigation of the direct-write parameter and impact relative to photo-response function of the imaging resist. This examines the true and ideal response to light and attempts to account practical considerations beyond just pattern of light distribution in the subsequent device formation.

Contrast is a measure of the photoresists capacity to differentiate exposed and unexposed areas, characterised using quantifiable parameter that relates exposure to the photoresist thickness after development[19,20]. This would ideally translate to a step-function. Instead the photo-response is described by a power law relationship between the minimum and maximum energy-dose states; important in understanding both the photoresist and lithographic method used. Upper and lower energy density threshold limits define the respective point at which the photoresist solubility saturates or remains unchanged. Application of the power law relationship can therefore allow patterning to different photoresist thickness in a single-exposure using greyscale lithography[21,22].

Structures below diffraction-limited spot are possible as result of the laser-beam's Gaussian intensity distribution, meaning power measured at the central-peak is significantly higher than at the beam-waist circumference. This creates a lack of delineation between the exposed and unexposed regions. Taking advantage of the laser beam's lack of definitive edge[20], parts of the laser beam can therefore exist simultaneously above and below the photoresists exposure dose-to-clear threshold limits. Dimensions are therefore dependent on the energy-dosage supplied at each point. This is controlled primarily by the defined vector write-speed or raster-scan exposure time, but also power density. Higher-resolution than conventional direct-write imaging is therefore possible through calibration of the energy-dose relative to the measured dimension in fabrication; metal lift-off removing issues of etch-rate selectivity in which gradient photoresist features are transferred to the substrate[21,23].

Figure 6.3a shows a log-linear plot of the feature-size dimension against the exposure energy that is either calculated from raster dwell-time (blue) or vector-speed (red and black) over distance, considering over 300 data-points, including both diameter and linewidth. This demonstrates that with minimal exposure energy-dose sub-micron features below the approximate 480 nm diffraction-limited spot-size are achieved.

In this study the difference between singular defined raster and vector circular features are first considered, before briefly the linewidth of seamless linear features. The distinction between raster and vector direct-write lithography is that the raster approach generates time-variant designs, where dwell-time is controlled between each feature. This single-point exposure is inherently expected to give smallest dimensions in subsequent device fabrication stages, limited only by the diffraction-

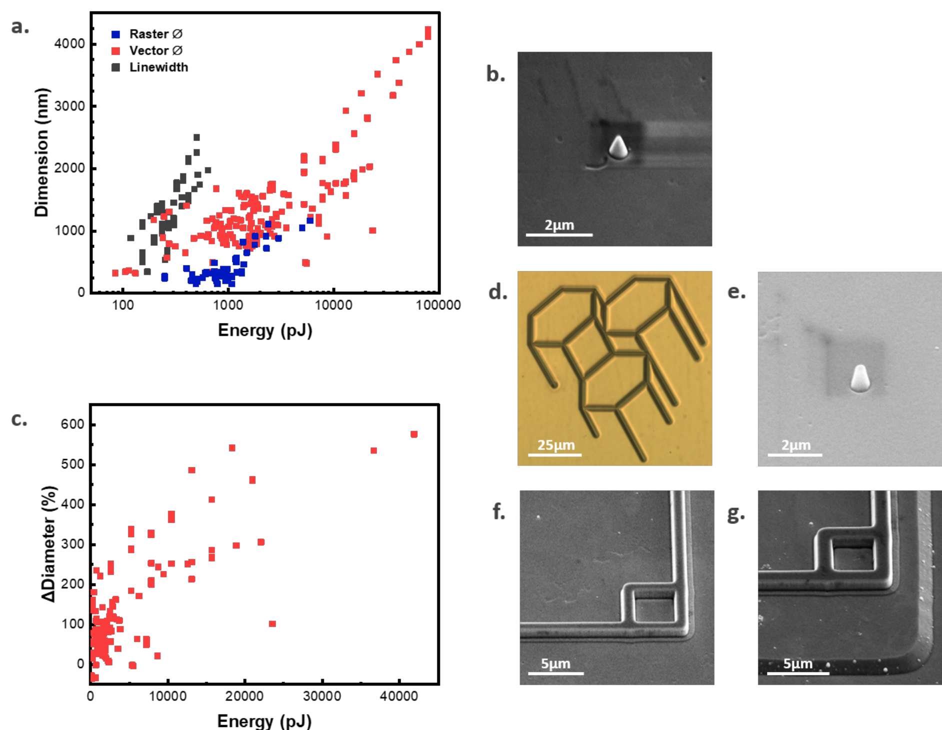

Figure 6.3: Optimisation of direct-write features relative to direct-write parameter: (a) semi-log plot of measured feature-size dimension against exposure energy; off-axis (45°) SEM image of fabricated (b) 145 nm diameter nano-pillar device; (c) linear plot of percentage diameter change against exposure energy; (d) optical image demonstrating arbitrary direct-write imaging; and off-axis (45°) SEM image of fabricated (e) 321 nm diameter nano-pillar device and (f) 895 nm and (g) 1130 nm linewidth.

limited spot-size. A vector feature is instead defined by the movement of the laser-beam between positions at defined speed, where energy considers the integrated exposure dosage for an entire vector pattern that contributes solely to a singular quantifiable dimension.

The laser beam power is set to operate at a consistent 1 mW to enhance stability. The optical power is then controlled with micrometer attenuation on the laser coupling unit and measured using a THORLABS PM100D compact power meter with a S120VC silicon photodiode sensor up to 50 mW with a 1 nW resolution over a 200 - 1100 nm range. The examined power of the CW laser diode is varied

between 1 - 500 nW with a 30 nW median and 56 nW average value; limited by the I-line 67 mJ/cm^2 sizing energy of SPR350 photoresist and 240 nm beam-waist. A ±5 % measurement uncertainty should be factored at the 375 nm wavelength.

Raster Direct-Write Features

The electronic diaphragm shutter can be used to modulate the laser beam on/off to expose a defined pattern, analogous to non-impact dot-matrix printing. The resulting quantifiable diameter of isolated single-point raster features are determined by an energy-variance that is controlled with the exposure time and power density, practical considerations for signal-delays are included in all instructions.

Energy is instead only varied across a smaller range between 249 and 6000 pJ. As from Figure 6.3a this replicates at the lower and upper limit a respective 239 and 1166 nm feature-size, where the former is well below the 480 nm diffraction-limited spot-size and latter gives the largest diameter. A mean 409 nm and median 323 nm diameter are recorded comparatively to a 1165 pJ and 923 pJ exposure energy.

In optimising these processes an NxN array is patterned across the full scan-area using an automated control script, where each element is centred on a single feature. A change in the structural dimensions relative to an exponential difference in the write-parameter is then observed between cells, creating sufficient separation between features to consider them in isolation.

The smallest 145 nm feature-size is achieved at an optimised 1.08 nJ energy-dose, significantly below the diffraction-limit. This is not however at the lowest exposure energy, but instead written using a 179 ms dwell-time and 6 nW power. The nano-structure is presented in the SEM image in Figure 6.3b, showing a 860 nm high truncated cone with a 74.4° side-wall angle and 145 nm diameter top nickel film.

A proposed explanation for this relates to focus. The focal point of a Gaussian-beam can affect the resist profile due to its hyperboloid form and change in power density as it is convergent or divergent to the beam-waist[24], despite the system having a depth-of-focus in the range of the photoresist thickness. A field-stop diaphragm positioned in the objective's back focal plane is used to aid optical positioning to the clean planar surface. The Z microscope stage is then employed to focus with a 30 mm travel range stepper motor and 10 nm step-size. No real-time auto-focus is used to account for potential surface fluctuations and an absence of

quantifiable alignment means defocusing of the laser beam is possible[7]. Passive vibration isolation (static granite plate) is however employed to minimise further external physical effects.

In addition, non-linearities with respect to intensity can also provide improvement in spatial resolution below the diffraction-limit, dependent on the activation energy of localised chemical reactions. This is not necessarily true of conventional homogenous photolithographic processes. Absorption of a Gaussian incident light can result in a similar distribution of temperature, where the reaction rate has a strong non-linear temperature dependence[25,26].

Vector Direct-Write Features

Alternatively, the typical direct-write vector designs demonstrated here have a 500 nm diameter circle that is patterned by a 20-point circumference vector, although extending from 500 nm to 2.5 µm with a 667 nm average. These are written at a vector-speed ranging between 1.3 - 1000 µm/s with a 29 and 101 µm/s typical and average, relative to Figure 6.3a.

Figure 6.3c depicts a linear-linear plot of percentage change in the diameter as a function of the exposure energy; as expected definite trend exists with an increasing energy. A positive or negative percentage change represents a respective increase and decrease in the diameter from the designed vector circumference, controlled with the write-speed and power density.

The measured upper and lower extreme limits range between 321 - 4231 nm, equating to a relative change between -36 % and 576 %; characterised by a 125 % average variance that corresponds to approximate median and mean diameters of 1217 nm and 1406 nm. The percentage change does not however translate from the equivalently designed and measured feature-size due to a seemingly non-linear relationship, where above approximately 5 nJ the percentage change increases at a slower-rate. The decreasing difference in diameter with greater deviations in the exposure energy suggest that the exposure profile changes with increasing power and/or scattering effects saturate to minimise over-exposure.

Figure 6.3d and 6.3e highlights the capacity of the direct-write lithography system to image arbitrary patterns in photoresist, Figure 6.3d showing the *Centre for GaN Materials and Devices* logo across approximately 80 x 80 µm. The scanning electron microscope (SEM) image in Figure 6.3e then shows the smallest vector 321 nm diameter nano-pillar following significant optimisation at a 45° off-axis,

measuring a 940 nm etched height and approximate 77.5° side-wall angle.

A short-wavelength incident light even at low-power will excite the active region of a light-emitting device, fluorescence at 450 nm as in this example is itself sufficient to partially expose the above photoresist layer. Calibration of direct-write single vector features can therefore be achieved by factoring a typical real increase in dimensions from design parameter.

Figure 6.3a also shows the relationship between linewidth (black) and the approximated exposure energy from vector-speed, showing a similar trend-line as with the diameter. The two additional SEM images in Figure 6.3f and 6.3g both show line-features patterned at a 15 μm/s write-speed with a measured 940 nm height and respective (left) 76.9° and (right) 73.6° side-wall angle. The left-most image has an 895 nm linewidth written at 30 nW power, alternatively the second image is 1130 nm wide and uses 50 nW.

A vector direct-write process allows a seamless rendering of features without demonstrating line-edge roughness (LER), a deviation from the ideal line-shape at a scale below the resolution limit[6,7]. This is because the Gaussian beam is convoluted across the line in practically infinite steps due to the sub-nanometre piezoelectric stage resolution. Transfer of this studied behaviour to pattern well-defined grossly non-planar structures is possible with the XYZ piezoelectric scan-stage, maintaining focus with change in Z-dimensions[27].

6.3.3 Confocal Photoluminescence

The single-instrument is then applied in demonstrating the optical characterisation of the same structured III-nitride light-emitting device. Fabricated structures are each detectable using this confocal PL spectral imaging technique provided thoughtful scan parameters; dimensions and step-size below the diffraction-limited spot will not otherwise offer distinction between adjacent spectral points. Minimum achievable lateral resolution is synonymous to the concept of image contrast. Resolution is characterised by the distance at which an optical system can distinguish between two-point objects separate in the image plane; Rayleigh criterion determines this to be where the respective central maxima and first minima intensity of the two features coincide.

Although not an actual point source the sample can be considered a superposition of infinite point-like objects with dimensions under the optical systems resolution. Confocal PL mapping can produce a point-like 0D to 3D spectral ar-

ray. The reflected fluorescent emission is collected in positions of the scanning point-source excitation beam, where intensity fluctuations are then correlated to the specimen structure. Emitted light outside the image-plane is rejected by focusing to the 10 μm pinhole, improving imaging contrast and lateral confocal resolution to approximately 200 nm. Pinhole diameter is significant because it requires trade-off between signal intensity and spatial resolution.

Spectra are measured using a Princeton Instruments SprectraPro 300i spectrometer and Andor Newton DU970N-UVB-353 back-illuminated CCD, as described in section 3.3.1. The 300 mm focal length spectrometer consists two aspheric mirrors and a three grating turret to disperse light of the collected beam; aspheric mirrors first collimating light to the grating and then focusing to the CCD for spectral acquisition. The input aperture is the second end to the SMA multimode optical-fiber connector that forms the pinhole.

A pixel in this instance is the manifestation of a complete spectrum at every scan position. Image scan parameters are restricted to below the number of resolvable point-like measurements per dimension.

An off-axis SEM image is provided in Figure 6.4a of the micro-pillar light-emitting device characterised under confocal PL study, measuring a 3.4 μm diameter and 660 nm etched height with an approximate 78.8° side-wall angle.

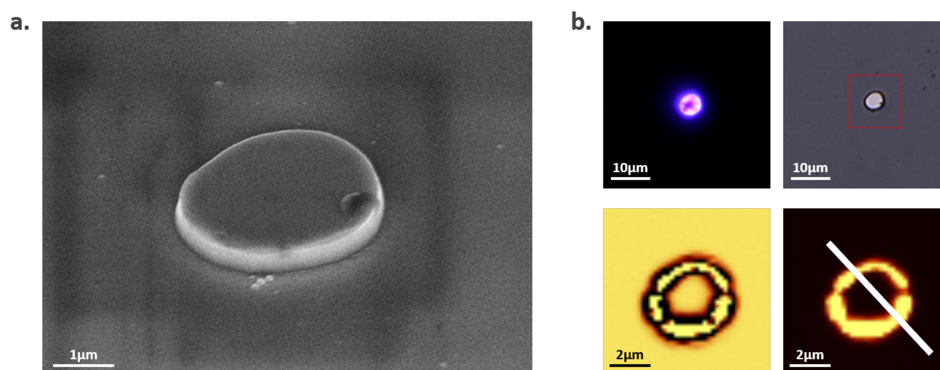

Figure 6.4: 3.4 μm diameter micro-pillar device (a) off-axis (45°) SEM image and (b) optical image of 375 nm laser excitation with scan-area [top] and 2D PL array map of the binomial average and integrated intensity distribution with cross-section [bottom].

Figure 6.4b shows top-left an optical image of the fluoresced light around periphery of the micron-scaled device, excitation coupled in from an edge. Image top-

right showing sample under-test and the 2D scan-area geometry, where bottom-left and bottom-right positions show a respective 2D PL array map of the average and integrated intensity distribution. The latter includes identification of the intensity cross-section profile demonstrated later in 6.5b.

A 10 x 10 μm PL map with 50 x 50 points and 36 ms integration time per spectrum is measured in XY across the direct-write laser fabricated area using a 150 grooves/mm grating. An absence of emission exists in the surrounding areas of the micro-pillar as result of removing the light-emitting active region completely. In central interior area the emission is not removed but is instead restricted by low-transmittance of the thick remaining thermally evaporated Ni hard-mask[28]. Peak incident and emission intensity is therefore primarily taken as scattered light at the side-wall.

The average scan better represents this change in intensity, where a low-pass mean-filter is applied to the image data object to replace data-points with binomial average of 3x3 pixel-grid values. This weights the central and surrounding values to different significance in calculating a new average, which has the effect of smoothing the images by minimising luminance variation between neighbouring pixels, reducing noise and eliminating data that is atypical of the area.

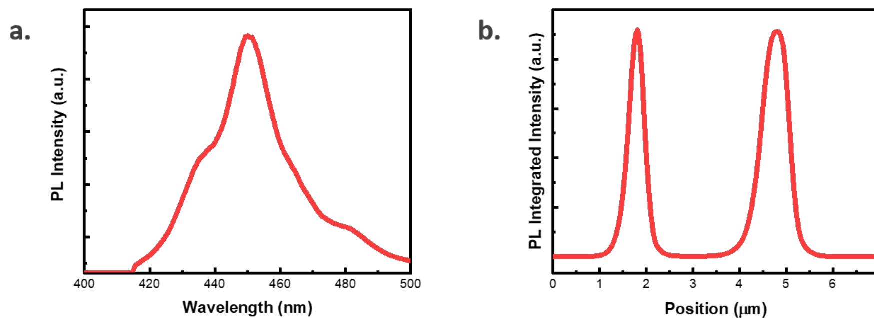

Figure 6.5: 3.4 μm diameter micro-pillar device (a) average PL spectrum across 10 x 10 μm scan-area and (b) PL integrated intensity cross-section profile.

An average PL spectrum across the entire scan-area graph data object is given in Figure 6.5a. This shows over a 414 - 500 nm range an emission-peak wavelength at 450 nm and 25 nm FWHM.

The binomial average image filtering also gives better visualisation of the cross-section profile in Figure 6.5b, removing the more abrupt change in luminance as

with the intensity distribution map. Demonstrating a more obvious gradual change in intensity that is better representative of the Gaussian-like distribution of the two peaks positioned at 1.8 and 4.8 µm. Importantly, confocal PL spectral imaging therefore provides an ability to accurately characterise structural features quickly; the image cross-section extracting an average intensity profile across a 200 nm linewidth perpendicular to the cross-section against real-position.

Considering difference between 90 % point of the first and second peak at their respective 1.7 and 5.0 µm extreme positions gives a 3.3 µm micro-pillar diameter, taking the separation at 10 % instead gives the 3.9 µm base diameter between 1.4 and 5.3 µm. These are both similarly comparable to the 3.4 and 3.7 µm dimensions taken using more traditional SEM measurements, demonstrating necessary accuracy. The difference between 10 and 90 % signal positions across a sharp emission edge can also give a rough approximation to the measured diffraction-limited beam-waist to 300 nm.

6.4 Micron Pillar Electroluminescence

The feasibility of nano-scale devices under electronic-excitation have been demonstrated previously with a reported 10 and 77 K low-temperature CW lasing of a 260 nm diameter III-P metallo-dielectric cavity at respective 3.5 and 6 µA current threshold[29]. In the same InP/InGaAs material system low-temperature (78 K) CW lasing under a 80 µA threshold injection current of a nano-pillar with diameter ranging between 330 – 500 nm and 1.4 µm resonant wavelength is again repeated[30]. Alternatively, the first 386.3 nm wavelength GaN-based room-temperature electrically pulsed lasing at above a 248 mA threshold current is demonstrated with a record 24 µm diameter microdisk structure, fabricated using standard optical lithography[31].

A micron and sub-micron round cavity confines light to the periphery of a small effective volume by total internal reflection, increasing the spontaneous emission coupled to the lasing mode through the Purcell effect[32], giving possibility for low-threshold and threshold-less lasing[33,34]. III-N semiconductors however generally have much higher lasing threshold when compared to other III-V materials, where current density is in the $\sim kA/cm^2$ range[35,36].

An ultra-stable high-performance single nano-laser is well-suited in nano-photonics, stable laser oscillation requiring that light intensity remains consistent

over time[37]. A transition to photonic integrated-circuits therefore has the potential to significantly lower energy consumption, replacing transistor switching, where an approximate 40 % of internet-related energy is consumed in data centre networks converting actual energy into computational power, after cooling and power-distribution[38,39].

The achievable high-speed modulation (> 0.1 THz) of a nano-laser, demonstrated under optical-excitation above 100 GHz[40,41], overcomes existing challenges facing electronic integrated-circuit in fundamental speed and bandwidth limits, where photonic signal do not suffer the same capacitive loading effect[29]. Photonic components are not however presently compatible with the scale of existing electronics (< 100 nm) blocking integration, requiring still a compact sub-micron and efficient electrically injected laser diode source, optical-pumping being entirely unfeasible in application.

An alternative to electron-beam lithography (EBL) is again presented here in the reproduction of nano-scale features, demonstrating dimensions between EBL ($\sim$ 10 nm) and standard contact photolithography ($\sim$ 1 µm)[20,42]. The application of this adapted high-performance direct-write laser photolithography instrument is tested in the fabrication of electrically injected single micro-pillar LED, where the measurable structures are limited only by the capacity to electrically-probe.

6.4.1 Fabrication

Figure 6.6 portrays a schematic of the entire fabrication process *(a-h)* resulting in a single micro-pillar structured LED.

The same standard commercial *(a)* blue InGaN/GaN LED wafer grown on c-plane sapphire is also used in this investigation. The as-grown structure again comprises a 1 µm n-GaN layer with a thick undoped GaN buffer on a standard thin low-temperature GaN nucleation layer, 100 nm InGaN pre-layer, 160 nm InGaN/GaN multi-quantum well (MQW) active region and then final 230 nm p-GaN layer.

An initial *(b)* mesa etching is first performed, selectively etching sections of the epi-wafer 680 nm down into the n-GaN layer for fabrication into isolated devices set as an array of 120 x 280 µm rectangular areas spaced 0.5 x 1 mm. N-contact electrodes *(c)* consisting of Ti/Al/Ti/Au (20/100/20/60 nm) are then subsequently thermally evaporated; both steps *(b)* and *(c)* are defined using standard contact photolithography.

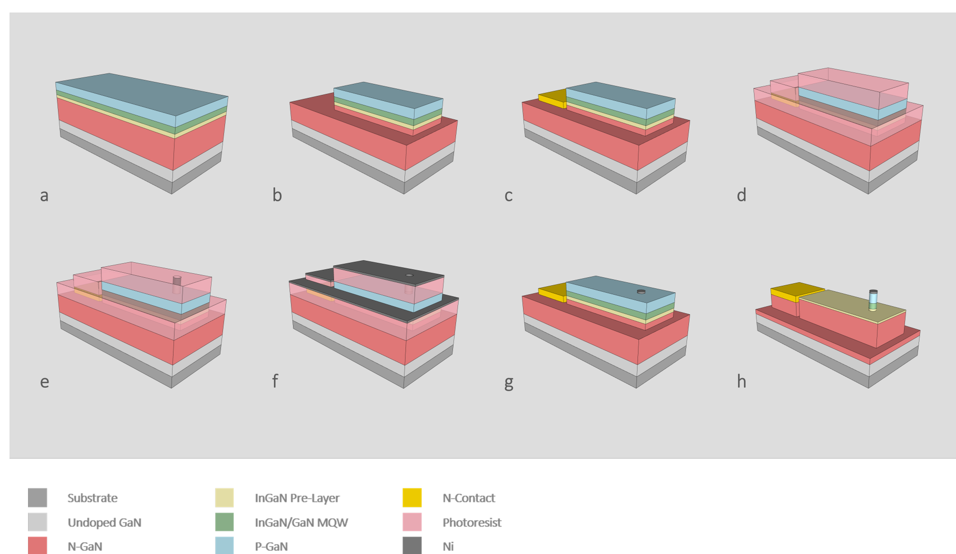

Figure 6.6: Schematic diagram of the single micro-pillar structured inorganic LED fabrication process (a-h).

A 300 nm MicroChem PMGI resist pre-layer and 1 μm thin positive-tone photoresist film *(d)* are again sequentially spin-coated at 8000 RPM.

Mask-less lithography *(e)* is then completed using the same confocal PL spectral imaging microscopy system described previously, focusing a 375 nm laser diode to diffraction-limited ∼480 nm spot-size. A direct-write pattern is defined through control of the relative substrate position to stationary laser beam utilising WITec's DaVinci Nanolithography scripting software, which facilitates both arbitrary movement and electronic shutter control. The mesa emission area is designed to match the maximum 100 x 100 μm travel range of the systems high-resolution piezoelectric scan-stage, patterning full-areas in a single-run exposure. The scanning and modulation of the laser beam induces a local chemical change in molecular structure and solubility at the focal-point in positive-tone photoresist, development *(e)* then selectively removing the exposed sections. This is then followed with an O_2 plasma ashing that clears remaining organic residues.

A 75 nm nickel layer is then *(f)* thermally evaporated and *(g)* lifted-off tear-free using the patterned photoresist as sacrificial template, leaving only defined areas in metal. The deposited metal-film then acts as an inversion secondary hard-mask, overcoming issues of etch-rate selectivity in subsequent selective processing, and later as a p-type electrode. Transfer of the patterned nickel layer into the LED

InGaN/GaN MQW structure *(h)* is then achieved after a further 940 nm high flow-rate $SiCl_4\,/\,Cl_2\,/\,Ar_2$ inductively coupled plasma (ICP) dry-etch.

This process combines the respective fast-throughput and flexibility of conventional and direct-write photolithography, allowing replication of consistent features without needing to replace intermediary static photomasks with each revision[17].

Figure 6.7 shows the fabricated electrical devices with a confirmed 940 nm height and 75 nm thick nickel p-type electrode, where the structure is determined by the requirements to electrically-probe.

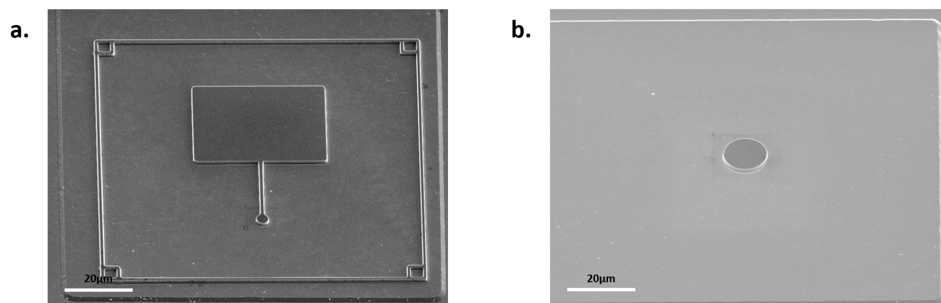

Figure 6.7: SEM images (45° angle) of single micro-pillar (a) LED *A* and (b) LED *B* with a respective 3.7 µm and 13 µm diameter.

LED *A* with a 3.7 µm diameter micro-pillar connected to a 40 x 30 µm contact via an uninsulated 1.1 µm wide bridge is shown in Figure 6.7a. This structure features an integrated alignment system that includes 5 x 5 µm inset corners and 100 x 100 µm perimeter drawn with a measured 894 nm linewidth; interface with the WITec control software and video-image feedback overlay then allows the manual alignment of subsequent direct-write device formation stages. LED *B* with a simplified arrangement includes just a 13 µm diameter single micro-pillar structure as shown in Figure 6.7b.

A single nano-pillar LED fabrication is also demonstrated in Figure 6.8a and 6.8b with respective a 326.2 nm and 382.1 nm diameter; current injection via direct electrical-probing is otherwise unsupported on the nano-scale. However, electrical characterisation of the single micro-pillar structured LED *A* and *B* provide verification through associated fabrication, which are produced under exact parallel conditions on the same as-grown sample.

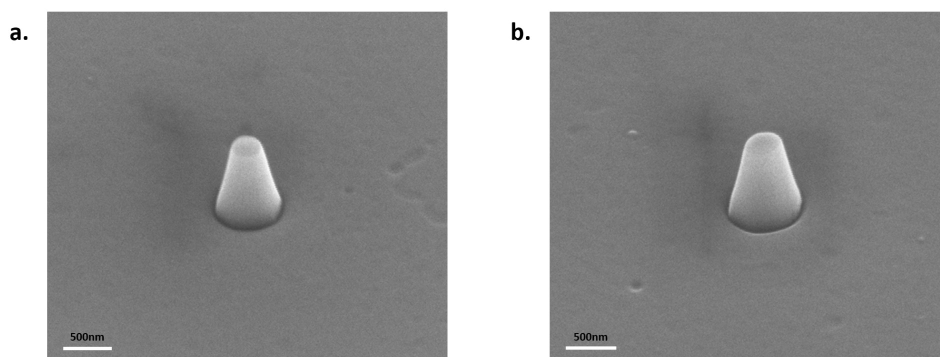

Figure 6.8: SEM images (45° angle) of (a) 326.2 nm and (b) 382.1 nm diameter single nano-pillar LED.

6.4.2 Electroluminescence

Electroluminescence (EL) is captured using a 600 nm probe-tip station as described in section 3.3.1, sufficient depth-of-focus and field-of-view ensure entire possible emission area of approximately 100 x 100 µm is collected.

Figure 6.9 shows the IV characteristics of LED *A* and *B* with a respective 3.7 µm and 13 µm diameter, exhibiting comparable electrical properties measured using a Keithley 2400 SourceMeter. LED *A* shows a 12.4 V turn-on voltage (20 µA) with a 37 $m\Omega$ series resistance, where instead LED *B* shows a 11.6 V turn-on voltage and 65 $m\Omega$ series resistance. The more significant change in resistance is a suspected result principally of the difference in device-area between 1240 μm^2 (*A*) and 98.1 μm^2 (*B*), where resistance decreases non-linearly with area.

The high turn-on voltage is however attributed to issues in forming an Ohmic anode and cathode. The nickel p-contact establishing first a Schottky barrier resulting from the difference in material work-function between p-GaN (7.5 eV) and Ni (5.1 eV)[43], generating additional band-gap discontinuities that otherwise restrict carrier flow. The effects of this can be reduced through a chemical composition grading, although no attempts are made to optimise the hard etch-mask for electrical contact. In addition, the 940 nm height completely exposes the active region side-walls, where an etch depth of just 490 nm is adequate to pass the InGaN/GaN MQW of the as-grown LED wafer into n-GaN. The combined etch depth of the mesa and direct-write features mean that the n-contact is instead positioned approximately 55 nm inside the undoped GaN buffer-layer, again a result of the unoptimised conditions.

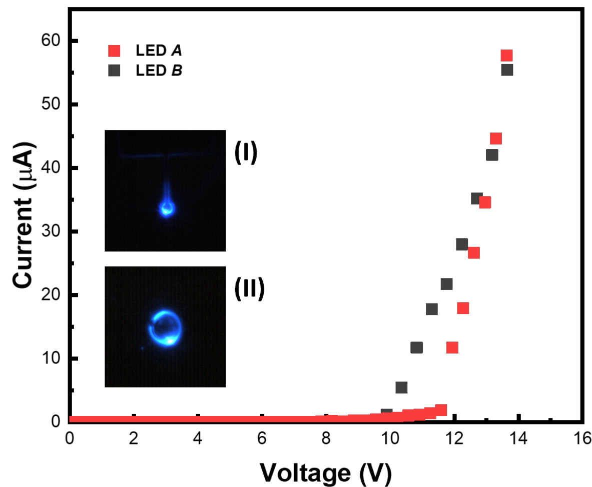

Figure 6.9: IV characteristics of the single micro-pillar LED *A* and *B*; inset optical images of (I) LED *A* and (II) LED *B* under 20 μA injection current

An optical image of the EL blue emission of LED *A* and *B* is also inset in Figure 6.9. This demonstrates that the thick low-transmittance nickel p-contact restricts top-vertical emission[28], where collected light is therefore primarily taken through side-wall scattering effect.

Figure 6.10 presents the EL spectrum of LED *A* and *B* measured under a 20 μA injection current with 0.08 nm wavelength resolution; peak blue emission is observed at 445.8 nm and 447.4 nm, respectively, with almost identical peak-intensity and 18.4 nm FWHM.

6.5 Conclusion

To conclude, the fabrication of a smallest 145 nm diameter tapered nano-pillar using a high-resolution confocal fluorescence spectral imaging microscopy system is presented. The single-instrument first requiring transformation to incorporate additional retrofit direct-write laser photolithography capabilities with a diffraction-limited 480 nm spot-size, allowing the reproduction of arbitrary mask-less nano-scale features. A detailed and thorough examination of the direct-write parameter relative to actual feature-size of sub-micron light-emitting devices are then pre-

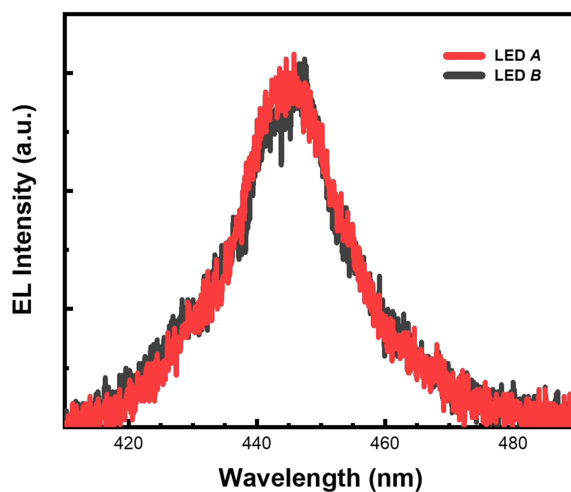

Figure 6.10: EL spectrum of the single micro-pillar LED *A* and *B* under 20 μA injection current.

sented, accounting considerations of the ideal and true photo-response. The optimisation process is then implemented in the construction of an optically-pumped 3.4 μm diameter micro-pillar structure, demonstrating PL characterisation using the same single-instrument in both fabrication and analysis. A fabrication scheme resulting in single micron and sub-micron optoelectronic light-emitting devices has then also been developed, providing a practical alternative between electron-beam lithography (EBL) and standard contact photolithography. In a technical demonstration the electrical characteristics of a 3.7 μm and 13 μm diameter single micro-pillar structured III-nitride LED are shown, more importantly an ability to fabricate single nano-pillar devices is also presented with a respective 326.2 nm and 382.1 nm diameter. The measurable features are limited only by the capacity to electrically-probe at the current dimensions, while verification is still provided through associated parallel fabrication.

6.6 References

[1]L. Chamness, *SEMI® Photomask Market Characterization Study, 2018 to 2020: A report covering Semiconductor Photomask Market Trends and Forecast*, tech. rep. (SEMI, 2019), pp. 1–21.

[2]R. Menon, A. Patel, D. Gil, and H. I. Smith, “Maskless lithography”, Materials Today **8**, 26–33 (2005).

[3]R. F. Pease, “Maskless lithography”, Microelectronic Engineering **78-79**, 381–392 (2005).

[4]G. V. Belokopytov and Y. V. Ryzhkova, “Optical maskless lithography”, Russian Microelectronics **40**, 414–427 (2011).

[5]D. Kattipparambil Rajan and J. Lekkala, “A maskless exposure device for rapid photolithographic prototyping of sensor and microstructure layouts”, Procedia Engineering **5**, 331–334 (2010).

[6]H. Ulrich, R. Wijnaendts-van-Resandt, C. Rensch, and W. Ehrensperger, “Direct writing laser lithography for production of microstructures”, Microelectronic Engineering **6**, 77–84 (1987).

[7]C. Rensch, S. Hell, M. V. Schickfus, and S. Hunklinger, “Laser scanner for direct writing lithography”, Applied Optics **28**, 3754 (1989).

[8]A. Braun and S. A. Maier, “Versatile Direct Laser Writing Lithography Technique for Surface Enhanced Infrared Spectroscopy Sensors”, ACS Sensors **1**, 1155–1162 (2016).

[9]Z. Zang, X. Zeng, J. Du, M. Wang, and X. Tang, “Femtosecond laser direct writing of microholes on roughened ZnO for output power enhancement of InGaN light-emitting diodes”, Optics Letters **41**, 3463 (2016).

[10]F. Benyettou, A. Aissat, M. Benamar, and I. Berbezier, “Contacting of Si/SiO 2 core/shell nanowires using laser photolithography”, Energy Procedia **119**, 131–138 (2017).

[11]C. Gui, X. Ding, S. Zhou, Y. Gao, X. Liu, and S. Liu, “Nanoscale Ni/Au wire grids as transparent conductive electrodes in ultraviolet light-emitting diodes by laser direct writing”, Optics & Laser Technology **104**, 112–117 (2018).

[12]WITec GmbH, *Application Note: Raman, PL & AFM measurements on lithographically created structures*, 2009.

[13]M. Athanasiou, R. M. Smith, S. Ghataora, and T. Wang, “Polarized White Light from Hybrid Organic/III-Nitrides Grating Structures”, Scientific Reports **7**, 39677 (2017).

[14]Q. Deng, Y. Yang, H. Gao, Y. Zhou, Y. He, and S. Hu, “Fabrication of micro-optics elements with arbitrary surface profiles based on one-step maskless grayscale lithography”, Micromachines **8** (2017).

[15]M. F. Huila, A. L. Parussulo, L. E. Armas, H. E. Peres, A. C. Seabra, F. J. Ramirez-Fernandez, K. Araki, and H. E. Toma, “Laser Patterning a Chem-FET Like Device on a V2O5 Xerogel Film”, IEEE Sensors Journal **18**, 1358–1363 (2018).

[16]S. Franssila and S. Tuomikoski, “MEMS Lithography”, in *Handbook of silicon based mems materials and technologies*, edited by M. Tilli, T. Motooka, V.-M. Airaksinen, S. Franssila, M. Paulasto-Kröckel, and V. Lindroos, 2nd ed. (Elsevier, 2015) Chap. 20, pp. 427–443.

[17]R. Moser, M. Kunzer, C. Goßler, K. Köhler, W. Pletschen, U. T. Schwarz, and J. Wagner, “Laser processing of gallium nitride–based light-emitting diodes with ultraviolet picosecond laser pulses”, Optical Engineering **51**, 114301 (2012).

[18]M. J. Madou, *Fundamentals of Microfabrication: The Science of Miniaturization*, 2nd ed. (CRC Press Taylor & Francis Group, 2001), pp. 1–752.

[19]F. Dill, “Optical lithography”, IEEE Transactions on Electron Devices **22**, 440–444 (1975).

[20]H. J. Levinson, *Principles of Lithography*, 3rd ed. (SPIE Press, Washington, 2011), pp. 1–32.

[21]C. Waits, B. Morgan, M. Kastantin, and R. Ghodssi, “Microfabrication of 3D silicon MEMS structures using gray-scale lithography and deep reactive ion etching”, Sensors and Actuators A: Physical **119**, 245–253 (2005).

[22]A. Bay, N. André, M. Sarrazin, A. Belarouci, V. Aimez, L. A. Francis, and J. P. Vigneron, “Optimal overlayer inspired by Photuris firefly improves light-extraction efficiency of existing light-emitting diodes”, Optics Express **21**, A179 (2013).

[23]I. Khazi, U. Muthiah, and U. Mescheder, “3D free forms in c-Si via grayscale lithography and RIE”, Microelectronic Engineering **193**, 34–40 (2018).

[24]C. A. Mack, "Understanding focus effects in submicrometer optical lithography: a review", Optical Engineering **32**, 2350 (1993).

[25]Y. S. Liu, "Sources, Optics, and Laser Microfabrication Systems for Direct Writing and Projection Lithography", in *Laser microfabrication: thin film processes and lithography*, edited by D. J. Ehrlich and J. Y. Tsao (Elsevier, 1989) Chap. 1, pp. 3–84.

[26]D. J. Ehrlich and J. Y. Tsao, "Nonreciprocal laser-microchemical processing: Spatial resolution limits and demonstration of 0.2-μm linewidths", Applied Physics Letters **44**, 267–269 (1984).

[27]A. Purvis, R. McWilliam, S. Johnson, N. L. Seed, G. L. Williams, A. Maiden, and P. Ivey, "Photolithographic patterning of bihelical tracks onto conical substrates", Journal of Micro/Nanolithography, MEMS, and MOEMS **6**, 043015 (2007).

[28]A. Axelevitch and B. Apter, "In-situ investigation of optical transmittance in metal thin films", Thin Solid Films **591**, 261–266 (2015).

[29]M. T. Hill, Y.-S. Oei, B. Smalbrugge, Y. Zhu, T. de Vries, P. J. van Veldhoven, F. W. M. van Otten, T. J. Eijkemans, J. P. Turkiewicz, H. de Waardt, E. J. Geluk, S.-H. Kwon, Y.-H. Lee, R. Nötzel, and M. K. Smit, "Lasing in metallic-coated nanocavities", Nature Photonics **1**, 589–594 (2007).

[30]K. Ding, L. Yin, M. T. Hill, Z. Liu, P. J. Van Veldhoven, and C. Z. Ning, "An electrical injection metallic cavity nanolaser with azimuthal polarization", Applied Physics Letters **102** (2013).

[31]J. Wang, M. Feng, R. Zhou, Q. Sun, J. Liu, Y. Huang, Y. Zhou, H. Gao, X. Zheng, M. Ikeda, and H. Yang, "GaN-based ultraviolet microdisk laser diode grown on Si", Photonics Research **7**, B32 (2019).

[32]K. J. Vahala, "Optical microcavities", Nature **424**, 839–846 (2003).

[33]Y. Rakovich and J. Donegan, "Photonic atoms and molecules", Laser & Photonics Reviews **4**, 179–191 (2009).

[34]Q. Gu, B. Slutsky, F. Vallini, J. S. T. Smalley, M. P. Nezhad, N. C. Frateschi, and Y. Fainman, "Purcell effect in sub-wavelength semiconductor lasers", Optics Express **21**, 15603 (2013).

[35]R. Tao and Y. Arakawa, "Impact of quantum dots on III-nitride lasers: a theoretical calculation of threshold current densities", Japanese Journal of Applied Physics **58**, SCCC31 (2019).

[36] V. Bougrov, M. Levinshtein, S. Rumyantsev, and A. Zubrilov, "Gallium Nitride (GaN)", in *Properties of advanced semiconductor materials: gan, ain, inn, bn, sic, sige*, edited by M. E. Levinshtein, S. L. Rumyantsev, and M. S. Shur, 1st ed. (John Wiley & Sons, Inc., New York, 2001) Chap. 1, p. 7.

[37] M. Fox, *Optical Properties of Solids*, 2nd ed. (Oxford University Press, Oxford, 2010).

[38] O. Popoola and B. Pranggono, "On energy consumption of switch-centric data center networks", The Journal of Supercomputing **74**, 334–369 (2018).

[39] S. Matsuo, A. Shinya, T. Kakitsuka, K. Nozaki, T. Segawa, T. Sato, Y. Kawaguchi, and M. Notomi, "High-speed ultracompact buried heterostructure photonic-crystal laser with 13 fJ of energy consumed per bit transmitted", Nature Photonics **4**, 648–654 (2010).

[40] B. Romeira and A. Fiore, "Purcell Effect in the Stimulated and Spontaneous Emission Rates of Nanoscale Semiconductor Lasers", IEEE Journal of Quantum Electronics **54**, 1–12 (2018).

[41] H. Altug, D. Englund, and J. Vučković, "Ultrafast photonic crystal nanocavity laser", Nature Physics **2**, 484–488 (2006).

[42] M. Shishova, S. B. Odinokov, D. S. Lushnikov, and A. Y. Zherdev, "Lithographic diffraction grating with a period failure", in Optical micro- and nanometrology vii, edited by C. Gorecki, A. K. Asundi, and W. Osten, May 2018 (May 2018), p. 14.

[43] J. R. Rumble, "Properties of Solids: Fermi Energy and Related Properties of Metals", in *Handbook of chemistry and physics*, edited by J. R. Rumble, 99th ed. (CRC Press Taylor & Francis Group, 2018) Chap. 12, pp. 1–1532.

Chapter 7

Conclusion

7.1 Conclusion

7.1.1 Overview

Electrically Injected Hybrid Organic/Inorganic White Light-Emitting Diode with Non-Radiative Förster Resonance Energy Transfer

A demonstration of electrically injected hybrid organic/inorganic III-nitride white LEDs were presented with an architecture compatible with the near-field requirements of non-radiative FRET. Top-down 2D micro-hole array structures were transferred to the InGaN/GaN MQW of a standard blue planar LED using a novel combination of standard fabrication process. The resulting white emitting device maintains relatively unchanged electrical performance, while providing the necessary near-field dipole-dipole separation. TRPL measurements of the compatible LED evidence a reduction in recombination lifetime of the InGaN/GaN MQW with organic/inorganic hybridisation; contributing a 16.7 % FRET efficiency across a device in which it accounts a 0.64 % total interaction area.

Polarised Light Emission from Inorganic and Hybrid Organic/Inorganic Nano-Grating Structured Device

The fabrication of optically-pumped hybrid organic/inorganic and electrically injected inorganic devices with respective highly polarised white and blue emission were demonstrated. This was achieved through combined mask-less laser ablation process and subsequent dry-etching technique to transfer 1D nano-grating structures through the InGaN/GaN MQW. The nano-structured inorganic active region emits polarised blue light through an anisotropic strain relaxation, occupation of F8BT down-converting material to the nano-channel then provides polarised yellow light emission following liquid crystalline phase macroscopic alignment. A strong relationship between the nano-channel duty-cycle and polarisation degree was observed. The polarisation dependent optical measurements show the hybrid organic/inorganic device with a combined white light polarisation degree up to 44 %; electrically injected blue emitting devices have a highest 34 % polarisation degree with largest nano-grating duty-cycle.

Direct-Write Laser Photolithography Fabrication of Micron and Sub-Micron Single Pillar Inorganic Light-Emitting Device

A 145 nm diameter nano-pillar structure was fabricated below the diffraction-limited spot-size of a high-resolution confocal spectral imaging system with retrofit direct-write laser photolithography capabilities. The single-instrument was used to both optically-characterise and construct arbitrary mask-less nano-scale light-emitting devices; detailed and thorough examination of direct-write parameter relative to actual feature-size were then presented. This comprehension is then implemented in the construction of an optically-pumped III-nitride micro-pillar structure, demonstrating PL characterisation of a 3.4 μm diameter device using the same single-instrument in both fabrication and analysis. A fabrication scheme resulting in single micron and sub-micron electrically injected light-emitting devices has then also been developed, providing a practical alternative between electron-beam lithography (EBL) and conventional photolithography. In a technical demonstration the electrical characteristics of a 3.7 μm and 13 μm diameter single micro-pillar structured III-nitride LED were shown, more importantly an ability to fabricate nano-pillar devices was also presented with a respective 326.2 nm and 382.1 nm diameter. The measurable features were limited only by the capacity to electrically-probe at the existing dimensions, while verification is provided through associated parallel fabrication.

7.1.2 Future Research

This work demonstrates the fabrication and characterisation of electrically injected micron and sub-micron featured III-nitride LED. In the process a novel sub-wavelength fabrication method using a modified single-instrument direct-write laser photolithography and high-resolution confocal PL microscopy system has been developed; demonstrating mask-less laser-ablation and exposure of photoresist below the diffraction-limited spot-size.

The expected steps following this works should include fabrication and electrical characterisation toward single nano-pillar LED using optical lithography, where the biggest challenge still remains to find means of injecting current even at the micron-scale[1,2]. A number of practical device structures should be considered in discovering the most efficient electrical-pumping scheme, including lateral side-wall, axial top-surface and suspended air-bridge excitation with appropriate dielectric isolation to large-area p-contact. The requirement being to form a p-type contact without short-circuiting across the active region, providing capacity to electrically-probe at all dimensions[3]. The developed fabrication scheme would then effortlessly lend itself to the demonstration of an electrically injected micron and/or sub-micron cavity laser[2], requiring first an epitaxial structure with sufficient vertical confinement to sustain optical modes[4].

The developed optical lithography system provides almost limitless design possibilities over a single 100 x 100 μm scan-stage area with homogeneous sub-micron resolution. An arbitrary mask-less pattern transfer can allow the simultaneous fabrication of active nano-photonic emitters and passive photonic integrated circuits[5], where in-plane electrical-excitation methods are inherently compatible with the requirements of near-field (< 100 nm) side-coupled optical waveguides[1]. This has been previously restricted by the impractically large diameter of existing electrically-pumped devices.

Additionally, a continued interest in combined complimentary organic and inorganic material groups would also be explored, considering the influence of LED structure and down-converting OLEP in optimising chromaticity and colour-rendering. Characterising the relationship then between the non-radiative FRET efficiency and respective interaction volume using the same direct-write laser photolithographic patterning to control feature-size and density, which fundamentally requires only to bring the resonant donor and acceptor dipoles in close proximity.

7.2 References

[1] F. Tabataba-Vakili, S. Rennesson, B. Damilano, E. Frayssinet, J.-Y. Duboz, F. Semond, I. Roland, B. Paulillo, R. Colombelli, M. E. Kurdi, X. Checoury, S. Sauvage, L. Doyennette, C. Brimont, T. Guillet, B. Gayral, and P. Boucaud, "III-nitride on silicon electrically injected microrings for nanophotonic circuits", Optics Express **27**, 11800 (2019).

[2] J. Wang, M. Feng, R. Zhou, Q. Sun, J. Liu, Y. Huang, Y. Zhou, H. Gao, X. Zheng, M. Ikeda, and H. Yang, "GaN-based ultraviolet microdisk laser diode grown on Si", Photonics Research **7**, B32 (2019).

[3] J. Bai, Q. Wang, and T. Wang, "Greatly enhanced performance of InGaN/GaN nanorod light emitting diodes", Physica Status Solidi (A) Applications and Materials Science **209**, 477–480 (2012).

[4] Y. Fan and K. A. Shore, "Design of Room Temperature Electrically Pumped Visible Semiconductor Nanolasers", IEEE Journal of Quantum Electronics **54**, 1–7 (2018).

[5] F. Tabataba-Vakili, L. Doyennette, C. Brimont, T. Guillet, S. Rennesson, E. Frayssinet, B. Damilano, J.-y. Duboz, F. Semond, I. Roland, M. El Kurdi, X. Checoury, S. Sauvage, B. Gayral, and P. Boucaud, "Blue Microlasers Integrated on a Photonic Platform on Silicon", ACS Photonics **5**, 3643–3648 (2018).

Chapter 8

Appendices

8.1 Appendix 1 - List of Symbols

$\boldsymbol{\theta}_{\mathbf{c}}$ = critical angle

$\mathbf{n_{air}}$ = ambient-air refactive index

$\mathbf{n_{gan}}$ = GaN refractive index

$\boldsymbol{\lambda}$ = wavelength

$\mathbf{h}$ = Planck's constant $(6.63 \times 10^{-34}\ Js)$

$\mathbf{p}$ = particle momentum

= hole density

$\mathbf{E}$ = energy

$\mathbf{c}$ = speed of light $(3.00 \times 10^{8}\ ms^{-1})$

$\mathbf{E_g}$ = band-gap energy

$\mathbf{E_c}$ = conduction band minima

$\mathbf{E_v}$ = valence band maxima

$\mathbf{F(E)}$ = Fermi-Dirac distribution

$\mathbf{E_F}$ = Fermi level

$\mathbf{k_B}$ = Boltzmann constant $(1.38 \times 10^{-23}\ JK^{-1})$

$\mathbf{T}$ = absolute temperature

$\mathbf{k}$ = wavenumber

$\boldsymbol{\hbar}$ = reduced Planck's constant $(1.05 \times 10^{-34}\ Js)$

$\mathbf{n}$ = electron density

= principal quantum number

$\mathbf{N_c}$ = conduction band density of states

$\mathbf{N_v}$ = valence band density of states

$\boldsymbol{\sigma}$ = electrical conductivity

$\mathbf{e}$ = elementary charge constant $(1.60 \times 10^{-19}\ C)$

$\boldsymbol{\mu}_{\mathbf{n}}$ = electron mobility

$\boldsymbol{\mu}_{\mathbf{p}}$ = hole mobility

$\mathbf{n_i}$ = intrinsic carrier density

$\boldsymbol{\tau}$ = total recombination lifetime

τ_r = radiative lifetime

τ_{nr} = non-radiative lifetime

η_{IQE} = internal quantum efficiency

$\mathbf{R}$ = recombination rate

= optical cavity radius

β = bimolecular recombination coeffecient

= spontaneous emission coupling factor

$\mathbf{n_0}$ = equilibrium electron density

$\delta\mathbf{n}$ = excess electron density

$\mathbf{p_0}$ = equilibrium hole density

$\delta\mathbf{p}$ = excess hole density

$\mathbf{E_n}$ = exciton binding energy

= discrete quantum well energy

μ = reduced electron-hole mass

$\mathbf{m_0}$ = invariant mass

ε_r = relative dielectric constant

$\mathbf{R_H}$ = Rydberg energy of hydrogen $(13.6\ eV)$

$\mathbf{m^*}$ = effective particle mass

$\mathbf{L}$ = quantum well thickness

$\Psi(x,t)$ = Schrödinger wave equation

$\mathbf{x}$ = positon

= indium mole fraction

$\mathbf{t}$ = time

$\mathbf{E_{InGaN}}$ = InGaN band-gap energy

$\mathbf{E_{InN}}$ = InN band-gap energy $(0.7\ eV)$

$\mathbf{E_{GaN}}$ = GaN band-gap energy $(3.4\ eV)$

$\mathbf{b}$ = bowing parameter $(1.4\ eV)$

$\Phi_V(\lambda)$ = luminous flux

η_0 = maximum luminous efficacy $(683\ lmW^{-1})$

$\boldsymbol{V(\lambda)}$ = CIE photoptic eye sensitivity function

$\boldsymbol{P(\lambda)}$ = spectral output power

$\boldsymbol{\eta_l}$ = luminous efficacy

$\mathbf{P}$ = input power

$\mathbf{Q}$ = quality factor

$\boldsymbol{\Delta\lambda}$ = bandwidth

$\mathbf{F_p}$ = Purcell factor

$\mathbf{n_c}$ = cavity refractive index

$\mathbf{V_{eff}}$ = effective cavity mode volume

$\boldsymbol{\Delta\lambda_{FSR}}$ = free spectral range

$\mathbf{W_{min}}$ = minimum resolvable linewidth

$\mathbf{Z}$ = mask-substrate separation

$\mathbf{I(t)}$ = instantaneous intensity

$\boldsymbol{\alpha_x}$ = bi-exponential magnitude decay components

$\boldsymbol{\tau_x}$ = bi-exponential lifetime decay components

$\mathbf{k_{MQW}}$ = total inorganic multi-quantum well recombination rate

$\mathbf{k_r}$ = radiative recombination rate

$\mathbf{k_{nr}}$ = non-radiative recombination rate

$\mathbf{k_{Hyb.}}$ = total hybrid organic/inorganic recombination rate

$\mathbf{k_{FRET}}$ = FRET recombination rate

$\boldsymbol{\bar{\tau}}$ = average weighted lifetime

$\boldsymbol{\eta_{FRET}}$ = FRET efficiency

$\boldsymbol{\rho}$ = polarisation degree

$\mathbf{I_{//}}$ = total parallel intensity

$\mathbf{I_{\perp}}$ = total perpendicular intensity

8.2 Appendix 2 - As-Grown Sample Structures

Chapters 4, 5 and 6

A commercial (Arima Optoelectronics Corp.) blue InGaN/GaN LED wafer grown on c-plane sapphire used in chapters 4 to 6, as demonstrated in Figure 8.1, which consists:

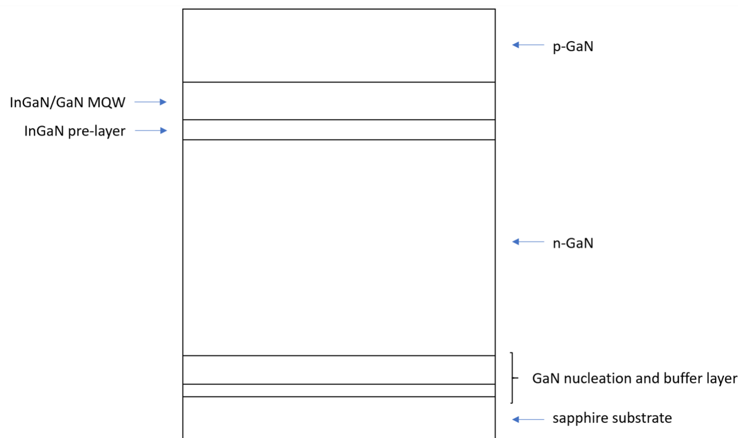

Figure 8.1: Schematic representation of an as-grown blue InGaN/GaN LED wafer structure grown on c-plane sapphire (not to scale).

- 1 µm n-GaN layer with a thick un-doped GaN buffer on a standard thin low-temperature GaN nucleation layer (unknown dimension);
- 100 nm InGaN pre-layer;
- 160 nm InGaN/GaN MQW active region (unknown period); and
- 230 nm p-GaN capping-layer.

Chapter 5

A standard five-period InGaN/GaN MQW epi-wafer grown on double-side polished c-plane sapphire, as shown in Figure 8.2, using an in-situ metal-organic chemical vapour deposition (MOCVD) system. This structure is used exclusively in chapter 5 and consists:

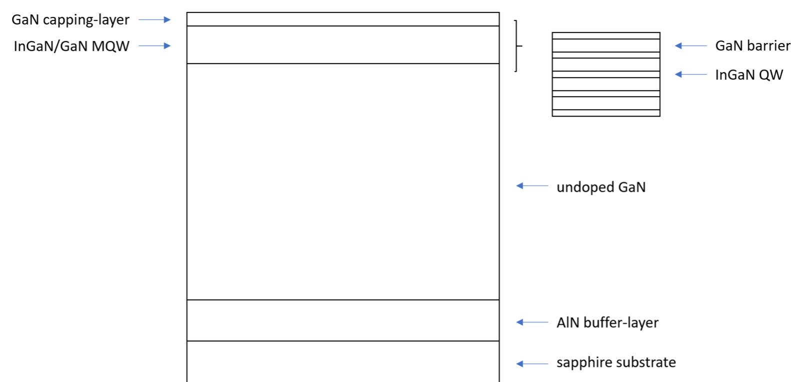

Figure 8.2: Schematic representation of an as-grown five-period InGaN/GaN MQW wafer structure grown on double-side polished c-plane sapphire (not to scale).

- 200 nm high-temperature AlN buffer-layer;
- 1.2 µm undoped GaN;
- 5x 2.5 nm InGaN quantum wells and 10 nm GaN barriers with an ∼20 % indium content; and
- 10 nm GaN capping-layer.